QUANTUM PHYSICS OF MOLECULAR MAGNETS

By

Reem Jaafar

A dissertation submitted to the Graduate Faculty in Physics in partial fulfillment of
the requirements for the degree of
DOCTOR OF PHILOSOPHY
at
THE CITY UNIVERSITY OF NEW YORK
2010

This manuscript has been read and accepted for the Graduate Faculty in Physics in satisfaction of the dissertation requirement for the degree of Doctor of Philosophy.

Date	Dist. Professor Eugene M. Chudnovsky Chair of Examining Committee
Date	Professor Steven Greenbaum Executive Officer

Professor J. Birman

Professor D. A. Garanin

Professor A. Kent

Professor F. Smith

Supervisory Committee

THE CITY UNIVERSITY OF NEW YORK

Abstract

QUANTUM PHYSICS OF MOLECULAR MAGNETS

by

Reem Jaafar

Advisor: Eugene M. Chudnovsky, Distinguished Professor of Physics
Co-Advisor: Dmitry Garanin, Prof. of Physics

In this thesis we focus on various aspects of quantum physics in molecular magnets, in particular, in Mn_{12}-acetate. This thesis is divided into three parts.

In the first part, we present a review on molecular magnets. Since Mn_{12}-acetate has a large spin (equal to 10), the theory of tunneling of a large spin is discussed as well as the early experiments that were performed two decades ago and which has shown spin tunneling, in particular, the ones that were performed on γ-Fe_2O_3 and on antiferromagnetic ferritin. Then, the first experiments that presented evidence on spin tunneling in Mn_{12}-acetate are outlined in detail. Magnetic hysteresis curves are shown and Landau-Zener effect in molecular magnets is discussed. Quantum classical crossover between thermally assisted and pure quantum tunneling regimes is described.
Finally, magnetic avalanches are introduced: they are another feature of the magnetization curve in Mn_{12}-Acetate where there is a sudden reversal in the magnetization. We exploit the first two experiments performed to elucidate the nature of magnetic avalanches in Mn_{12}-acetate and the theory developed as a result of these experiments.

In the second part of this thesis, we focus on three of my publications on quantum magneto-mechanical effects. First, a recent experiment on Einstein-de Haas effect in

a NiFe film deposited on a microcantilever is discussed. The cantilever was placed inside a coil that generated an ac magnetic field. Oscillation of the cantilever was measured by a fiber-optic interferometer positioned above the tip of the cantilever. When the frequency of the ac field matched the resonance frequency of the cantilever the amplitude of the oscillations was about 3 nm. The data were analyzed within a model that replaced the mechanical torque due to change in the magnetization with the effect of the periodic force acting on the fictitious point mass at the free end of the cantilever so this model did not account for the microscopic dynamics of the Einstein-de Haas effect. This motivated us to develop a more rigorous theoretical framework for the description of the dynamics of the Einstein-de Haas effect that we applied to the problem of the magnetic cantilever.

We then study the quantum dynamics of a magnetic molecule deposited on a microcantilever. Amplitude and frequencies of the coupled magneto-mechanical oscillations have been computed. We show that oscillations of the spin and the cantilever occur independently at frequencies $\Delta/\hbar$ and ω_n respectively, unless these two frequencies come very close to each other.

The results show that the splitting δ has no free parameters and that for a given resonance, $\Delta = \hbar\omega_n$, the relative splitting δ depends only on the position of the molecule on the cantilever. We then show that existing experimental techniques permit observation of the driven coupled oscillations of the spin and the cantilever, as well as of the splitting of the mechanical modes of the cantilever caused by spin tunneling.

Finally, the dynamics of a magnetic molecule bridged between two conducting leads is investigated. We start by reviewing various experiments performed when there is a weak coupling between the molecule and the leads and when there is a strong coupling which results in the Kondo effect. Experimental efforts were mainly motivated to measure the electronic current through a single molecule. We study the dynamics of the total angular momentum that couples spin tunneling to the mechanical rotations. We show that the Landau-Zener spin transition produced by the time-dependent magnetic field generates a unique pattern of mechanical oscillations that can be detected by measuring the electronic tunneling current through the molecule.

In the last and final part, we present our numerical work to describe quantum magnetic deflagration in Mn_{12}-acetate. This part is related to magnetic deflagration as discussed in part I of this thesis. The focus is on the quantum features of magnetic deflagration which are exhibited by the maxima in the speed of deflagration front as a function of the applied magnetic field. We review recent work on the effect of the dipolar field in forming self-organized fronts of spin tunneling, and present our enhanced computational work on the calculation of the relaxation rate. Previously, spin relaxation rates were calculated using a simple Arrhenius exponent. In this thesis we calculate the relaxation rate as a function of both the external field and temperature using the density matrix formalism and use them to study the effect of the transverse field on the front speed of deflagration.

To my parents,
Dr. Ali and Acinta Jaafar.

Acknowledgments

First I would like to express my deepest gratitude for my advisor Prof. Eugene Chudnovsky for his distinguished and professional mentorship, support and patience. I couldn't imagine having a better advisor than him. His guidance and his availability for discussion made this thesis possible. He greatly supported me during my most difficult days in graduate school, including the time when I was pregnant. He has given me the opportunity to participate in various conferences and promoted my work whenever possible.

I also would like to thank Prof. Dmitry Garanin for numerous valuable discussions. His constructive criticism has helped me become a better physicist. I also would like to thank him for his friendship and sense of humor.

I thank Prof. Joseph Birman for serving on this committee and for teaching me mathematical physics when I first started graduate school.

I thank Prof. Frederick Smith for his help and guidance when I was at City College, and for teaching me solid state physics when I first started graduate school. He also advised me on several academic issues.

I thank Prof. Andrew Kent for serving on this committee and for many useful discussions we had on several occasions.

I also would like to extend my gratitude to Jaroslav Albert with whom I had shared the office and had great physics discussions.

At Lehman college, I thank all faculty members for providing a supportive and pleasant atmosphere. In particular, Prof. Chris Gerry had made one of his offices available to me when needed and Prof. Dimitra Karabali promptly addressed my concerns whatever they were. I recently started sharing the office with Micheal O'Keeffe, Liufei Cai and Debajyoti Sarkar. They all created a pleasant atmosphere and let me use their computers whenever mine crashed. In particular, I thank Micheal O'Keeffe for substituting for my teaching whenever I was unavailable.

When I first started doing research I was a student at City College and would like to thank few people there. First, I thank the late Russell Hinchliffe for his help in the machine shop. I was deeply saddened by his death. His memory will remain in my heart forever.
I would also like to extend my deepest gratitude to Prof. Myriam Sarachik for her mentorship and for the great guidance and research opportunities she has given me. She also has given me the opportunity to attend several conferences and to meet very influential people in science.
I thank Prof. Timothy Boyer for advising me on classes and various academic issues. I would also like to thank Yoko Suzuki who first taught me how to operate the ^{3}He cryostat, David Graybill who taught me how to operate the magnetometer and Sean McHugh for working with me on various projects and on trouble-shooting issues in the laboratory.

On a personal level, I cannot be thankful enough to my husband Shadi Haidar for his endless support and love. He stood by me and encouraged me at every single stage. He also picked me up very late whenever I needed to work long hours. The arrival of our son Adam Allen has brought so much joy to our life and has motivated me to work harder. I am deeply grateful to my parents Dr. Ali and Acinta Jaafar and my parents-in-law, Afif and Rajiah Haidar who never stopped worrying about me. In particular, my mother's and my mother-in-law's cooking for me over the summer for the whole year has helped me focus on my research during the academic year. My mother-in-law pleasantly volunteered to stay with my son Adam while I am completing my work. Without them this work could have never been possible. I am indebted to them for the rest of my life. I finally thank my sister Rana and her husband Jeff for helping me when I moved back to the States.

Table of Contents

Table of Contents x

list of figures xii

I Single Molecule Magnets 1

1 History 3

1.1 The Theory of Tunneling of a Large Spin 3

1.2 Early Experiments on Spin Tunneling 7

1.2.1 Ensembles of Small Particles 7

1.2.2 Experiments on Spin Tunneling 9

1.3 Tunneling in Antiferromagnetic Ferritin 14

2 Spin Tunneling in Molecular Magnets 18

2.1 Quantum Magnetic Hysteresis 18

2.1.1 Mn_{12}-Acetate 18

2.1.2 Quantum Tunneling in Single Molecule Magnets 21

2.2 Landau Zener Effects in Molecular Magnets 23

2.2.1 Tunnel Splitting 23

2.2.2 A Perturbative Approach to Spin Tunneling 26

2.2.3 Probability of Tunneling in a Field-Swept Experiment 28

2.3 Berry Phase in Molecular Magnets 29

2.4 Quantum Classical Crossover Between Thermally Assisted and Pure Quantum Tunneling in Molecular Magnets 35

3 Magnetic Deflagration 39

3.1 Nature of Magnetic Avalanches 39

3.2 Quantum Features of Magnetic Avalanches 43

3.3 Theory of Magnetic Deflagration 44

II Quantum Magnetomechanical Effects 50

4 Einstein-de Haas Effect at the Nanoscale 52
- 4.1 Einstein-de Haas Effect in a NiFe Film Deposited on a Microcantilver 52
  - 4.1.1 What is the Einstein-de Haas Effect? 52
  - 4.1.2 NIST Experiment 54
- 4.2 Spin Rotation Interaction 56
  - 4.2.1 Introduction 56
  - 4.2.2 Microscopic Theory of Spin-Rotation Coupling 56
- 4.3 Theory of a Magnetic Microcantilever 60
  - 4.3.1 Elastic Theory With Internal Twists due to Spin-Rotation Coupling 60
  - 4.3.2 Dynamics of Magnetic Cantilever 63
  - 4.3.3 Suggestions for Experiment and Comparison With NIST's Experiment 71

5 Magnetic Molecule on a Microcantilever 73
- 5.1 Projection on a Two-State System 74
- 5.2 Coupled Dynamics of Spin and Cantilever 76
- 5.3 Quantum Magneto-Mechanical Oscillations 80

6 Magnetic Molecule Between Conducting Leads 87
- 6.1 Recent Experiments 87
  - 6.1.1 Introduction 87
  - 6.1.2 The Weak and the Strong Coupling Limit 89
- 6.2 Rotational Dynamics of the Molecule 90
- 6.3 Landau-Zener Effects in a Magnetic Molecule Bridged Between two Conducting Leads 96
  - 6.3.1 Landau-Zener Dynamics 96
  - 6.3.2 Conclusion 102

III Quantum Magnetic Deflagration 103

7 Recent Experiments 105
- 7.1 Quantum Deflagration Maxima 105
- 7.2 Effect of Dipolar Fields 109

7.2.1 Experimental Determination of the Dipolar Field in Mn_{12}-acetate 110
7.2.2 Theoretical Calculations of the Dipolar Field 115

8 Theory of Quantum Magnetic Deflagration 118
8.1 Self-Organized Patterns of Macroscopic Quantum Tunneling in Molecular Magnets 118
8.2 Computation of the Spin Relaxation Rate 120
8.3 Quantum Deflagration Fronts 126
8.3.1 Various Types of Fronts 126
8.3.2 Front Speed 128
8.4 Conclusion 130

Bibliography 132

Papers by Reem Jaafar 143

List of Figures

1.1 The spherical coordinate system used to describe the magnetic moment of a monodomain particle, $\mathbf{M}$. 4
1.2 Two classical degenerate magnetic states 6
1.3 FC and ZFC magnetization curves for γ-Fe_2O_3 [9] 10
1.4 Typical relaxation curves obtained for γ-Fe_2O_3 after field reversal [9] 11
1.5 The magnetization of an ensemble of γ-Fe_2O_3 particles versus $T\ln(t/\tau_0)$ [9] 12
1.6 The coercive field versus Temperature for $CoFe_2O_3$ particles for T from 2 to 250 K [11]. 13
1.7 The decay in time of the magnetic moment for various Temperatures for $CoFe_2O_3$ particles [11]. 14
1.8 The decay in time of the magnetic moment for various temperatures for ferritin molecules [18]. 16

2.1 The structure of the core of Mn_{12}-acetate 19
2.2 Double well potential in the absence of an external magnetic field . . 21
2.3 Magnetization of a Mn_{12}-Acetate crystal normalized by its saturation value as a function of the applied magnetic field along the c-axis for various temperatures [31]. 22
2.4 Eigenstates of the Hamiltonian in the presence and in the absence of fourth order anisotropy [31]. 23

2.5 Energy eigenvalues near the energy resonance E(m'=-2)=E(m=1) with the symmetry breaking term included [41]. 24

2.6 Energy levels of a nanomagnet with $H = -DS_z^2 - b_zS_z$ which shows the dependence of the classical energy $E = -Dm^2 - b_zm$ on the continuous variable $S_z = Scos\theta$. 27

2.7 Landau-Zener-Stueckelberg transition 29

2.8 Fe$_8$ magnetic molecule. 30

2.9 Interference of Tunneling Trajectories in Fe$_8$ 32

2.10 Unit sphere showing degenerate minima A and B which are joined by two tunnel paths (heavy lines). The hard, medium, and easy axes are taken in x, y and z direction, respectively. The transverse field is applied in the xy plane at an azimuth angle ϕ. At zero applied field, the giant spin reversal results from the interference of two quantum spin paths of opposite direction in the easy anisotropy plane yz [51]. . 33

2.11 Detailed measurement of the tunnel splitting Δ around a topological quench for the quantum transition between M = 10 and (10 n) at $\phi = 0$ for Fe$_8$, [53]. 34

2.12 Derivative of the magnetization with respect to the applied field versus the field for various temperatures [64]. 37

2.13 The dependence of the peak positions on temperature [64]. 38

3.1 Magnetization curve for a Mn$_{12}$-acetate sample. Note the sudden jump in the magnetization in the red and purple curve. 40

3.2 Signals recorded during a magnetic avalanche by Hall sensors placed on the surface near the middle of a bar-shaped sample of Mn$_{12}$-acetate. The schematic indicates the field line configuration that gives rise to the signals as the avalanche propagates from one end of the sample to the other. The inset shows sensor positions versus the time at which each sensor recorded the peak amplitude for an avalanche that started at the top and travels downward [68]. 41

3.3 A crystal of Mn_{12} molecules placed in a magnetic field opposite to the magnetic moment is equivalent to a metastable flammable chemical substance. In our case the role of the chemical energy stored in the molecule is played by the difference in the Zeeman energy $\Delta E = 2g\mu_B HS$. 42
3.4 Velocity of propagation of avalanches versus the magnetic field at which the avalanches occurred for samples whose magnetization is prepared differently, when $\Delta M/2M_{sat} = 1$, we have a full change of the magnetization whereas for zero-field-cooled conditions $\Delta M/2M_{sat} = 0.5$ [67]. 43
3.5 Velocity of propagation of avalanches versus the magnetic field. The vertical dashed line shows the position of the tunneling resonances [71]. 44
3.6 The dependence of the magnetic field that ignites deflagration on the temperature of the crystal of Mn_{12}. A is given by $A = \frac{R^2\Gamma_0 n_{-,i}}{2\kappa(T_0)/k_B}$ [70]. . 48

4.1 The Barnett Effect. 53
4.2 Root mean square (rms) cantilever deflection [82]. 55
4.3 Rotation of the crystal field due to local elastic twist at the location of the spin. 57
4.4 The geometry considered. 64
4.5 Profiles of the oscillating cantilever at different moments of time for $n = 1, 2, 3$. 67
4.6 The dependence of $P_k^{(n)}(\bar{a}, \bar{b})$ on the amplitude of the oscillations of the domain wall whose equilibrium position is in the middle of the cantilever: a) $k = 1$, b) $k = 2$. 70
4.7 The dependence of $P_k^{(n)}(\bar{a}, \bar{b})$ on the equilibrium position of the domain wall for $n = 1, 2, 3$ and $k = 1, 2$. 70

5.1 The geometry of the problem. 74

5.2 The dependence of the splitting of the first three cantilevers modes on the position of the molecule. 80
5.3 3D plots of the amplitude of oscillation at the free end as a function of $\bar{\Delta}$ and $\bar{\omega}$ when the molecule is at $\bar{y_0} = 0.9$. 83
5.4 3D plots of the amplitude of oscillation at the free end as a function of $\bar{\Delta}$ and $\bar{\omega}$ when the molecule is at $\bar{y_0} = 0.9$. It is the same as figure 5.3 but shown from a different angle. 84

6.1 (a) Side view of a Mn_{12} molecule with tailormade ligands containing acetyl-protected thiol end groups. Atoms are color labeled: manganese (orange), oxygen (dark red), carbon (gray), sulfur (yellow). The molecule diameter is about 3 nm. (b) Schematic drawing of the Mn12 molecule (red circle) trapped between electrodes. A gate changes the electrostatic potential on the molecule enabling energy spectroscopy. (c) Scanning electron microscopy image of the electrodes [103]. 88
6.2 Mn_{12} spin-10 magnetic molecule bridged between metallic leads [116]. 92
6.3 The fraction of molecules n that transit to the final state for a) fast sweep, b) slow sweep. 97
6.4 Typical time dependence of the rotation angle ϕ. The inset shows the fine structure of the oscillations. 98
6.5 The evolution of the angle ϕ when $\delta = r = 1000, \epsilon = 0.1$. The red plot is the result of the analytical solution shown in equation 6.42 whereas the blue one represents the numerical solution for φ. 100
6.6 The evolution of the angle ϕ when: a) $\delta = r = 1000, \epsilon = 0.1$; b) $\delta = 1000, r = 500, \epsilon = 0.1$. 101

7.1 Temperature required to ignite avalanches plotted as a function of magnetic field. All data were taken for field-cooled samples. The vertical lines denote the magnetic fields where sharp minima occur in the ignition temperature corresponding to thermally assisted tunneling near the top of the anisotropy barrier [64, 35]. The overall decrease in ignition temperature is due to the reduction of the anisotropy barrier as the field is increased. 107

7.2 Velocity of propagation of avalanches (right-hand yaxis) for field-cooled (filled circles) and zero-field-cooled (open circles) samples versus magnetic field at which avalanche was triggered. The triangles show the ignition temperature (lefthand y-axis). The solid vertical lines drawn from the bottom denote velocity maxima; the dashed vertical lines drawn from the top denote ignition temperature minima. The overall increase of the velocity with increasing magnetic field is due to the decrease of the anisotropy barrier. 108

7.3 Magnetization versus magnetic field of a single crystal of Mn_{12}-ac measured for an external field sweep rate of ±10 mT/s. 111

7.4 Procedure used to prepare Mn_{12}-ac with minor and major species magnetized in opposite directions. (a) First, a +6 T field is applied to align all spins. (b) Then, a −2 T field is applied, reversing the magnetization of the minor species. (c) Finally, the field is returned to zero, leaving the major and minor species spins anti-parallel. 112

7.5 (a) Magnetization of the minor species as a function of external magnetic field swept at +5 mT/s with the major species magnetization prepared following the three protocols described in the text. The triangles (squares) are data taken with the major species aligned in the positive (negative) direction. The circles are data taken with the minor species randomly oriented to yield zero magnetization. (b) The derivative of the curves shown in frame (a). 114

8.1 Moving wall of resonant spin tunneling induced by a slow sweep, for Mn_{12}-acetate. There are well-developed spatially quasiperiodic, time independent structures behind the wall [131]. 120

8.2 Thermal activation in the nonresonant case vs tunneling in the resonant case. 122

8.3 Relaxation rate $\Gamma(B_z, T)$ in a generic model of a molecular magnet when a)$B_\perp = 2$ T and b) $B_\perp = 3$ T. 125

8.4 Deflagration fronts for $\tilde{R} = 10$ and $\tilde{L} = L/l_d = 50$ as a function of τ and dimensionless spatial variables when a)$B_\perp = 2$ T and b) $B_\perp = 3$ T. 127

8.5 Deflagration front when the field is swept for $B_\perp = 2$, $\tilde{R} = 10$ and $\tilde{L} = L/l_d = 50$ and $\epsilon = 0.1$ when the added term to (8.11) is a) 0, b) slightly greater than zero. 127

8.6 Profiles of the metastable population n and the total bias $\widetilde{W}$ across the front for two values of the external bias $\widetilde{W}_{\mathrm{ext}}$: (a) $\widetilde{W}_{\mathrm{ext}} = 0$, laminar regime; (b) $\widetilde{W}_{\mathrm{ext}} = 5$, non-laminar regime. 128

8.7 Reduced front speed $\tilde{v}$ vs bias field for different values of the reduced transverse size $\widetilde{R} \equiv R/l_d$, l_d being the width of the thermal deflagration front. For such a strong applied transverse field, the effect of tunneling is dramatic. 130

Part I

Single Molecule Magnets

Introduction

In this part, we present a review on molecular magnets. We review the theory of tunneling of a large spin, we then discuss early experiments perfomed on γ-Fe_2O_3 and on antiferromagnetic ferritin which exhibited quantum tunneling. We then discuss the first experiments that presented evidence on spin tunneling in Mn_{12}-acetate, a prototypical molecular magnet of spin 10. Magnetic hysteresis curves are presented and Landau-Zener effects in molecular magnets are discussed. One important application of Landau-Zener effect resulted is the discovery of the Berry phase in Fe_8, another molecular magnet with a spin 10. We then discuss quantum classical crossover between thermally assisted and pure quantum tunneling regimes. Finally, we discuss the first two experiments perfomed to elucidate the nature of magnetic avalanches in Mn_{12}-acetate and the theory developed as a result of these experiments.

Chapter 1

History

In this chapter we review the theory of tunneling of a large spin and the early experiments performed to elucidate spin tunneling in ensembles of small particles.

1.1 The Theory of Tunneling of a Large Spin

Macroscopic quantum tunneling (MQT) corresponds to the tunneling of a macroscopic variable through the barrier between two minima of the effective potential of a macroscopic system.

Various systems such as nanomagnets with a spin of the order 10 for example, small ferromagnetic and antiferromagnetic particles and the Néel Vector in antiferromagnets exhibit various tunneling phenomena. Two decades ago, the problem has been studied for small ferromagnetic particles [1] and the probability of tunneling of the magnetization in a single domain particle between easy directions has been calculated. MQT has been thoroughly studied and explored experimentally in several systems ever since. Initially a very basic problem was solved by considering a macroscopic spin in a metastable potential. It was proven that tunneling rate can be computed by switching to imaginary time (instantantons solutions) [2]. Then Chudnovsky and Gunther [1] considered tunneling of the magnetic moment of a nanometer size single domain ferromagnetic particle with a size small enough to treat its moment as a fixed length vector that can rotate as a whole at low temperature. A certain amount of energy (the anisotropy energy) is required to rotate the spin vector as a whole.

It was shown that the monodomain magnetic particle must be firmly coupled to a solid matrix in order for it to tunnel between spin up and spin down states [3].

The tunneling of the magnetic moment in a mondomain ferromagnetic particle is given by an instanton solution of the equation of motion for $\mathbf{M}$ and perturbations around this solution.

$$\frac{\partial \mathbf{M}}{\partial t} = -\gamma \mathbf{M} \times \frac{\partial E}{\partial \mathbf{M}} \tag{1.1}$$

Equation 1.1 has been proposed by Landau and Lifshitz in 1935 [4]. If $\mathbf{M}$ has a fixed magnitude M, we characterize this vector in terms of its spherical coordinates, θ and

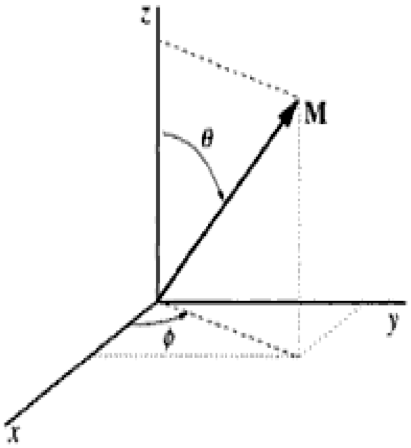

Figure 1.1: The spherical coordinate system used to describe the magnetic moment of a monodomain particle, $\mathbf{M}$.

ϕ, see figure 1.1. Equation 1.1 can then be rewritten as:

$$\frac{d\phi}{dt} = -\frac{\gamma}{Msin\theta}\frac{\partial E}{\partial \theta} \tag{1.2}$$

and

$$\frac{d\theta}{dt} = \frac{\gamma}{Msin\theta}\frac{\partial E}{\partial \phi} \tag{1.3}$$

where E(θ,ϕ) is the magnetic energy of the particle.

In order to compute the rate of tunneling **M** out of a metastable state, path integral and density matrix formalism are used [2]. For a mechanical motion, the partition function is:

$$Z = \oint D_x(\tau)exp[-\frac{1}{\hbar}\int_0^{\hbar/T} d\tau(\frac{1}{2}\dot{x}_\tau^2 + U(x))] \tag{1.4}$$

where T is the temperature of the bath with which the particle is in thermal equilibrium, U(x) is the potential and $\tau = \mathrm{i}\, t$ is the imaginary time and the integral is taken over all $x(\tau)$ trajectories that are periodic in imaginary time with the period equal to $\hbar/T$ [5]. A similar expression is found for a spin in a the spherical coordinate system

$$Z = \oint D_\theta D_\phi exp[-\frac{1}{\hbar}\int_0^{\hbar/T} d\tau(L_E)] \tag{1.5}$$

where L_E is the Euclidean magnetic Lagrangian. The latter is related to the real time Lagrangian L through $L_E = -L(t \to -\mathrm{i}\tau)$. To define L, conjugate variables are used, x(τ) and p(τ). For a fixed angular momentum, $\mathbf{L} = \mathbf{M}/\gamma$, they are: $x = \phi$ and $p = \hbar L_z = \frac{M}{\gamma}cos\theta$ and the Lagrangian is found to be:

$$L = p\dot{x} - E(x,p) = \frac{M}{\gamma}\dot{\phi}cos\theta - E(\theta,\phi) + \frac{df(\theta,\phi)}{dt} \tag{1.6}$$

Equation 1.6 can be used to deduce the equations of motion:

$$\dot{x} = \frac{\partial E}{\partial p} \quad and \quad \dot{p} = -\frac{\partial E}{\partial x} \tag{1.7}$$

f is chosen to be $f = \frac{M}{\gamma}\phi$ [6]

$$I = \int dtL = \int dt(\frac{M}{\gamma}\dot{\phi}(cos\theta - 1) - E(\theta,\phi)) \tag{1.8}$$

is the area on the sphere of radius S swept by the total spin $\mathbf{S} = \gamma^{-1}\mathbf{M}$ as it makes a closed path around the north pole of the sphere. It is also known as Berry's phase. D. Loss, D. P. DiVincenzo, G. Grinstein [7] and J. von Delft, C. L. Henley [8] have studied the significance of this term to quantum tunneling. He has proven that for a wide class of ferromagnetic and antiferromagnetic systems, quantum tunneling of the magnetization direction is spin-parity dependent: it vanishes for magnetic particles with half-integer spin but is allowed for integer spin. Chudnovsky and Gunther [1] calculated the probability of tunneling for several forms of the magnetic anisotropy.

If we consider a uniaxial single domain particles with the anisotropy along the Z-axis, in a transverse magnetic field applied along the X-axis, then

$$E = V(K sin^2\theta - HM_0 sin\theta cos\phi + \frac{H^2M_0^2}{4K}) \tag{1.9}$$

For $H < H_c = 2K/M_0$, the energy 1.9 has two minima (E=0) corresponding to $\phi = 0$ with $\theta = \theta_0$ and $\theta = \pi - \theta_0$ where $\theta_0 = H/H_c$.

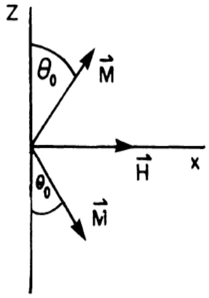

Figure 1.2: Two classical degenerate magnetic states

These positions are shown in figure 1.2. The energy barrier between the two states is $U = K\epsilon^2$ where $\epsilon = 1 - H/H_c$. At $H = H_c$, when $\theta_0 = \pi/2$, the two equilibrium orientations of $\mathbf{M}$ meet on the X-axis and the barrier disappears.

Equations 1.2, 1.3 and 1.9 yield an equation for θ in τ:

$$\frac{d^2\theta}{d\tau^2} = \omega_H^2[1+\omega_H^{-2}(\frac{d\theta}{d\tau})^2]cot\theta - 2\omega_1\omega_H[1+\omega_H^{-2}(\frac{d\theta}{d\tau})^2]^{1/2} cos\theta \tag{1.10}$$

where $\omega_H = \gamma H$ and $\omega_1 = \gamma K/M_0$. In the limiting case of a very low field, $\theta_0 \to 0$, the approximate solution of 1.10 corresponding to the switching of $\mathbf{M}$ from $\theta = \pi$ at $\tau = -\infty$ to $\theta = 0$ at $\tau = \infty$ is given by

$$\theta = arccos[tanh(\omega_1\tau)] \tag{1.11}$$

If the action of this trajectory is calculated and keeping in mind that the tunneling rate P is given by $P = A\, exp[\mathrm{i}I/\hbar]$, P is found to be proportional to $(H/Hc)^{2M_0/(\hbar\gamma)}$. As $H \to 0$, P goes to zero and as $H \to H_c$, it is shown that [1] P is proportional to $exp[-(4M_0/(\hbar\gamma))\epsilon^{3/2}]$ which means that the tunneling rate is proportional to $(H/H_c)^{2S}$. This follows from the fact that the transition between $S_z = S$ and $S_z = -S$ appears in the 2S order of the perturbation theory of the transverse field H. This idea will be revisited in the next chapter when we discuss quantum magnetic hysteresis in molecular magnets.

1.2 Early Experiments on Spin Tunneling

1.2.1 Ensembles of Small Particles

At a given temperature any magnetic system has a certain state that corresponds to the absolute minimum of its free energy. Particles in several systems (such as monodomain particles embedded within a non magnetic solid matrix) can be in a metastable state due to energy barriers produced by the magnetic anisotropy. The presence of metastable states results in magnetic hysteresis and all magnetic systems that exhibit hysteresis are expected to relax slowly toward the minimum of the free energy. It is important to note that slow relaxation toward the thermodynamic equilibrium is a non-linear effect and its long duration is due to the exponentially large lifetimes of metastable states [2].

At a high enough temperature the relaxation proceeds over the local barrier due to thermal fluctuations. Below we develop the necessary equations needed to understand the relaxation of the moment of a system of identical non-interacting single-domain particles frozen in a non-magnetic solid matrix whose axes are parallel to each other and to the external magnetic field.

If M_+ and M_- are the total moments due to particles whose moments are aligned along and against the field respectively, then they must satisfy the following equations.

$$\frac{dM_+}{dt} = -\Gamma_+ M_+ + \Gamma_- M_- \quad and \quad \frac{dM_-}{dt} = -\Gamma_- M_- + \Gamma_+ M_+ \tag{1.12}$$

where $\Gamma\pm$ are the rates of transition out of a given state. For thermal transitions, we have $\Gamma\pm = \nu_\pm exp[-K_\pm(H)V/T]$. If the total moment of the system is $M = M_+ - M_-$ and if we consider uniaxial particles whose axes are aligned with the field $K_\pm = K(1 \pm H/H_a)^2$, then

$$M(t) = M_{eq} + (M_0 - M_{eq})exp(-\Gamma t) \tag{1.13}$$

where

$$M_{eq}(H) = \frac{\Gamma_- - \Gamma_+}{\Gamma_- + \Gamma_+} M_s \tag{1.14}$$

is the equilibrium moment and $M_s = M_+ + M_-$ is constant and is the total moment at saturation, $M_0 = M(t = 0)$ and $\Gamma = \Gamma_- + \Gamma_+$.

Similar expressions were found for uniformly oriented non-interacting uniaxial particles with the same magnetization and anisotropy energy per unit volume but with the distribution of volume, f(V), in that case $exp(-\Gamma t)$ in 1.13 is replaced by

$$\frac{\int_0^\infty dV f(V) V exp[-\Gamma(V)t]}{\int_0^\infty dV f(V) V} \tag{1.15}$$

and for thermal relaxation

$$\Gamma = \nu_- exp[-K_-(H)V/T] + \nu_+ exp[-K_+(H)V/T] \tag{1.16}$$

In experiment, νt is of the order of 10^{11} to 10^{15} so that the exponential factor under the integral in 1.15 is $\Theta(V - V_B)$ where V_B can be approximated by a step function:

$$V_B = \frac{T}{K_-(H)} \ln(\nu_- t) \tag{1.17}$$

and thus M(t) can be written as

$$M(t) = M_{t_0} - (M(t_0) - M_{eq}(H))\frac{\int_0^{V_B} dVf(V)V}{\int_0^{\infty} dVf(V)V} \tag{1.18}$$

V_B can be called blocking volume. At a time t only particles with volume $V_B(t)$ can contribute to the relaxation: smaller particles have already relaxed and bigger particles have their moment blocked in the initial direction. In most relaxation experiments, the field is small compared with the anisotropy field and the dependence of the energy barrier on the field and the orientation of the particle can be neglected.

It is assumed that f(V) changes slower than exponentially in the vicinity of V_B so that in the thermal relaxation case, M depends on time only through the combination $T\ln(\nu t)$. It is shown that $T_B = \frac{KV_0}{\ln(\nu t)}$ where T_B is the blocking temperature and f(V) dV drops rapidly above a certain value called V_0. t is the characteristic measurement time of the instrument and depends on the instrument. On that time-scale, the transitions in most particles unfreeze above T_B. The condition $T << T_B$ (below the blocking temperature) is equivalent to $V_B << V_0$ and only the magnetization confined within particles of volume V_B is relaxing whereas in the bigger ones it is frozen. Based on the arguments above, $\ln(t)$ relaxation is expected at $T << T_B$ and ceases at $T \geq T_B$. In the next section we explore the results of relaxation experiments that were performed for various particles.

1.2.2 Experiments on Spin Tunneling

Relaxation measurements have been performed in order to detect change in the total moment. Typically experimentalists collect data for the magnetization when the sample is field cooled (FC) or zero field cooled (ZFC). FC data correspond to an experiment in which the system was initially cooled down in the presence of a weak magnetic field, then it was slowly warmed up and the magnetization data were taken. The ZFC data are typically taken when the sample is initially cooled in the absence of a field then a small field was applied and the data were taken as the temperature was slowly raised.

One of the earliest experiments on slow relaxation in small particles was done by Vincent el al [9] using small (average of 4 nm) γ-Fe_2O_3 particles. Electron microscopy has shown the particles to be nearly spherical with diameter distribution around a peak value of 4.2 nm. The Curie temperature of the sample is around 863 K. Mutual interactions between particles was weak. A magnetization curve was obtained around 4.3 K and FC and ZFC magnetization curves are shown in 1.3. M_0 is the residual magnetization that was obtained from a magnetization curve as a function of the applied field at 4.3 K. It was subtracted from M to emphasize the effect of the 300 Oe field. The blocking temperature can be deduced from the peak of the ZFC curve.

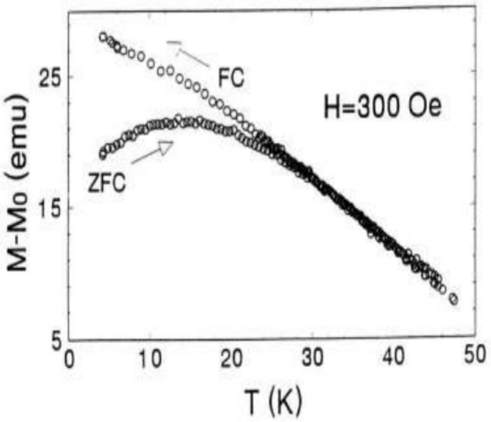

Figure 1.3: FC and ZFC magnetization curves for γ-Fe_2O_3 [9]

From figure 1.3 it can be seen that for the FC curve as temperature increases, the moments of the particles begin to flip leading eventually to thermal equilibrium whereas for the ZFC curve the initial moment is zero and the moments of bigger and bigger particles progressively flipped towards the direction of the field until the blocking temperature when it goes down according to the equilibrium law [10]. From $t = \tau_0 exp(KV_B)/T$, and using values of $T_B = 13K$ determined from the hysteresis curve with t ˜ 1000 s and $\tau_0 = 10^{-10}s$ one can estimate V_B to be around $6.7{*}10^{-20}cm^3$. This volume is equivalent to spherical particles of diameter 5 nm in accordance with electron microscopy.

Magnetic relaxation was measured by heating the sample to 50 K in a 300 Oe field. It was then cooled to low temperature (<12 K) and no relaxation was detected. The field was then reversed from 300 Oe to -300 Oe and the sample was allowed to relax towards equilibrium. Magnetization data were recorded right after reversing the field. Relaxation curves are shown in 1.4.

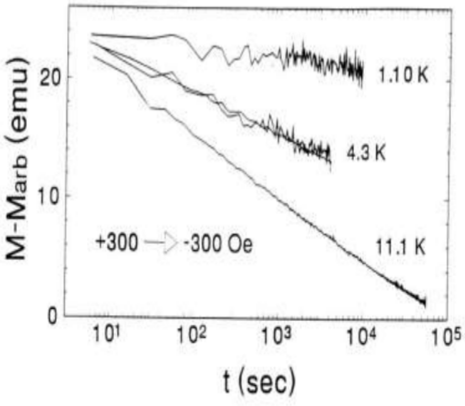

Figure 1.4: Typical relaxation curves obtained for γ-Fe_2O_3 after field reversal [9]

A plot of M versus $T\ln(t/\tau_0)$ should yield a universal curve for data collected at various temperatures for purely thermal relaxation. This was achieved for γ-Fe_2O_3 [9], as shown in 1.5. This experiment provides a good example of thermal behavior of small particles and can help understand how to detect quantum tunneling if there is deviation from this thermal behavior. Another experiment was performed on

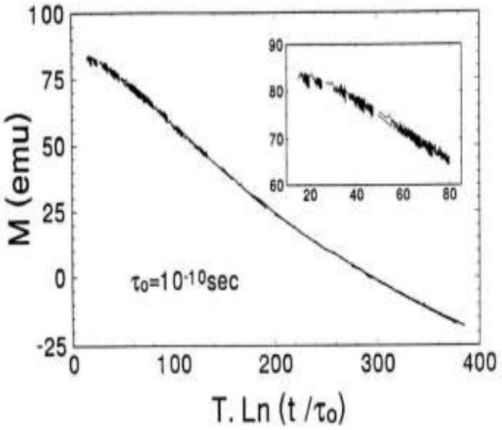

Figure 1.5: The magnetization of an ensemble of γ-Fe_2O_3 particles versus $T\ln(t/\tau_0)$ [9]

$CoFe_2O_3$ ferrimagnetic particles of average diameter 3.5 nm [11]. The Curie temperature was 793 K and so no detectable change in the spin structure was expected at low temperature. A magnetic hysteresis study at 250 K shows that the coercive field is very low (few Oe), hence one can conclude that at high temperature the system is superparamagnetic. A study of the coercive field versus temperature shows that as the temperature is lowered, the value of the coercive field increases.

Figure 1.6 shows that more particles become superparamagnetic as the temperature is raised. Since the coercive field does not saturate for low temperature one can conclude that thermal blocking of the smallest particles persists down to 1.8 K which makes it interesting to investigate quantum tunneling. A magnetic hysteresis data was taken at 2.4 T from which the authors in [11] estimated the bulk anisotropy field to be about 1 T whereas the highest anisotropy field inside the particles was found to be close to 5 T. This suggests that the anisotropy of the particles is of crystalline

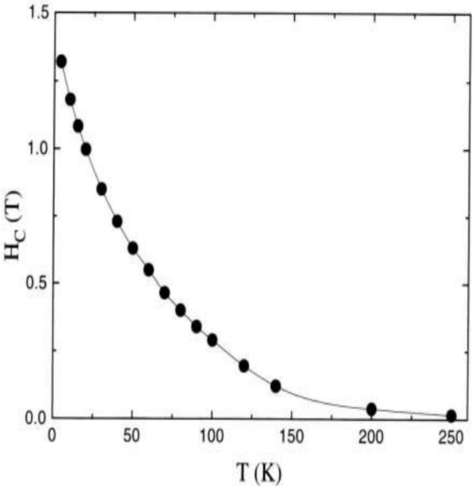

Figure 1.6: The coercive field versus Temperature for $CoFe_2O_3$ particles for T from 2 to 250 K [11].

origin. The anisotropy field is greater by a factor of 10 than that for γ-Fe_2O_3 particles (anisotropy field was about 5000 Oe) which brings the crossover from thermal to the quantum regime into the kelvin range. Several conclusions were drawn from the study:

a. FC and ZFC curves were given for $H = 0.01$ T and $H = 0.4$ T, the higher the value of the field the lower the value of the blocking temperature which is found by locating the peak of the ZFC curve.

b. The value of the blocking temperature for low field was about 300 K from which the barrier height was estimated to be 30 $T_B \approx 770$ meV.

c. Magnetic relaxation measurements were performed for temperatures between 8 K and 1.8 K by cooling the sample down from 300 K at 5000 Oe and then reversing the field. It was found that the lower the temperature the smaller the fraction of the total magnetization that is relaxing during the observation time see figure 1.7. This is expected because at lower temperatures, bigger particles are blocked and smaller size particles will contribute to the magnetization.

d. A plot of M versus $T\ln(T/T_0)$ for $CoFe_2O_3$ for temperatures below 5 K reveals a systematic departure from the universal curve, and the authors of [11] attribute that as evidence for quantum tunneling and estimate the crossover from thermal to the quantum regime to occur in the range 2.5 to 5 K.

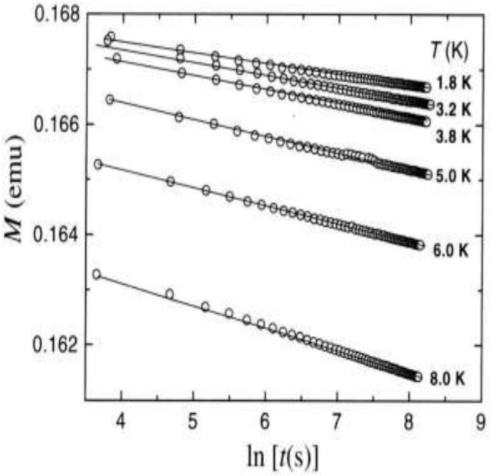

Figure 1.7: The decay in time of the magnetic moment for various Temperatures for $CoFe_2O_3$ particles [11].

1.3 Tunneling in Antiferromagnetic Ferritin

B. Barbara and E. M. Chudnovsky have studied macroscopic quantum tunneling in antiferromagnets [12]. Starting from the Néel state of a uniaxial antiferromagnetic particle, they showed that, due to the tunneling of the Néel vector between easy directions, the ground state of a sufficiently small particle is a quantum superposition of two equivalent Néel states. Awschalom et al. explored this effect in horse-spleen

ferritin [13]. Ferritin is an iron-storage protein that has a spherical cage of diameter of about 8 nm that contains the mineral ferrihydrate combined with a phosphate [2]. Its core is equivalent to a small antiferromagnetic particle α-Fe_2O_3. Mössbauer studies have predicted a superparamagnetic behavior at high temperature and a blocked magnetic state at low temperature with the blocking temperature between 10 K and 15 K [14, 15]. Low-field magnetic susceptibility data of ferritin also confirmed its antiferromagnetic structure [16]. FC and ZFC data obtained by the authors of [16] have shown that the particles are superparamagnetic above 13 K. The size of the particles was estimated to be 7 nm and was in agreement with the upper limit on the size of hematite core [2]. Other works have proven that the blocking temperature T_B is proportional to V [17] in agreement with the formula $T_B = E_a V/30$.
Other works focused on AC measurements of the blocking effects [18]. Below the Néel temperature the particles should appear magnetically ordered depending on the period of the AC field. In that case $T_B = -U/(\ln \omega t_0)$ and a plot of $\ln(1/f)$ vs $1/T_B$ show a straight line [18].
Measurements of M versus $\ln(t)$, like the case of $CoFe_2O_3$ shows a straight line and proves its logarithmic character [18]. This is in agreement with the broad distribution of sizes deduced from Mössbauer measurements [14, 15]. A small part of the total magnetization relaxes below 4 K, which suggests that the relaxation is due to the presence of the smallest particles just as in $CoFe_2O_3$ see figure 1.8.

It was estimated [2]that the crossover temperature from the thermal to the quantum regime to be around 5 K or less. Subsequent AC susceptibility measurements have supported the hypothesis that below 2 K the magnetic relaxation is due to quantum tunneling [19].

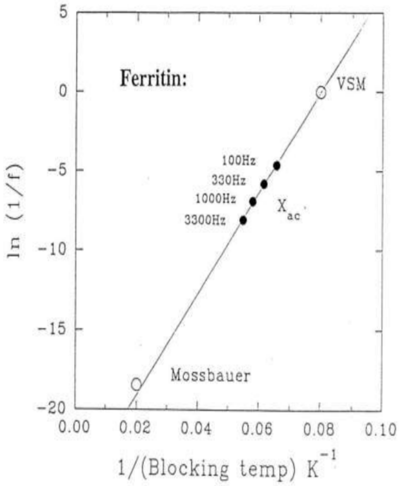

Figure 1.8: The decay in time of the magnetic moment for various temperatures for ferritin molecules [18].

Several arguments, presented below explain evidence of magnetic quantum tunneling in ferritin [2].

a. Several reports have estimated the anisotropy constant and they were all consistent [20, 16, 17].

b. High frequency magnetic noise and susceptibility measurements show resonance in R(ω) (the noise) and in the susceptibility [13]. However measurements of the same quantities on an undiluted sample failed to show any resonance structure. The aim was to observe a resonance in the absorption spectrum of ferritin that corresponds to the tunnel splitting of the ground state level.

c. There is evidence for the exponential dependence of the tunneling rate on the volume.

The problem with ferritin is that for successful resonant experiments, it is hard to expect uniform size distribution of ferritin particles needed to produce a unique value of the tunnel splitting Δ. Molecular magnets, which is the topic of the next chapter, provided lot of excitement for scientists to study the problem of MQT as it consisted of identical particles.

Chapter 2

Spin Tunneling in Molecular Magnets

Molecular magnets solved the problem of unique size distribution for an ensemble of particles and became the ideal system to study spin tunneling. In this chapter, we focus on spin tunneling in molecular magnets, in particular in Mn_{12}-acetate. Quantum magnetic hysteresis, tunnel splitting and the effect of the sweeping field are discussed. We end the chapter by studying the crossover between thermally assisted tunneling and pure quantum tunneling.

2.1 Quantum Magnetic Hysteresis

2.1.1 Mn_{12}-Acetate

Magnetic molecules are an interesting area for investigating magnetic quantum tunneling. We focus this section on the properties of Mn_{12}-Acetate which is a prototypical single molecule magnet to help us understand quantum tunneling properties in subsequent sections. Mn_{12}-Acetate was first synthesized by Lis in 1980 [21]. However few experiments were performed on samples of Mn_{12}-Acetate until its large magnetic moment and magnetic bistability were recognized [22, 23]. A Mn_{12}-Acetate molecule has a spin 10 rigid at low temperatures. It is equivalent to a very small single domain magnetic particle. It has a very large anisotropy with the barrier of the order of 60 K [23]. The presence of the barrier causes a relaxation time τ that obeys an Arrhenius law. The blocking temperature was estimated to be about $T_B = 3$ K [22, 25, 26, 27, 29].

X-ray diffraction methods were used to find the characteristics of Mn_{12}-Acetate samples [21]. It was shown that the molecular crystal has a tetragonal symmetry with lattice parameters $a = 1.732$ nm and $b = 1.239$ nm. The molecule possesses S_4 symmetry and has tetrahedral core of four Mn^{4+} ions at its center surrounded by a crown of eight Mn^{3+} ions as shown in 2.1.

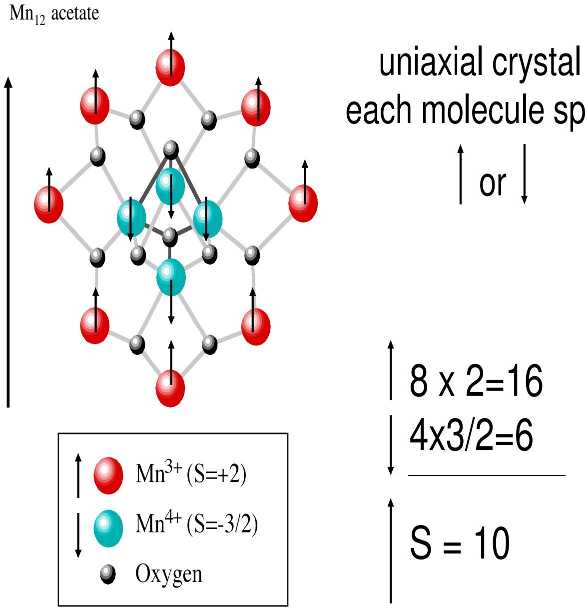

Figure 2.1: The structure of the core of Mn_{12}-acetate .

Each of the Mn^{3+} ions has spin 3/2 whereas each of the Mn^{4+} ions has spin 2.

The spins of the Mn ions are coupled through oxygen ligands which allow an indirect exchange interaction between them. Magnetism of the molecule is of pure spin origin. The value of g was found to be 1.9 from ESR studies [122]. In single molecule magnets (SMM), for example in Mn_{12}-Acetate, the molecules are relatively far apart so that the magnetic exchange between them is small and they only interact very weakly. At low temperature, SMMs in general behave as single rigid spins. As the temperature is lowered, the spin reversal process in SMM evolves from thermal activation to pure quantum tunneling.

Because the molecule has a strong uniaxial anisotropy along the c-axis, to a first approximation, one can write its Hamiltonian as:

$$H = -DS_z^2 - g\mu_B \mathbf{S} \cdot \mathbf{H} \tag{2.1}$$

where the z-direction is taken to be along the c-axis. ESR measurements [122] have provided a value of D close to 0.6 K.

When H= 0, the energy barrier is $U = DS_z^2 = 60$ K. The blocking temperature can then be estimated to be around 3 K, in accordance with experimental measurements of the ZFC magnetization curve [24] and so above 3 K thermal energy is available for the magnetization to achieve equilibrium and no hysteresis behavior is expected to be observed in the magnetization curve.

Equation 2.1 can include higher order longitudinal anisotropy term such as A S_z^4 and A is estimated to be around A $= 1.173 \times 10^{-3}$ K.

The spin's energy is a double-well potential where one well corresponds to the spin pointing up and the other one corresponds to the spin pointing down as shown in figure 2.2.

The effect of applying an external magnetic field would be to unbalance the double well shown in figure 2.2. For the simple Hamiltonian given by equation 2.1 the level crossings corresponding to each resonance occur pairwise at the same value of the magnetic field: every level in the left well simultaneously crosses a level in the right well at a certain value of the magnetic field. When higher order anisotropy terms are introduced in equation 2.1 such as A S_z^4, the level crossings would not correspond

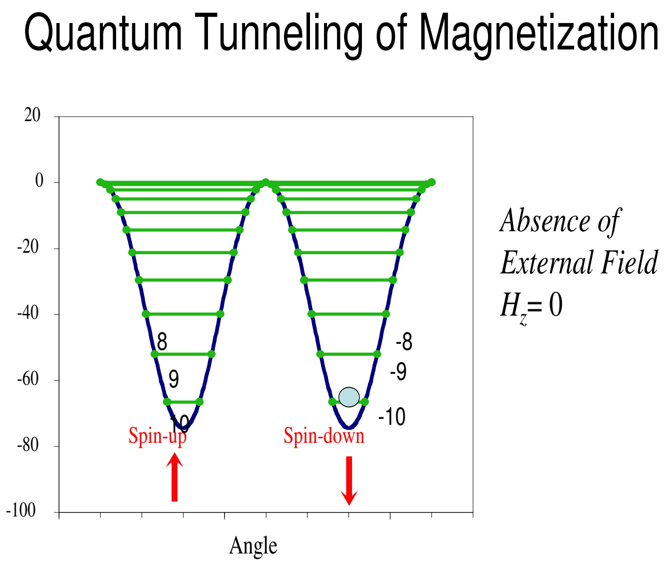

Figure 2.2: Double well potential in the absence of an external magnetic field .

exactly at the same value of the field and a structure is introduced in each step.

2.1.2 Quantum Tunneling in Single Molecule Magnets

Magnetic hysteresis curves for Mn_{12}-Acetate have been published by several researchers [29] before Friedman et al. [24] observed the regular jumps in the magnetization curve. Examination of the Hamiltonian 2.1 shows that tunneling is impossible unless a symmetry breaking term that does not commute with S_z is added to equation 2.1 so that a modification of 2.1 that exhibits tunneling is:

$$H = -DS_z^2 - g\mu_B \mathbf{S} \cdot \mathbf{H} + H' \tag{2.2}$$

where H' can be written as:

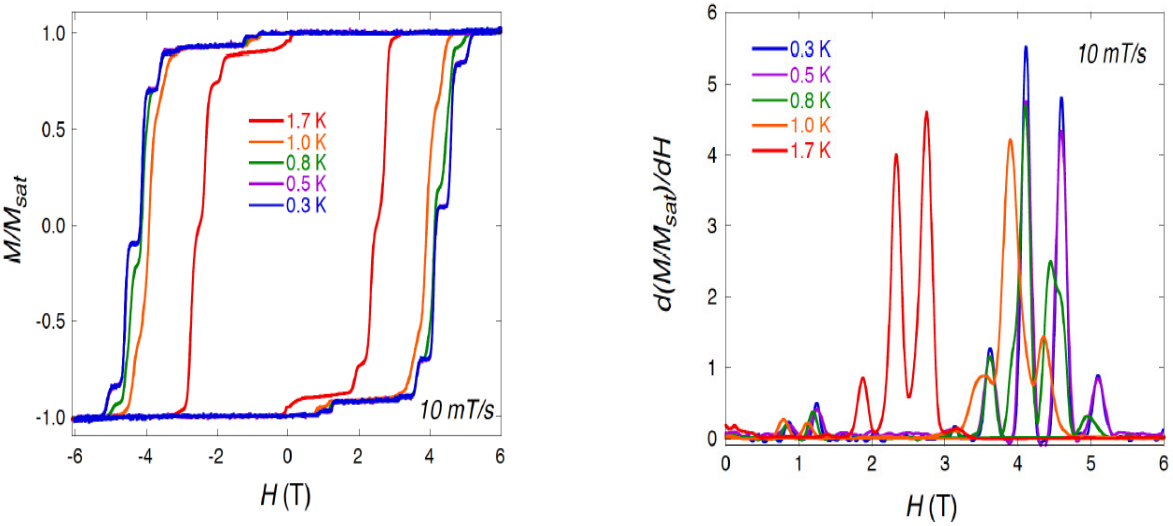

Figure 2.3: Magnetization of a Mn_{12}-Acetate crystal normalized by its saturation value as a function of the applied magnetic field along the c-axis for various temperatures [31].

$$H' = -g\mu_B H_x S_x + E(S_x^2 - S_y^2) + (C/2)(S_+^4 + S_-^4) + ... \tag{2.3}$$

The first term includes hyperfine, dipolar and externally applied transverse field. The second term on the right-hand side is the second order transverse anisotropy that is present in many low-symmetry SMMs. The third term is the fourth-order transverse anisotropy. Experimental measurements [30] on Mn_{12}-Acetate show steps in the magnetization curve, see figure 2.3. The first term in equation 2.3 allows tunneling for each level crossing. The second term allows tunneling for $\Delta m = 2$ and the third term allows tunneling for $\Delta m = 4$ where m is given by $S_z|m >= m|m >$ Dipolar fields alone are very weak to cause tunneling [30].

Experimental and theoretical work have traced the source of tunneling to isomer disorder in Mn_{12}-Acetate[32, 33, 116, 35, 36, 37, 38, 39, 40]. It was shown that the most relevant term in equation 2.3 is the term H_x and it is the term that causes spin tunneling in Mn_{12}-Acetate.

2.2 Landau Zener Effects in Molecular Magnets

2.2.1 Tunnel Splitting

As mentioned in the previous section, a symmetry breaking term in the Hamiltonian such as, for e.g. H_x, is needed in order for the spin to tunnel. Consider for example the following spin Hamiltonian for

$$H = -DS_z^2 - AS_z^4 - g\mu_B S_z H_z + g\mu_B S_x H_x \tag{2.4}$$

Figure 2.4 shows the eigenstates of the 2.4 in the presence and in the absence of the term A S_z^4.

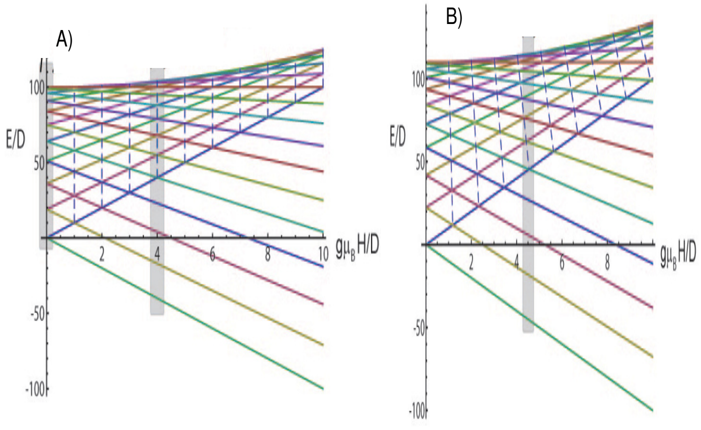

A) Energy of spin projection states versus the applied magnetic field in the absence of the 4th order anisotropy term. B) Energy levels versus the applied magnetic field in the presence of the 4th order anisotropy term AS_z^4. The vertical shaded line clearly shows that all level pairs cross simultaneously when AS_z^4 is absent.

Figure 2.4: Eigenstates of the Hamiltonian in the presence and in the absence of fourth order anisotropy [31].

If the Hamiltonian does not contain the symmetry breaking term $g\mu_B S_x H_x$, m is a good quantum number since H_z commutes with the Hamiltonian. When $g\mu_B S_x H_x$ is included, the situation is different. In that case, for fields that do not place the system near resonance, the eigenstates of the full Hamiltonian given by 2.4 are accurately given by the eigenstates of the unperturbed Hamiltonian (that is m can still be used as a good quantum number). For fields that do place the system near resonance, mixing occurs between the two states that are near the resonance [10].

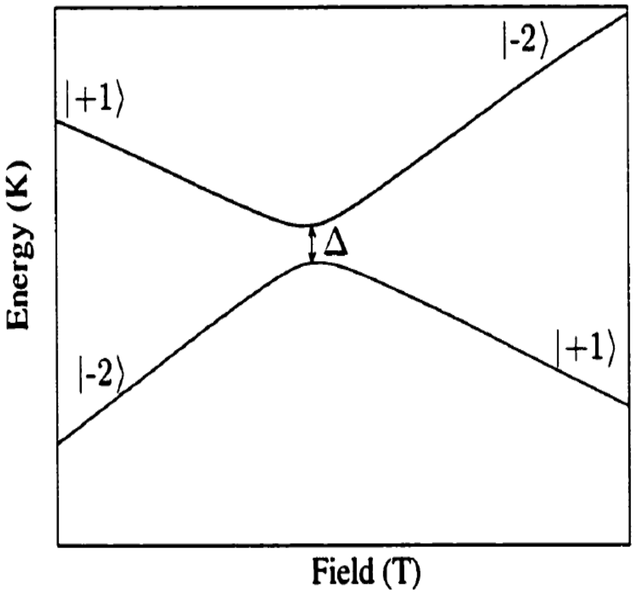

Figure 2.5: Energy eigenvalues near the energy resonance E(m'=-2)=E(m=1) with the symmetry breaking term included [41].

Consider for example the energy of the levels at first resonance between m'=-2 and m=1 see figure 2.5, [41]. If the field is below the resonance field, the lower curve corresponds to eigenstate $|-2>$ and the upper one to eigenstate $|+1>$, however above resonance, one can see that the lower curve now corresponds to eigenstate $| + 1 >$ while the upper one corresponds to eigenstate $| - 2 >$. The gap formed between the eigenvalues near a transition is called the tunnel splitting. Garanin has shown that the tunnel splitting can be calculated using perturbation theory that we shall explore next [42].

2.2.2 A Perturbative Approach to Spin Tunneling

Consider, for e.g. the following Hamiltonian

$$H = -DS_z^2 - b_x S_x \tag{2.5}$$

where $b_x = \gamma \hbar H_x$. The term b_x causes tunneling. Consequently, the magnetic moment of a nanoparticle that was initially prepared in a state m can tunnel under the barrier to the state -m and back. For small values of b_x the problem is essentially reduced to a two-state problem with known solution [43, 10]. The tunneling splits the degenerate level $E_m = -Dm^2$ into two levels of energies $E_{m\pm} = E_m \pm \Delta_m/2$. The corresponding eigenstates are:

$$\psi_{m\pm} = \frac{1}{\sqrt{2}}(|m > \mp | -m >). \tag{2.6}$$

If the system was initially prepared in the state m or -m the tunnel splitting Δ_m determines the frequency of the oscillation, $\omega_m = \Delta_m/\hbar$ between m and -m. Garanin computed Δ_m using perturbation theory for small b_x [42]. Using the fact that the second term in 2.5 the second term has non-zero matrix elements only between neighboring states,

$$V_{m+1,m} = V_{m,m+1} =< m|b_x S_x|m+1 >= \frac{1}{2} b_x l_m \tag{2.7}$$

where $l_m = \sqrt{S(S+1) - m(m+1)}$. Tunneling between $\pm m$ states appears in the $2|m|$-th order of the perturbation theory on $b_x S_x$ and Δ_m is found to be:

$$\Delta_m = 2D \frac{b_x}{2D} \prod_{n=m+1}^{2|m|-m-1} \frac{1}{m^2 - n^2} \prod_{n=m}^{-m-1} l_n = \frac{2D}{((-2m-1)!)^2} \frac{(S-m)!}{(S+m)!} (\frac{b_x}{2D})^{2|m|} \tag{2.8}$$

Equation 2.8 can be simplified further for the limiting case of $1 \ll |m| \ll S$. The problem can be modified to include the Zeeman term $b_z S_z$. In that case, equation 2.5 becomes:

$$H = -DS_z^2 - b_x S_x - b_z S_z \tag{2.9}$$

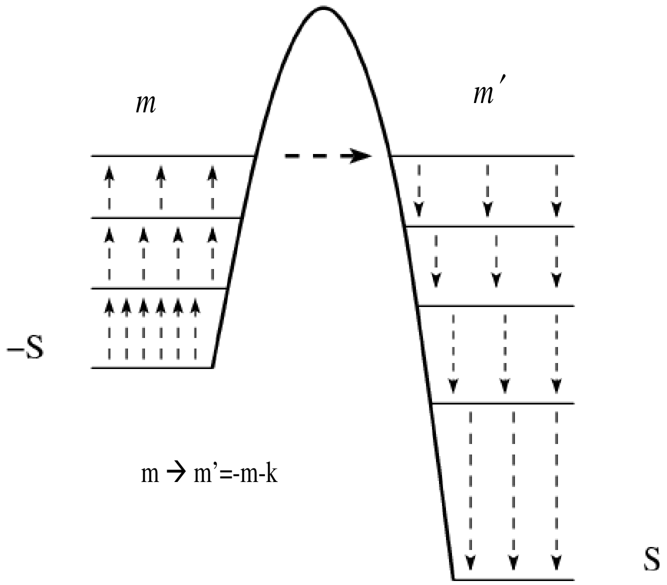

Figure 2.6: Energy levels of a nanomagnet with $H = -DS_z^2 - b_zS_z$ which shows the dependence of the classical energy $E = -Dm^2 - b_zm$ on the continuous variable $S_z = Scos\theta$.

As discussed earlier, the degeneracy of the m-states is removed and there is an incidental degeneracy for pair of levels $m < 0$ and $m' = -m-k$ if b_x is to be ignored.

At resonance, for $b_x \neq 0$ the $E_m = E_{m'}$ level splits into two levels separated by $\Delta_{mm'}$. Similar calculations can be done for equation 2.9 and in that case it is found that [10]:

$$\Delta_{m,m'} = \frac{2D}{[(m'-m-1)!]^2}(\frac{b_x}{2D})^{m'-m}\sqrt{\frac{(S+m')!(S-m)!}{(S-m')!(S+m)!}} \tag{2.10}$$

2.2.3 Probability of Tunneling in a Field-Swept Experiment

As discussed in section 2.2.1, the eigenstates exchange character when crossing the resonance in a field swept experiment. There is a probability for the molecule which was originally in the metastable well to tunnel to the stable well because of the presence of the symmetry breaking term. Since the wavefunction must obey the time dependent Schrödinger equation, time-dependent perturbation theory can be applied when the field is swept quickly or slowly. In the case when the field is swept quickly, the wave function cannot change in a timely manner. In the case of the example shown in section 2.2.1, the system that was originally in $|-2>$ before resonance will still be in that state after crossing the resonance. This implies that the molecule remains in the metastable well and there is no tunneling [41]. In the other limit, when the field changes slowly, the wavefunction will have time to evolve so that he system that was originally in $| - 2 >$ before crossing the resonance will transit into the $| + 1 >$ after crossing the resonance. In between the two approximations comes the Landau-Zener-Stueckelberg (LZS) solution. It is the exact solution to the Schrödinger equation for a two-state system whose diagonal terms change linearly with time and off-diagonal symmetry breaking terms that are constant [44, 45, 46]. If a certain energy level is occupied by N molecules before it comes into resonance with an unoccupied level, we want to know the fraction of the N molecules that will remain at the initially occupied level after the resonance is crossed see figure 2.7.

When the tunnel splitting Δ between the two levels is small compared to the distances to all other energy levels, the probability P for the molecule to remain in the initial state is given by

$$P = exp(\frac{-\pi\Delta^2}{2v\hbar}) \tag{2.11}$$

and the probability for the molecule to transit to the final state is given by 1 - P(t). v is the rate at which the energy levels approach each other $v = W(t)/t$ where $W(t)$ is the sweep rate. One can see from equation 2.11 that the slower the field is swept the higher is the probability of tunneling and that for very fast sweep rate, P approaches 1, in accordance with the expectation that the spins do not have enough time to

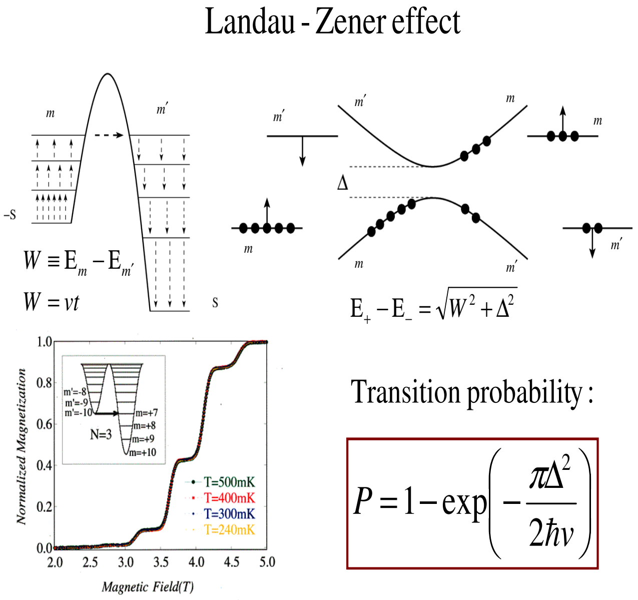

Figure 2.7: Landau-Zener-Stueckelberg transition

tunnel.

2.3 Berry Phase in Molecular Magnets

In the previous sections we have focused our attention on Mn_{12}-Acetate. It has uniaxial anisotropy which makes it easy to be studied symmetry-wise. Another widely used SMM is Fe_8. Like Mn_{12}-Acetate, it also has a spin ground state of 10. The energy levels can also be modeled by a double well potential. Its symmetry is, however, very different from that of Mn_{12}. Fe_8 has three inequivalent axes: it possesses a biaxial (rather than a uniaxial as the case of Mn_{12}-Acetate) anisotropy. The anisotropy barrier in Fe_8 is about 22 K and shows resonant tunneling steps in the hysteresis loops [47, 48].

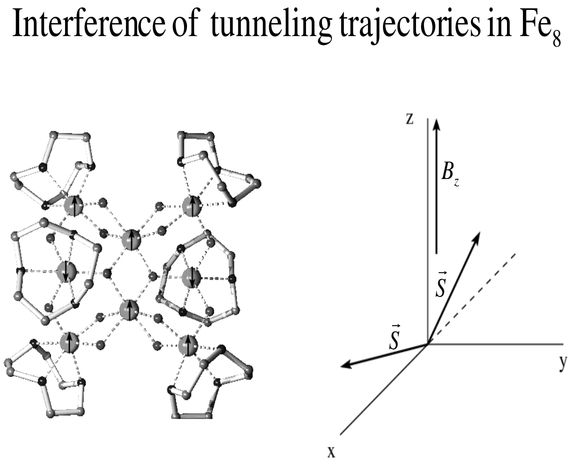

Figure 2.8: Fe$_8$ magnetic molecule.

As shown in figure 2.8 Fe$_8$ possesses three inequivalent directions, providing a hard axis x and a medium axis y within the hard plane. In this case, the most relevant term from equation 2.3 is $E(S_x^2 - S_y^2)$ which indicates that in the absence of a magnetic field, the spin has two preferred tunneling paths through the y and -y directions.
A Berry phase is the phase acquired over the course of a cycle when a system is subjected to a cyclic adiabatic process resulting from the geometrical properties of the parameter space of the Hamiltonian. A typical example is the Aharanov-Bohm effect in which a charged particle experiences a phase shift due to the enclosed magnetic field despite the magnetic field being zero in the region through which the particle passes.

In the case of SMMs, when a spin's orientation traverses a closed path, it acquires a geometric phase proportional to the solid angle enclosed by that path. In particular, Fe_8, which has a biaxial spin anisotropy, must have two least-action tunneling paths for spin reversal. Each path acquires a different geometric phase and these paths will therefore interfere [31].

In 1993, Garg [49, 50] predicted that a magnetic field could be used to modulate the geometric-phase interference that is a magnetic field can change the geometric phase difference between tunneling paths, therefore altering the interference. He subsequently studied the oscillation in the tunneling rate with magnetic field for magnetic quantum tunneling problem [50]. It was shown that the tunnel splitting can be modulated by a factor cos (S Ω) where Ω is the angle circumscribed by the two paths. As the field increases, Ω decreases and destructive interference occurs for $S\Omega = (2n + 1) \times \pi/2$ for integer n. The predicted field interval between zeros is: $\Delta H = \frac{2}{g\mu_B}\sqrt{2E(E + D)}$.

In 1999 Wernsdorfer and Sessoli discovered interference effect in Fe_8 [51]. They used Landau-Zener tunneling method by rapidly sweeping the longitudinal field through a tunneling resonance, to determine the tunnel splitting Δ of that resonance.

In their work they assumed that the cluster has a large anisotropy with a strong transverse component, which makes x the hard axis. If the magnetization is prepared by saturating along $+z$ axis, when the field is switched off the system must return to equilibrium by switching between the ± directions. The rotation will occur preferentially in the yz plane, and it can be either clockwise or anticlockwise.When a transverse field is applied, the two minima A and B are still connected by two paths, which depend on the strength of the transverse field and its orientation in the xy plane see figure 2.10. If the two paths are in phase there will be a reinforcement and a tunnel splitting will result, while if they are dephased by $\pi/2$ then the splitting will be quenched. These topological interferences are also known as Berry phases [52, 51]. The results are shown in figures 2.9, 2.10.

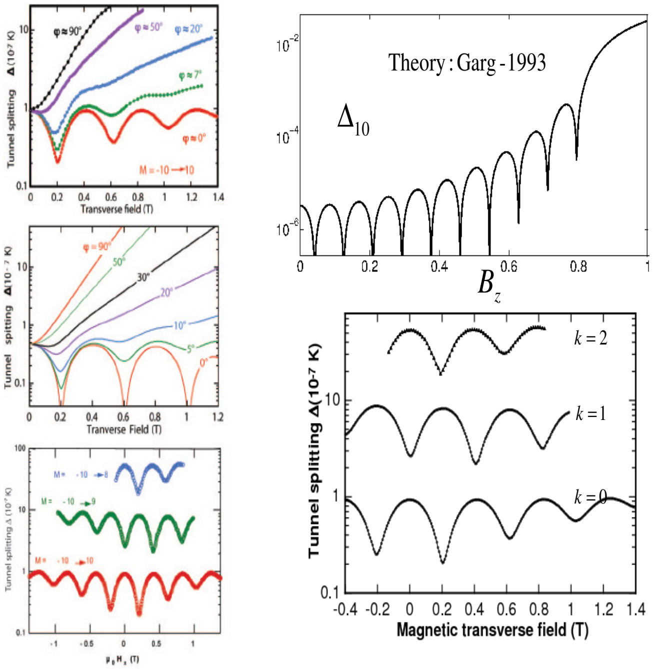

Figure 2.9: Interference of Tunneling Trajectories in Fe_8

They showed oscillations of the tunnel splitting as a function of the magnetic field applied along the hard anisotropy axis and argued that they are due to topological quantum interference of two tunnel paths of opposite windings. They also showed that transitions between quantum numbers M = -S and (S - n), with n even or odd, revealed a parity effect that is analogous to the suppression of tunneling predicted for half-integer spins. This observation was a direct evidence of the topological part of the quantum spin phase (Berry phase) in a magnetic system see figure 2.9. There was a qualitative agreement with the theory of Garg and quantitative agreement is obtained when the fourth order anisotropy term is included in the Hamiltonian (see the bottom left figure in 2.9). Interference was observed for several resonances (k=0, 1, 2) as can be seen from the lower right figure in 2.9. It also shows that k = 1 resonance (odd

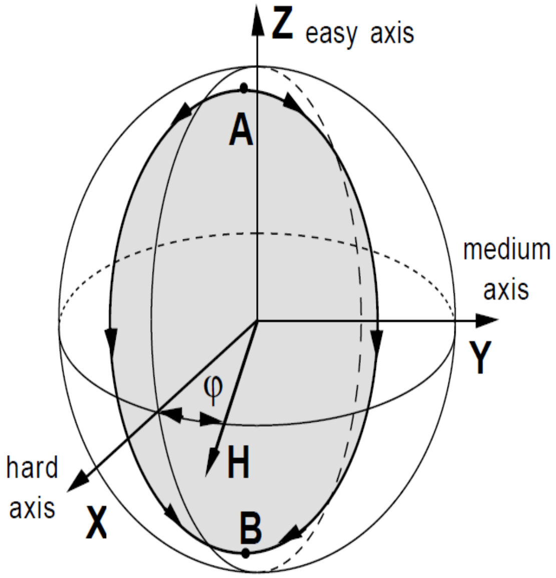

Figure 2.10: Unit sphere showing degenerate minima A and B which are joined by two tunnel paths (heavy lines). The hard, medium, and easy axes are taken in x, y and z direction, respectively. The transverse field is applied in the xy plane at an azimuth angle ϕ. At zero applied field, the giant spin reversal results from the interference of two quantum spin paths of opposite direction in the easy anisotropy plane yz [51].

resonance) is out of phase with the k = 0, 2 resonances (even resonances). This is called parity-effect. It results from the selection rule imposed by the second-order transverse anisotropy in Fe_8, in particular the fact that odd resonances are forbidden for an integer spin.

The fact that the tunnel splitting does not go to zero prompted the authors for a follow up work [53] where they made every possible effort to align the transverse field well in the direction of the hard axis. They then measured $\Delta(M_{in})$ (where M_{in} is the initial magnetization) and noticed a strong dependence of the minimal tunnel splitting on the initial magnetization which demonstrates the dipolar interaction between Fe_8 molecular clusters [53], see figure 2.11.

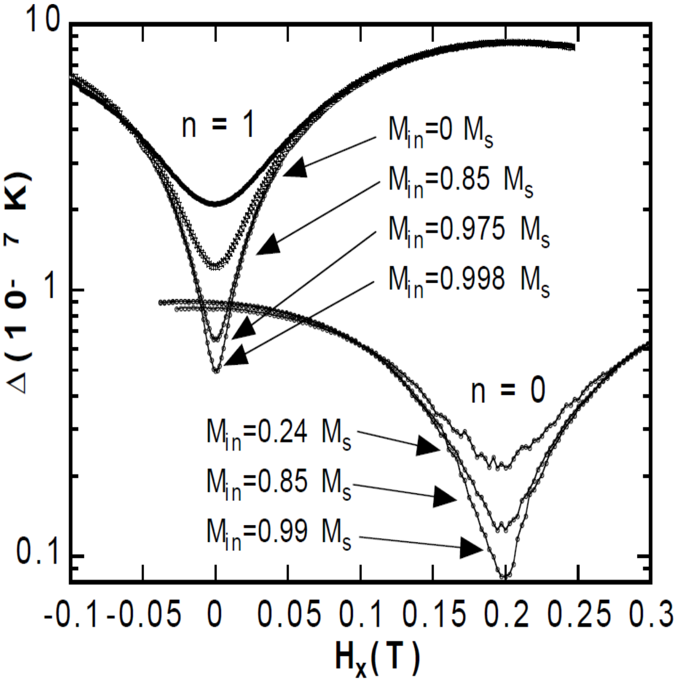

Figure 2.11: Detailed measurement of the tunnel splitting Δ around a topological quench for the quantum transition between $M = 10$ and $(10\ n)$ at $\phi = 0$ for Fe_8, [53].

We end this section by noting that more recently there has been renewed interest in geometric-phase interference effects in SMMs that behave as exchange-coupled dimers [54, 55], and in antiferromagnetic SMMs [56, 57].

2.4 Quantum Classical Crossover Between Thermally Assisted and Pure Quantum Tunneling in Molecular Magnets

As mentioned in earlier sections, molecular magnets exhibit bistability which made them an interesting system to investigate quantum tunneling. Transition between two states in such a system is temperature dependent. At high temperature, the transition follows the Arrhenius law, $\Gamma \approx exp(-\Delta U/T)$ with ΔU being the height of the energy barrier between the two states. At very low temperature, the transitions occur by quantum tunneling. Thus there exists a crossover temperature T_0 from the thermally activated regime to the pure quantum tunneling regime. For a quasiclassical particle in a potential U(x), Goldanskii [58] defined the temperature more accurately as $T_0^{(2)} = \hbar\tau_0$ where τ_0 is the period of small oscillations near the bottom of the inverted potential −U(x). Above $T_0^{(2)}$ quantum effects are negligible and transitions occur via the top of the barrier by thermal activation whereas below $T_0^{(2)}$, thermally assisted tunneling occurs from the excited states that reduces to the tunneling from the ground state at T=0. More extensive theoretical work of the crossover were done by Affleck [59], Larkin and Ovchinnikov [60] who showed that a second-order crossover from thermal to quantum regimes can occur at T_0 by using the standard instanton technique. Chudnovsky [61] demonstrated that the crossover can be first and second order depending on the potential. Later on Chudnovsky and Garanin [62] applied this to the problem of spin tunneling. The escape rate can change sharply for the case of first-order crossover or smoothly for the case of second-order crossover around the crossover temperature. They argued that both kinds of crossover can exist for Mn_{12}-Acetate depending on the strength of the transverse field [62, 63]. The dependence of the crossover temperature on the transverse field was calculated and was shown to be non-monotonic [62, 63].

There were no experimental evidence of the crossover in SMMs until 1999 when

Kent et al. [64, 65] presented experimental evidence for the crossover in Mn_{12}-acetate. They studied steps in the magnetization curves for various temperatures ranging from 0.4 K to 2.4 K. They found that, at lower temperature there is an abrupt shift in the step position and it could be attributed to transition from thermally assisted tunneling to pure quantum tunneling. They also showed that the transverse magnetic field makes the crossover more gradual (that is a second order cross-over) and leads to a continuous shift in the dominant energy levels with temperature, thus validating prior theoretical work [62, 63].

In the experiment of Kent et al. [64], the derivative of the magnetization as a function of the applied field was obtained for various temperatures see figure 2.12. The important features presented in the data of figure 2.12 are:
a. As the temperature is lowered, lower field peaks decrease in amplitude consistent with the model of thermally assisted tunneling.
b. As the temperature is lowered, peaks shift continuously to higher fields.
c. For temperatures below 1.2 K peaks in $\frac{dM}{dH}$ shift dramatically in position as a function of the temperature. For example the n = 7 peaks shifts from 3.10 T at 1.6 K to 3.53 T at 1 K, that is, it has shifted by a full quantum field H_0. All steps observed at low temperatures exhibit this type of shift.
The dependence of the peak positions on temperature is then plotted see figure 2.13.

One can note from figure 2.13 the following:
a. Initially, starting from 1.8 K, as the temperature if lowered the peaks shift to higher magnetic fields.
b. The solid vertical line shows demarcates the approximate temperature at which sudden shifts in peak positions occur.
c. Below the solid line, the step positions are independent of temperature except for the high indices line (n=9).

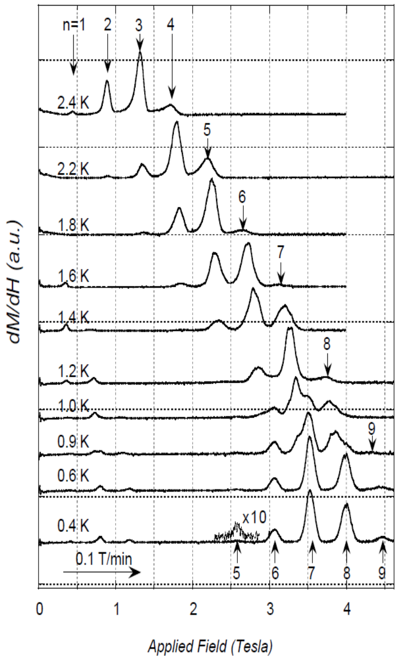

Figure 2.12: Derivative of the magnetization with respect to the applied field versus the field for various temperatures [64].

Based on the data presented in figure 2.13, one can distinguish between two different temperature regimes. At high temperature the step positions shift gradually with temperature, which is the regime of thermally assisted tunneling. The second regime is that of low temperature (below the solid line) in which the positions of peaks in the magnetization is independent of temperature. This is quantum tunneling from the lowest levels in the metastable well. The abrupt shift in step position with temperature can be the evidence for first-order transition between thermally assisted and pure quantum tunneling in line with the prediction of Chudnovsky and Garanin [62, 63]. The authors of [64, 65] followed up with data on the effect of the transverse field, and they found [65] that the crossover between the two regimes can be first-order or second-order depending on the magnitude and orientation of the applied field as

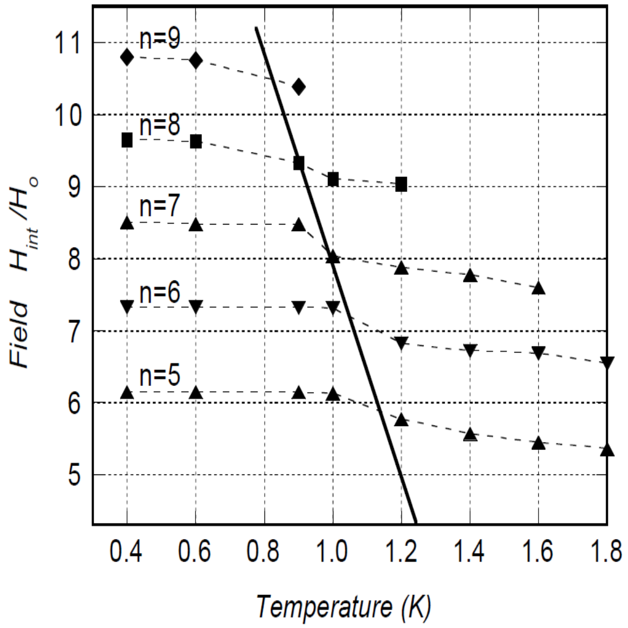

Figure 2.13: The dependence of the peak positions on temperature [64].

suggested by theory.

More recently, Wernsdorfer et al [66] explored sharp crossover between thermally assisted and pure quantum tunneling in Mn_{12}-*t*BuAc molecular magnet. Similar to Mn_{12}-acetate, it has spin S = 10 but the molecules are better isolated and the crystals have less disorder and a higher symmetry. They found a sharp crossover between thermally assisted and pure quantum tunneling.

Chapter 3

Magnetic Deflagration

In this chapter, we are going to discuss the first two experiments performed to study magnetic avalanches in Mn_{12}-acetate. We will then proceed to explore the theory that explained in detail the experimental results as well as its prediction for various parameters.

3.1 Nature of Magnetic Avalanches

We have seen in the previous chapter that the magnetization of a prototypical molecular magnet such as Mn_{12}-acetate exhibits a series of steps at low temperature due to quantum tunneling at certain values of the applied longitudinal magnetic field. It was first reported by Paulsen and Park [29] that Mn_{12}-acetate crystals sometimes exhibit a sudden, complete reversal of the magnetic moment during a field-swept experiment. Initially when early experiments were performed by Friedman et al. [24], sudden jumps in the magnetization were also occasionally observed and were an impediment to understand the nature of the steps in the magnetization see figure 3.1.

Those sudden jumps in the magnetization represent an abrupt reversal of the magnetic moment and are called avalanches. Later on in 2005, Suzuki et al. [67] investigated magnetic avalanches using local time-resolved measurements of the reversal of the magnetization. The sample was first magnetized in a certain direction

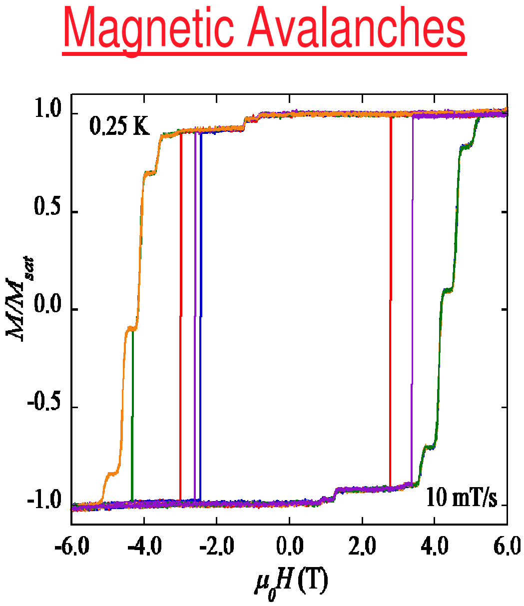

Figure 3.1: Magnetization curve for a Mn_{12}-acetate sample. Note the sudden jump in the magnetization in the red and purple curve.

(+ or −c-axis), the field was then swept in the opposite direction and avalanches ignited at a certain value of the field. The local magnetization was tracked using an array of micron-sized Hall sensors placed on the surface of Mn_{12}-acetate crystals see figure 3.2. They discovered [67] that a magnetic avalanche propagates through the crystal at speed of about 10 m/s in the form of a narrow interface between regions of opposite magnetization.

Chudnovsky suggested that the phenomenon was analogous to the propagation of a flame front through a flammable chemical substance. A crystal of Mn_{12} molecules placed in a magnetic field opposite to the magnetic moment is equivalent to a metastable chemical substance with the Zeeman energy ($\Delta E = 2g\mu_B HS$) playing the role of the chemical energy as illustrated in figure 3.3. A well-known mechanism for the release

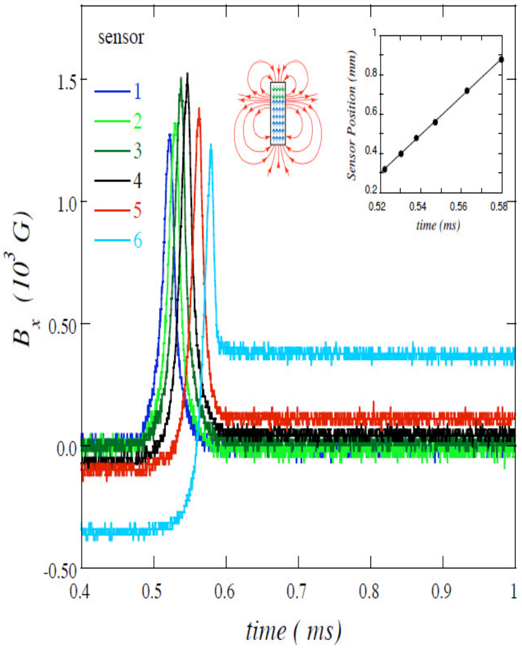

Figure 3.2: Signals recorded during a magnetic avalanche by Hall sensors placed on the surface near the middle of a bar-shaped sample of Mn_{12}-acetate. The schematic indicates the field line configuration that gives rise to the signals as the avalanche propagates from one end of the sample to the other. The inset shows sensor positions versus the time at which each sensor recorded the peak amplitude for an avalanche that started at the top and travels downward [68].

of energy by a metastable chemical substance is combustion, often referred to as deflagration [69]. From this mechanism, one can write the time of the chemical reaction τ as:

$$\tau(H) = \tau_0 \quad exp[\frac{U(H)}{k_B T_f}] \tag{3.1}$$

where $\tau_0 \approx 10^{-7}s$ is the attempt time [24] and T_f is the temperature of the flame. The dynamics of the flame are governed by heat diffusivity κ which obeys: $\frac{\partial T}{\partial t} = \kappa \nabla^2 T$ and the dependence of v, the velocity of the flame front, on H, the field, was found to be:

$$v \approx \frac{\delta}{\tau} \approx \sqrt{\kappa/\tau} = \sqrt{\frac{\kappa}{\tau_0}} exp[-\frac{U(H)}{2k_B T_f}] \tag{3.2}$$

where $\kappa \approx 10^{-5}m^2/s$ for the case of Mn_{12}-acetate. This approach to magnetic deflagration was explored in further detail by E. M. Chudnovsky and D. A. Garanin [70]. We will explore their theory in more details at the end of this chapter. The experimental values for the velocity of progapation of avalanches versus the applied field are shown in figure 3.4.

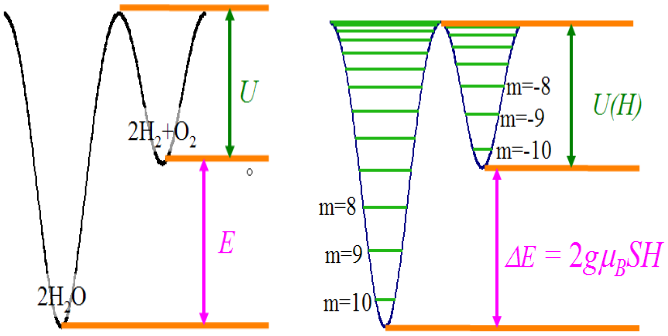

Chemical Reaction

Spin Reversal

Figure 3.3: A crystal of Mn_{12} molecules placed in a magnetic field opposite to the magnetic moment is equivalent to a metastable flammable chemical substance. In our case the role of the chemical energy stored in the molecule is played by the difference in the Zeeman energy $\Delta E = 2g\mu_B HS$.

The experiment of Suzuki was an important first step towards the understanding of avalanches. The process is similar to flame propagation through a metastable chemical substance and the analogy derives from the bistability of molecular magnets. In contrast to the destructive nature of chemical deflagration, magnetic deflagration is a non-destructive, reversible process. The only setback was the fact that the authors had no control over the value of the field at which avalanches were triggered. A more controlled ignition of avalanches was performed by Hernández-Mínguez et al. [71] as we'll discuss next. Finally, it is important to note that direct measurements of the heat emitted have confirmed the thermal nature of the avalanches: molecular crystals can also emit bursts of radiation during avalanche [72, 73, 74].

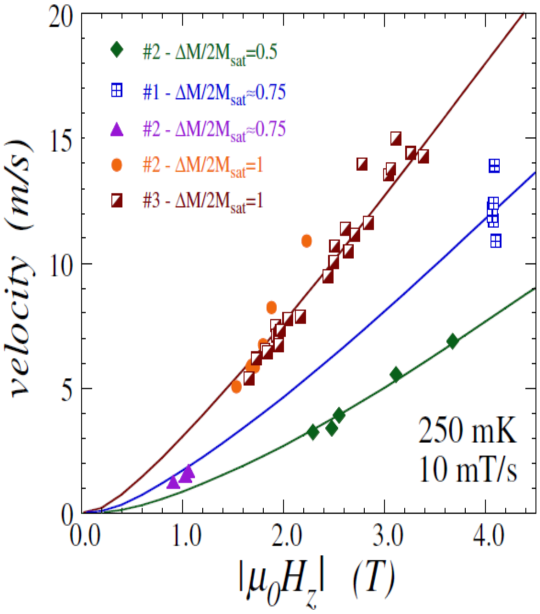

Figure 3.4: Velocity of propagation of avalanches versus the magnetic field at which the avalanches occurred for samples whose magnetization is prepared differently, when $\Delta M/2M_{sat} = 1$, we have a full change of the magnetization whereas for zero-field-cooled conditions $\Delta M/2M_{sat} = 0.5$ [67].

3.2 Quantum Features of Magnetic Avalanches

Hernández-Mínguez et al. [71] studied avalanches by igniting them using surface acoustic waves (SAW). A plot of the velocity as a function of the magnetic field showed peaks at certain values of the field unlike the previous results obtained by Suzuki et al.[67] see figure 3.4 in comparison with figure 3.5. The presence of those peaks indicated that deflagration in Mn_{12} acetate is assisted by quantum tunneling between spin states.

This has motivated lot of theoretical and computational work in the subject which

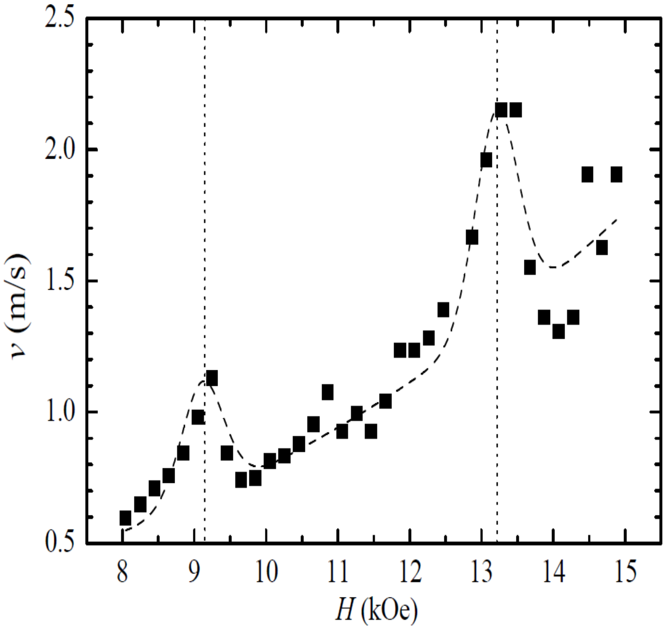

Figure 3.5: Velocity of propagation of avalanches versus the magnetic field. The vertical dashed line shows the position of the tunneling resonances [71].

we will explore in the next chapter and in Part III of this thesis. I end this section by noting that McHugh et al. [75] employed a resistive wire as a simple electric heater to trigger avalanches.

3.3 Theory of Magnetic Deflagration

Motivated by the experimental work mentioned in the previous two sections, Garanin and Chudnovsky [70] developed a comprehensive theory of magnetic deflagration. In their paper, they calculated the combination of parameters (magnetic field, initial temperature, and size of the sample) that sets off the deflagration process and the temperature of the flame and the velocity of the deflagration front. The most important aspect of the theory of the deflagration is the fact that energy is released by the metastable spins as they relax to the ground state and that this energy diffuses as heat through the crystal and thermally causes the reversal of neighboring spins in the metastable state.

So when a magnetic molecule makes a transition from the metastable state $S_z = -10$ to the absolute energy minimum $S_z = 10$, the energy ΔE is released. This leads to temperature change $\Delta T = \Delta E / C_{ph}$, where C_{ph} is the phonon heat capacity per magnetic molecule. The magnetic relaxation creates a source in the heat conduction equation. Another term added to this equation is due to heat flow $q = -k\nabla T$ so that the system of equations that describe the temperature T and the populations of the metastable minimum n_- has the form:

$$\frac{\partial T}{\partial t} = \frac{1}{C_{\mathrm{ph}}} \nabla . k \nabla T - \frac{\Delta \mathrm{E}}{C_{\mathrm{ph}}} \frac{\partial n_-}{\partial t} \tag{3.3}$$

$$\frac{\partial n_-}{\partial t} = -\Gamma \left(n_- - n_-^{\mathrm{eq}} \right) \tag{3.4}$$

where n_-^{eq} is given by

$$n_-^{\mathrm{eq}} = \frac{1}{exp(\frac{\Delta E}{K_B T}) + 1} \tag{3.5}$$

and Γ is given by an Arrhenius law

$$\Gamma = \Gamma_0 exp[\frac{-U}{K_B T}] \tag{3.6}$$

One important feature of magnetic deflagration is the strong temperature dependence of the heat capacity and thermal conductivity at low temperatures. The phonon heat capacity C_{ph} has the form:

$$C_{ph} = A k_B \left(\frac{T}{\Theta_D} \right)^{\alpha} \tag{3.7}$$

where $\alpha = 3$ in 3 D, A is a numerical factor and Θ_D is the Debye temperature. From the simple crystal model that assumes that at low temperatures only acoustic phonons are excited [76], $A = 12\pi^4/5$. The thermal diffusivity κ is given by

$$\kappa = K/C_{ph} \tag{3.8}$$

and depends on the average mean free path of thermal phonons. Since the heat capacity and thermal conductivity strongly depend on temperature, equations 3.3, 3.4 are coupled nonlinear differential equations.

Several aspects of deflagration were investigated. Below we summarize the most important findings.

1. Ignition time is defined as the time it takes the thermal runaway to develop and is denoted by τ_{ig}. If the rate of heat transfer out of the sample is very high, ignition does not occur. For an infinite and/or thermally insulated samples, the temperature of the sample is the only relevant variable and its dynamics are determined by the competition between the heat release due to relaxation (that is nonlinear in temperature) and the heat loss due to heat conduction (that is linear in temperature). Ignition threshold occurs when one changes various parameters (sample size, energy barrier, temperatures at the boundaries, initial magnetization) until the thermal runaway begins. Ignition is mainly controlled by the parameter δ given by:

$$\delta = \left(\frac{R}{l_0}\right)^2 = \frac{R^2 U \Delta E n_{-,i} \Gamma(T_0)}{2K_0 K_B T_0^2} \tag{3.9}$$

where R is a typical shortest distance from the center of the sample to its boundary and K_0 is thermal conductivity K at $T = T_0$. l_0 is the characteristic thermal length at $T = T_0$. The exact value of δ_c depends on the geometry of the sample. Various values of δ_c are given in [70] for various dimensions. In one dimension, δ_c=0.439.

2. Ignition threshold is also calculated in the presence of field gradient and in the presence of temperature gradient.

3. Solutions to equations 3.3 and 3.4 describe deflagration. Because of the dependence of the heat capacity and thermal conductivity on temperature, the authors switch to the phonon energy E as their dynamical variable instead of the temperature T, equations 3.3 and 3.4 become:

$$\frac{\partial \tilde{E}}{\partial \tau} = \tilde{\nabla} \cdot \tilde{\kappa} \tilde{\nabla} \tilde{E} - \frac{\partial \tilde{n}}{\partial \tau} \tag{3.10}$$

and

$$\frac{\partial \tilde{n}}{\partial \tau} = -\tilde{\Gamma}(\tilde{E})\tilde{n} \tag{3.11}$$

where $\tilde{E}, \tau$ and $\tilde{\Gamma}$ are given by:

$$\tilde{E} = \frac{E}{n_{-,i}\Delta E} \quad \tau = t\Gamma_f \tag{3.12}$$

where κ_f and Γ_f are thermal diffusivity and relaxation rate at the flame temperature T_F and $l_d = \sqrt{\kappa_f/\Gamma_f}$ describes the width of the deflagration front. $\tilde{\Gamma}(\tilde{E})$ is given by

$$\tilde{\Gamma}(\tilde{E}) = \frac{\Gamma}{\Gamma_f} = exp[W_f(1 - \frac{1}{\tilde{T}(\tilde{E})})] \tag{3.13}$$

where $\tilde{\kappa} = \kappa/\kappa_f$ and $\tilde{T} = T/T_f$.

4. The real deflagration speed is given by

$$v = \tilde{v} l_d \Gamma_f = \tilde{v}\sqrt{\kappa_f \Gamma_f} = \tilde{v}\sqrt{\kappa_f \Gamma_0} exp(-W_f/2) \tag{3.14}$$

if $\tilde{v} = \frac{1}{\sqrt{v_f}}$ where $v_f = \frac{W_f}{\alpha+1}$ then v becomes:

$$v = \sqrt{\frac{\kappa_f \Gamma_0}{v_f}} exp(-W_f/2) \tag{3.15}$$

The flame Arrhenius exponent W_f is given by:

$$W_f = \frac{U}{K_B T_f} \tag{3.16}$$

5. From the theory of magnetic deflagration, avalanches can be ignited by either increasing the magnetic field or temperature. The simplest situation is when the magnetic field and temperature of the sample boundary T_0 are independent of coordinates. In this case, the crystal loses stability against formation and propagation of the flame when the rate of the spin flip for an individual molecule, $\Gamma(H, T_0)$ exceeds:

$$\Gamma_c = \frac{8K(T_0)K_B T_0^2}{U(H)\Delta E(H) n_{-,i} l^2} \tag{3.17}$$

$n_{-,i}$ can be expressed as $n_{-,i} = \frac{M_0 - M_i}{2M_0}$. T_0 is field dependent and the dips in $T_0(H)$ at regularly spaced fields are due to the maxima of $\Gamma(H, T_0)$ at tunneling resonances see figure 3.6 as found experimentally by Hernández-Mínguez et al [73].

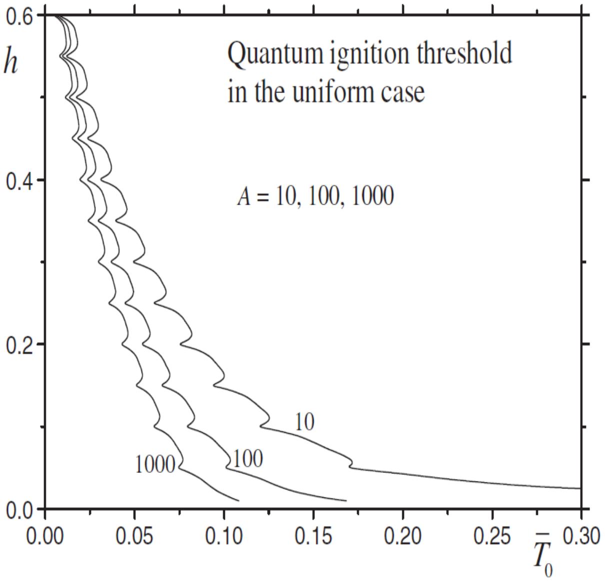

Figure 3.6: The dependence of the magnetic field that ignites deflagration on the temperature of the crystal of Mn_{12}. A is given by $A = \frac{R^2\Gamma_0 n_{-,i}}{2\kappa(T_0)/k_B}$ [70].

6. The study has elucidated the fact that magnetic avalanches start as an instability of a smooth temperature profile when the spin-flip rate of individual molecules exceeds the rate at which the heat flows out of the burning region.The effect is exponentially sensitive to the magnetic field and temperature of the sample.

7. The speed of the developed deflagration front is:

$$v(H) = \sqrt{\frac{4K_B T_f \kappa(T_f)\Gamma(H, T_f)}{U(H)}} \tag{3.18}$$

where κ is the thermal diffusivity and

$$T_f = \frac{\Theta_D}{\pi}[\frac{5n_{-,i}\Delta E(H)}{3K_B\Theta_D}]^{1/4} \tag{3.19}$$

is the flame temperature.

This theory was a very important first step towards understanding the nature of magnetic avalanches. It will be extensively used in Part III when we develop a numerical framework to study front of spin tunneling in molecular magnets where the relaxation rates will be determined without using Arrhenius exponent.

Part II

Quantum Magnetomechanical Effects

Introduction

In this part, we present our work on magneto-mechanical effects. In the first work, we devised a microscopic theory to describe the Einstein-de Haas effect in a microcantilever. This theory has been motivated by an experiment performed at NIST in 2006 in which the mechanical modes of the cantilever have been coupled to the frequency of the ac field and the maximal displacement of the cantilever at the free end was measured to be 3 nm. In the second work, we studied resonant coupling between the mechanical modes of the cantilever and the frequency of spin tunneling in a molecular magnet deposited on a nanocantilever. Finally, in the third project, we studied the spin-rotation effects in a magnetic molecule bridged between two conducting leads.

Chapter 4

Einstein-de Haas Effect at the Nanoscale

In this chapter, we start by describing the NIST experiment on the Einstein-de Haas Effect in a NiFe Film Deposited on a Microcantilver, we then present the theory that we came up with to describe the experimental results.

4.1 Einstein-de Haas Effect in a NiFe Film Deposited on a Microcantilver

4.1.1 What is the Einstein-de Haas Effect?

Einstein - de Haas effect [77] consists of the mechanical rotation of a freely suspended body, caused by the change of its magnetic moment. The latter can be induced by the applied magnetic field or by rapid warming. The Einstein - de Haas effect is a direct consequence of the conservation of the total angular momentum (spin + orbital). Consider, e.g., a solid made of N atoms of magnetic moment $\mathbf{M} = \gamma_J \mathbf{J}$, where $\mathbf{J} = \mathbf{S} + \mathbf{L}$ is the operator of the total angular momentum of the atom (that includes spin $\mathbf{S}$ and orbital moment $\mathbf{L}$), $\gamma_J = g_J e/(2mc)$ is the gyromagnetic ratio for J, $e < 0$

is the charge of electron, and $g_J = 1 + [2J(J+1)]^{-1}[J(J+1) + S(S+1) - L(L+1)]$ is the Lande factor. Total angular momentum of the magnet suspended from a string is a sum of $N\langle \mathbf{J} \rangle$ and the mechanical orbital moment, $\boldsymbol{\mathcal{L}}$, due to the rotation of the solid. If, for example, the solid, initially non-magnetized and at rest, develops a macroscopic magnetic moment $\boldsymbol{\mathcal{M}} = N\langle \mathbf{M} \rangle = \gamma_J N\langle \mathbf{J} \rangle$, then the conservation law requires that $N\langle \mathbf{J} \rangle + \boldsymbol{\mathcal{L}} = 0$. This gives $\boldsymbol{\mathcal{L}} = -\boldsymbol{\mathcal{M}}/\gamma_J$, that is, the solid begins to rotate on being magnetized.

Experiments on Einstein - de Haas effect and the related Barnett effect [78] (generation of the magnetic moment by mechanical rotation, see figure 4.1), performed at the dawn of quantum physics, provided first measurements of the gyromagnetic ratio for various materials [79]. Even today the Einstein - de Haas method can still provide

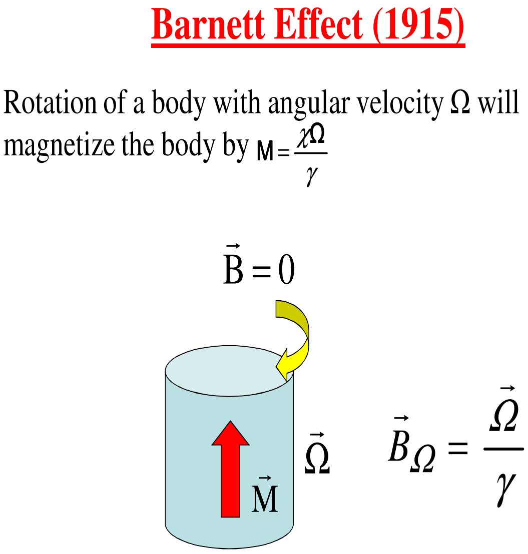

Barnett Effect (1915)

Rotation of a body with angular velocity Ω will magnetize the body by $M = \frac{\chi\Omega}{\gamma}$

Figure 4.1: The Barnett Effect.

a more accurate value of g_J as compared to electron spin resonance and ferromagnetic resonance methods that require precise knowledge of the effective magnetic field inside the sample [80]. Nevertheless fundamental questions about the Einstein - de Haas effect remain unanswered. In particular, the global conservation of the angular momentum does not explain how the angular momentum is actually transferred from individual atoms to the whole body. This question is clearly related to the magnetic relaxation and decoherence at the atomic level. The latter determine the width of para- and ferromagnetic resonances, as well as functionality of spin-based qubits. Advances in manufacturing and measuring of nanomechanical devices promise to revive interest to the local dynamics of Einstein - de Haas effect.

4.1.2 NIST Experiment

In 2006, an experiment was performed at the National Institute of Standards and Technology (NIST) laboratory in Boulder, Colorado [82]. In that experiment, a 50nm permalloy film was deposited onto a 200μm×20μm×0.6μm cantilever. The cantilever was placed inside a coil that generated an ac magnetic field. Oscillation of the cantilever was measured by a fiber optic interferometer positioned above the tip of the cantilever. When the frequency of the ac field matched the resonance frequency of the cantilever the amplitude of the oscillations was about 3nm. The data were analyzed within a model that replaced the mechanical torque due to change in the magnetization by the effect of the periodic force acting on the fictitious point mass at the free end of the cantilever. The amplitude z_0 of the cantilever deflection was calculated using

$$z_0 = \frac{F_0/m_{mod}\omega}{\sqrt{\left(\omega_0^2 - \omega^2\right)^2\omega^2 + \omega_0^2/Q^2}} \tag{4.1}$$

where

$$F_0 = \frac{4m_e\Delta\mu\omega}{l_c e g'} \tag{4.2}$$

ω is the driving frequency of the alternating magnetic field, $\Delta\mu$ is the change in the magnetic moment of the film, m_{mod} is the modal mass of the beam, $\omega_0 = 2\pi f_0$

is the resonant frequency of the beam, Q is the quality factor, and l_c is the length of the cantilever and $g' = \frac{2m_e\mu}{eJ_{tot}}$ is the magnetomechanical ratio with m_e being the mass of the electron, μ the magnetic moment, and J_{tot} the total angular momentum. In order to determine the value of g', the authors determined the deflection of the cantilever as a function of the frequency of the magnetic field. The results are plotted in 4.2; It is important to note that $\Delta\mu$ was already determined from magnetometry measurements. The authors fitted the data in 4.2 giving $f_0 = 13180$ Hz, $Q = 24$, and $g' = 1.82$. Another confirmation of the value of g' is obtained by plotting $\frac{zl_c em_{mod}\omega_0}{4m_eQ}$ versus $\Delta\mu$ which gives a straight line whose slope is $1/g'$. The value of g' obtained in that case is 1.83 ± 0.10. In Bulk permalloy, g' is 1.91. Although this experiment provided evidence of the Einstein-de Haas effect at the microscale, the explanation

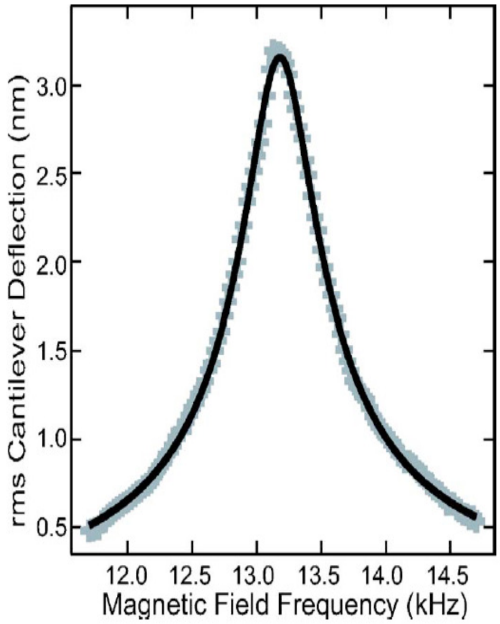

Figure 4.2: Root mean square (rms) cantilever deflection [82].

presented in equation 4.1 is insufficient for the study of the microscopic dynamics of the Einstein - de Haas effect. This motivated me to study the dynamics of the Einstein-de Haas effect which will be the subject of the next two sections [81].

4.2 Spin Rotation Interaction

4.2.1 Introduction

In order to develop the theoretical framework to describe the Einstein - de Haas effect, we shall assume (as is the case for many magnetic solids) that the magnetism is of spin origin and can be described either by individual spins, $\mathbf{S}_i$, localized at the atomic sites i, or by a continuous spin field $\mathbf{S}(\mathbf{r}, t)$. (Generalization to magnetism of spin and/or orbital origin can be obtained through a straightforward re-definition of the constants). We shall derive general equations describing the transfer of the spin angular momentum to the mechanical angular momentum of the body. In the NIST experiment, the effect of the ac magnetic field was likely the displacement of the domain wall separating two magnetic domains inside the permalloy film. We shall pay special attention to this case. The cantilever problem will be solved by adding the internal torque due to the motion of the domain wall to the equations of the elastic theory describing the motion of the cantilever. The obtained dynamics of the cantilever is rather rich and it allows a detailed comparison between theory and experiment.

4.2.2 Microscopic Theory of Spin-Rotation Coupling

Spin-lattice interaction comes from magnetostriction and spin-rotation coupling. Only the latter, however, is responsible for the Einstein - de Haas effect. The most obvious effect of local elastic twists comes from the dependence of the energy of a spin on its orientation in the crystal - magnetic anisotropy. This effect is due to spin-orbit interactions and is of relativistic origin. It is described by the crystal-field Hamiltonian that can be very generally written as

$$\hat{H}_A = \sum_j K_j^{\alpha\beta} S_j^\alpha S_j^\beta + \sum_j L_j^{\alpha\beta\gamma\delta} S_j^\alpha S_j^\beta S_j^\gamma S_j^\delta + ..., . \tag{4.3}$$

Here the Greek letters denote Cartesian components of a dimensionless spin vector $\mathbf{S}_j$ belonging to the site j of the crystal lattice. Tensors $K_j^{\alpha\beta}$, $L_j^{\alpha\beta\gamma\delta}$, etc., describing magnetic anisotropy, are defined in the coordinate frame $\mathbf{e}_j^{(1,2,3)}$ that is rigidly coupled to the locally-defined crystal axes, see Fig.4.3.

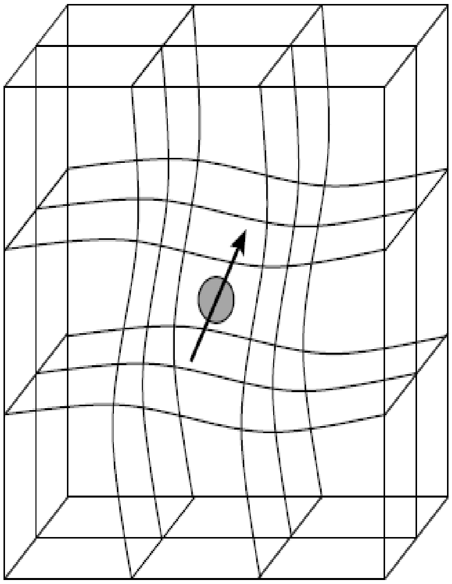

Figure 4.3: Rotation of the crystal field due to local elastic twist at the location of the spin.

Local rotation of the lattice is performed by the (3×3) rotation matrix $\mathbb{R}_j$,

$$\mathbf{e}_j^{(1,2,3)} \to \mathbb{R}_j \mathbf{e}_j^{(1,2,3)} . \tag{4.4}$$

It results in

$$\begin{aligned}
&K_j^{\alpha\beta} \to \mathbb{R}_j^{\alpha\gamma}\mathbb{R}_j^{\beta\delta}K_j^{\gamma\delta} \\
&L_j^{\alpha\beta\gamma\delta} \to \mathbb{R}_j^{\alpha\eta}\mathbb{R}_j^{\beta\xi}\mathbb{R}_j^{\gamma\theta}\mathbb{R}_j^{\delta\epsilon}L_j^{\eta\xi\theta\epsilon} \\
&...
\end{aligned} \tag{4.5}$$

For a small rotation at the site j by an angle $\delta\phi_j$, one has

$$\mathbb{R}_j^{\alpha\beta} = \delta^{\alpha\beta} - \epsilon^{\alpha\beta\gamma}\delta\phi_j^{\gamma}. \tag{4.6}$$

We now notice that due to the rotational invariance of $\hat{H}_A$, the rotation of the local frame $(\mathbf{e}_j^{(1)}, \mathbf{e}_j^{(2)}, \mathbf{e}_j^{(3)})$ is equivalent to the rotation of the vector $\mathbf{S}_j$ by the same angle in the opposite direction, $\mathbf{S} \to \mathbb{R}^{-1}\mathbf{S}$. As is known [83], this rotation can be equivalently performed by the $(2S+1) \times (2S+1)$ matrix in the spin space,

$$\mathbf{S}_j \to \hat{R}_j\mathbf{S}_j\hat{R}_j^{-1}\,, \qquad \hat{R}_j = e^{-i\mathbf{S}_j\cdot\delta\phi_j}\,. \tag{4.7}$$

Consequently, in the presence of rotations, $\hat{H}_A$ becomes [84, 94]

$$\hat{H}'_A = \hat{R}\hat{H}_A\hat{R}^{-1},, \tag{4.8}$$

where

$$\hat{R} = e^{-i\sum_j \mathbf{S}_j\cdot\delta\boldsymbol{\phi}_j},. \tag{4.9}$$

In the linear order on $\delta\boldsymbol{\phi}_j$ one obtains

$$\hat{R}\hat{H}_A\hat{R}^{-1}\cong\hat{H}_A+\hat{H}_R, \qquad \hat{H}_R = i\sum_j\left[\hat{H}_A, \mathbf{S}_j\right]\cdot\delta\boldsymbol{\phi}_j,. \tag{4.10}$$

By quantizing $\delta\boldsymbol{\phi}_j$ one can apply this Hamiltonian to the study of rigid spin clusters and quantum dots [86, 87, 88].

The total spin Hamiltonian $\hat{H}_S$ may include exchange interaction, magnetostriction, Zeeman interaction and dipole-dipole interaction. The dipole-dipole interaction is usually the weakest one and will not be considered here. The magnetostriction is local on spin. Consequently, it is transformed by rotations the same way as the crystal field. The Zeeman interaction of spins with the external magnetic field $\mathbf{B}$,

$$\hat{H}_Z = \sum_j \mathbf{b} \cdot \mathbf{S}_j, \qquad \mathbf{b} \equiv g\mu_B \mathbf{B} \tag{4.11}$$

is not affected by rotations; g being the gyromagnetic factor for the spin. Here we take into account that the magnetic moment due to spin, $\mathbf{M} = -g\mu_B\mathbf{S}$, has direction opposite to $\mathbf{S}$ because of the negative gyromagnetic ratio for the electron. Finally, the exchange interaction,

$$\hat{H}_{\text{ex}} = -\frac{1}{2}\sum_{ij} I_{ij}, \mathbf{S}_i \cdot \mathbf{S}_j, , \tag{4.12}$$

only depends on the local arrangement of spins that is not affected by rotations. In the first order on $\delta\boldsymbol{\phi}_j$, the generalization of Eq. (4.10) is

$$\hat{H}_R = i\sum_j \left[\hat{H}_S, \mathbf{S}_j\right] \cdot \delta\boldsymbol{\phi}_j - i\sum_j \left[(\hat{H}_Z + \hat{H}_{\text{ex}}), \mathbf{S}_j\right] \cdot \delta\boldsymbol{\phi}_j \,. \tag{4.13}$$

The last two terms appeared in Eq. (4.13) because Zeeman Hamiltonian (4.11) and the exchange Hamiltonian (4.12), that are included in $\hat{H}_S$, are independent from local rotations. Consequently, one should subtract $\hat{H}_Z$ and $\hat{H}_{\text{ex}}$ from $\hat{H}_S$ when computing the effect of rotations.

Let the total Hamiltonian of the system that incorporates all couplings, including interactions with rotations, be $\hat{H}$. It is clear that the difference between $[\hat{H}_S, \mathbf{S}_j]$ and $[\hat{H}, \mathbf{S}_j]$ begins with the terms that are linear on $\delta\boldsymbol{\phi}_j$. Thus, in the linear approximation on $\delta\boldsymbol{\phi}_j$, we can replace $i[\hat{H}_S, \mathbf{S}_j]$ in Eq. (4.13) with $i[\hat{H}, \mathbf{S}_j] = \hbar\dot{\mathbf{S}}_j$. Working out the commutator with the Zeeman Hamiltonian in Eq. (4.13) one obtains

$$\hat{H}_R = \sum_j \left(\hbar\dot{\mathbf{S}}_j + \mathbf{S}_j \times \mathbf{b} - i\sum_j \left[\hat{H}_{\text{ex}}, \mathbf{S}_j\right]\right) \cdot \delta\boldsymbol{\phi}_j \,. \tag{4.14}$$

4.3 Theory of a Magnetic Microcantilever

4.3.1 Elastic Theory With Internal Twists due to Spin-Rotation Coupling

Our approach to Einstein - de Haas effect is based upon Eq. (4.14). To apply this equation to long-wave torsional deformations of the body we shall write $\delta\boldsymbol{\phi}_j$ in terms of the displacement field of the elastic theory $\mathbf{u}(\mathbf{r},t)$ [95],

$$\delta\phi(\mathbf{r}) = \frac{1}{2}\nabla \times \mathbf{u}(\mathbf{r})\,, \tag{4.15}$$

and replace $\mathbf{S}_j$ by the spin density $\mathbf{S}(\mathbf{r},t)$. The classical energy of the body then becomes

$$\mathcal{H} = \mathcal{H}_S + \mathcal{H}_E + \mathcal{H}_R\,. \tag{4.16}$$

Here $\mathcal{H}_E$ is the elastic energy of the body written in terms of $\mathbf{u}(\mathbf{r},t)$ while $\mathcal{H}_S = \langle H_S \rangle$ includes exchange, anisotropy, Zeeman and dipolar energies, magnetostriction, etc., written in terms of $\mathbf{S}(\mathbf{r},t)$ and $\mathbf{u}(\mathbf{r},t)$ [10]. The last term in Eq. (4.16) follows from equations (4.14) and (4.15),

$$\mathcal{H}_R = \frac{1}{2}\int d^3r\,\left[\hbar\dot{\mathbf{S}} + \mathbf{S}\times(\mathbf{b}+\mathbf{b}_{\rm ex})\right]\cdot(\nabla\times\mathbf{u})\,, \tag{4.17}$$

where [2]

$$\mathbf{b}_{\rm ex} = \frac{\delta\mathcal{H}_{\rm ex}}{\delta\mathbf{S}} = -I_{\alpha\beta}\frac{\partial^2\mathbf{S}}{\partial r_\alpha \partial r_\beta} \tag{4.18}$$

and

$$I_{\alpha\beta} = \frac{1}{2}\sum_j I_{ij}(r_i^\alpha - r_j^\alpha)(r_i^\beta - r_j^\beta)\,. \tag{4.19}$$

The dynamical equation for the displacement field is [95]

$$\rho\frac{\partial^2 u_\alpha}{\partial t^2} = \frac{\partial\sigma_{\alpha\beta}}{\partial x_\beta}\,, \tag{4.20}$$

where $\sigma_{\alpha\beta} = \delta\mathcal{H}/\delta e_{\alpha\beta}$ is the stress tensor, $e_{\alpha\beta} = \partial u_\alpha/\partial x_\beta$ is the strain tensor, and ρ is the mass density of the material. The stress tensor can be divided into two parts,

$\sigma_{\alpha\beta} = \sigma^{(\mathrm{M})}_{\alpha\beta} + \sigma^{(\mathrm{R})}_{\alpha\beta}$, with

$$\sigma^{(\mathrm{M})}_{\alpha\beta} = \frac{\delta(\mathcal{H}_S + \mathcal{H}_E)}{\delta e_{\alpha\beta}} \tag{4.21}$$

and

$$\sigma^{(\mathrm{R})}_{\alpha\beta} = \frac{\delta \mathcal{H}_R}{\delta e_{\alpha\beta}} \,. \tag{4.22}$$

Here $\sigma^{(\mathrm{M})}_{\alpha\beta}$ is the mechanical part of the stress tensor, e.g., the part coming from the elastic properties of the cantilever plus magnetostriction, while $\sigma^{(\mathrm{R})}_{\alpha\beta}$ is the part of the stress tensor produced by the internal rotations due to spins,

$$\sigma^{(\mathrm{R})}_{\alpha\beta} = -\frac{1}{2}\epsilon_{\alpha\beta\gamma}\left\{\hbar\dot{S}_\gamma + [\mathbf{S}\times(\mathbf{b}+\mathbf{b}_{\mathrm{ex}})]_\gamma\right\} \,. \tag{4.23}$$

Notice that, contrary to the symmetric stress tensor ($\sigma_{\alpha\beta} = \sigma_{\beta\alpha}$) used by the conventional elastic theory, $\sigma^{(\mathrm{R})}_{\alpha\beta}$ is antisymmetric. The immediate consequence of that is a non-zero torque,

$$dK^{(\mathrm{R})}_{\alpha\beta} = (\sigma_{\alpha\beta} - \sigma_{\beta\alpha})d^3r \,, \tag{4.24}$$

acting on the volume element d^3r. Such torques, neglected by the conventional theory of elasticity, are responsible for the Einstein - de Haas effect.

Equations (4.20) - (4.23) allow one to obtain the general dynamical equation of the elastic theory that accounts for local internal forces due to the dynamics of spins in a ferromagnet:

$$\rho\frac{\partial^2 u_\alpha}{\partial t^2} - \frac{\partial \sigma^{(\mathrm{M})}_{\alpha\beta}}{\partial x_\beta} = f^{(\mathrm{R})}_\alpha \,, \tag{4.25}$$

where

$$\mathbf{f}^{(\mathrm{R})} = -\frac{1}{2}\boldsymbol{\nabla}\times\left[\hbar\dot{\mathbf{S}} + \mathbf{S}\times(\mathbf{b}+\mathbf{b}_{\mathrm{ex}})\right] \,. \tag{4.26}$$

Let us check that these equations conserve the total angular momentum (spin + orbital). Writing the total angular momentum due to the spins and the crystal as

$$\mathbf{J} = \int d^3r \left[\hbar\mathbf{S} + \rho\,(\mathbf{r}\times\dot{\mathbf{u}})\right] \,, \tag{4.27}$$

one obtains the following equation for the time derivative of the α-th component of $\mathbf{J}$,

$$\begin{aligned}
\dot{J}_\alpha &= \int d^3r \left[\hbar \dot{S}_\alpha + \epsilon_{\alpha\beta\gamma} r_\beta \left(\rho \ddot{u}_\gamma\right)\right] \\
&= \int d^3r \left\{\hbar \dot{S}_\alpha + \epsilon_{\alpha\beta\gamma} r_\beta \nabla_\delta \sigma^{(\mathrm{M})}_{\gamma\delta}\right. \\
&- \frac{1}{2}\left[r_\beta \nabla_\alpha - (\mathbf{r}\cdot\boldsymbol{\nabla})\,\delta_{\alpha\beta}\right] \times \\
&\left.\left[\hbar \dot{S}_\beta + (\mathbf{S}\times\mathbf{b})_\beta - \epsilon_{\beta\gamma\delta} I_{\epsilon\eta} S_\gamma \nabla_\epsilon \nabla_\eta S_\delta\right]\right\}, \qquad (4.28)
\end{aligned}$$

where we have used equations (4.25), (4.26) and (4.18). If one prohibits transfer of spin angular momentum through the surface, integration by parts with account of the symmetry of $\sigma^{(\mathrm{M})}_{\alpha\beta}$ and $I_{\alpha\beta}$ gives

$$\dot{\mathbf{J}} = \mathbf{K}^{(M)} + \mathbf{K}^{(R)}\,, \qquad (4.29)$$

with

$$K^{(M)}_\alpha = \int dA_\delta \left[\epsilon_{\alpha\beta\gamma} r_\beta \sigma^{(M)}_{\gamma\delta}\right] \qquad (4.30)$$

and

$$\mathbf{K}^{(R)} = \int d^3r\,(\mathbf{b}\times\mathbf{S})\ . \qquad (4.31)$$

Here $\mathbf{K}^{(M)}$ is the external mechanical torque applied to the surface of the body $\mathbf{A}$, while $\mathbf{K}^{(R)}$ is the volume spin torque due to the external magnetic field. Thus, in accordance with our expectation, when external forces are absent, Eq. (4.25) conserves the total angular momentum, $\dot{\mathbf{J}} = 0$.

If the spin-lattice interaction were absent there would be no deformation induced by the dynamics of spins. This condition provides another check of the validity of equations (4.25) and (4.26). In the absence of dissipation the spin field satisfies [2]

$$\hbar\dot{\mathbf{S}} = -\mathbf{S}\times\mathbf{b}_{\mathrm{eff}} \qquad (4.32)$$

where $\mathbf{b}_{\mathrm{eff}} = \delta\mathcal{H}/\delta\mathbf{S}$ is the effective field that can be presented as $\mathbf{b}_{\mathrm{eff}} = \mathbf{b} + \mathbf{b}_{\mathrm{ex}} + \mathbf{b}'$. Here $\mathbf{b}'$ is determined by the spin-lattice coupling. Its main part is usually the anisotropy field, $\mathbf{b}_A = \delta\mathcal{H}_A/\delta\mathbf{S}$. Equations (4.25) and (4.32) then show that Zeeman and exchange interactions alone do not provide any force on the body. This is in accordance with the fact that spins should couple to the lattice in order to produce such a force. Dissipation can be incorporated into the problem by adding standard damping terms to the elastic equation (4.25) and Landau-Lifshitz equation (4.32).

4.3.2 Dynamics of Magnetic Cantilever

Among many problems involving internal forces due to spins, Eq. (4.25) can be used for computation of the elastic motion of a magnetic cantilever. For example, in the case of the motion of a domain wall inside the cantilever, one substitutes the known domain wall solution for $\mathbf{S}(\mathbf{r}, t)$ into the right-hand side of Eq. (4.25), while the left-hand side follows from the elastic theory of cantilever in the absence of spins [95]. Sudden increase of the external magnetic field should result in the domain wall sweeping the cantilever, thus providing a source of deformation during a finite time. Application of a harmonic ac magnetic field, as in the NIST experiment, should lead to the oscillation of the position of the domain wall inside the cantilever. The geometry of the problem is shown in Fig. 4.4.

The cantilever of length L, parallel to the Y-direction, is magnetized in the X-direction. The $y = 0$ end of the cantilever is attached to the holder while the $y = L$ end is free. We are interested in small displacements of the cantilever in the Z-direction, $u_z(y, t)$, caused by the time-dependent external magnetic field. Vectors $\mathbf{B}$ and $\mathbf{S}$ are assumed to lie in the XY plane. The latter property of the magnetization is common for thin films. It is easy to see that in this case the terms proportional to $\mathbf{S} \times \mathbf{b}$ and $\mathbf{S} \times \mathbf{b}_{ex}$ in the right-hand side of Eq. (4.25) give zero contribution to the Z-component of the elastic equation. Adding the term proportional to $\dot{\mathbf{S}}$ to the right-hand side of the conventional equation of motion for a cantilever [95], one obtains from Eq. (4.25)

$$\rho\frac{\partial^2 u_z}{\partial t^2} + \frac{h^2 E}{12(1-\sigma^2)}\frac{\partial^4 u_z}{\partial y^4} = \frac{\hbar}{2}\frac{\partial}{\partial y}\frac{\partial}{\partial t}S_x(y, t)\,, \tag{4.33}$$

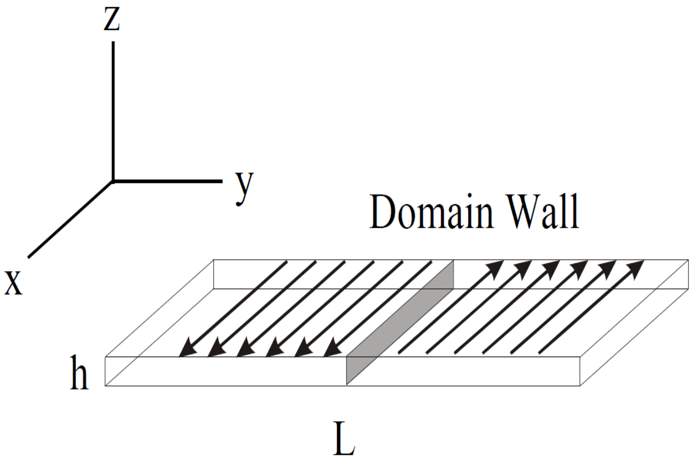

Figure 4.4: The geometry considered.

where h is the thickness of the cantilever in the Z-direction, E is the Young's modulus, and σ is the Poisson coefficient, $-1 < \sigma < 1/2$.

If the magnetization of the cantilever was rotating uniformly in space, then according to Eq. (4.33) the force from spins would only act on the free end of the cantilever where the magnetization has a discontinuity. However, for a soft magnetic material like permalloy, deposited on a cantilever that is large compared to the dimensions of a monodomain particle, the change in the magnetization should occur through the motion of a domain wall. For that reason we shall describe the magnetic state of the cantilever by two domains separated by the domain wall at $y = y_0(t)$. Then $S_x(y,t)$ is given by the domain wall solution centered at $y = y_0(t)$,

$$S_x(y,t) = S_{\mathrm{dw}}\left[y - y_0(t)\right] . \tag{4.34}$$

In the absence of the dc magnetic field this gives

$$\rho\frac{\partial^2 u_z}{\partial t^2}+\frac{h^2 E}{12(1-\sigma^2)}\frac{\partial^4 u_z}{\partial y^4}=$$
$$-\frac{\hbar}{2}\left(\frac{dy_0}{dt}\right)\frac{\partial^2}{\partial y^2}S_{\rm dw}\left[y-y_0(t)\right]\,. \tag{4.35}$$

For the dissipative motion of the domain wall the speed of the wall is proportional to the field. When the ac magnetic field, $B=B_0\cos(\omega t)$, is applied in the X-direction, one has $y_0(t)=y_0(0)+a\sin(\omega t)$, where $a<L$ is the amplitude of the oscillations around $y_0(0)$. The domain wall is given by $S_{\rm dw}(y,t)=S_0F\left[y-y_0(t)\right]$ where S_0 is a constant spin density and F changes from -1 to $+1$ as one crosses the wall. Note the connection of S_0 to the magnetization, $M_0=g\mu_B S_0$.

It is convenient to switch to dimensionless variables,

$$\bar{u}_z=\frac{u_z}{L}\,,\quad \bar{y}=\frac{y}{L}\,,\quad \bar{t}=t\nu\,,\quad \nu\equiv\sqrt{\frac{Eh^2}{12\rho(1-\sigma^2)L^4}}\,, \tag{4.36}$$

where L is the length of the cantilever and ν determines the scale of the eigenfrequencies of its vertical oscillations, $u_z(y,t)$. In terms of these variables Eq. (4.35) becomes

$$\frac{\partial^2\bar{u}_z}{\partial\bar{t}^2}+\frac{\partial^4\bar{u}_z}{\partial\bar{y}^4}=-\epsilon\left(\frac{d\bar{y}_0}{d\bar{t}}\right)\frac{\partial^2 F}{\partial\bar{y}^2}\,, \tag{4.37}$$

where

$$\epsilon=\frac{\hbar S_0}{2\rho L^2\nu}=\frac{\hbar S_0}{2\rho}\sqrt{\frac{12\rho(1-\sigma^2)}{Eh^2}} \tag{4.38}$$

is a dimensionless parameter that does not depend on the length of the cantilever L. By order of magnitude, $\epsilon\sim\hbar/(Msh)$, where $M\sim\rho/S_0$ is the mass of the material per spin 1/2 and $s\sim\sqrt{E/\rho}$ is the speed of sound. It is easy to see that ϵ is a small parameter that can hardly exceed 0.01 even for the smallest cantilevers. For the given function $\bar{y}_0(\bar{t})$ that describes the motion of the domain wall, Eq. (4.37) has to be solved with the following boundary conditions:

$$\bar{u}_z=0\,,\ \frac{\partial\bar{u}_z}{\partial\bar{y}}=0\quad\text{at}\quad\bar{y}=0\,,$$
$$\frac{\partial^2\bar{u}_z}{\partial\bar{y}^2}=0\,,\ \frac{\partial^3\bar{u}_z}{\partial\bar{y}^3}=0\quad\text{at}\quad\bar{y}=1\,. \tag{4.39}$$

The first two conditions correspond to the absence of displacement and the absence of bending of the cantilever at the fixed end, while the last two conditions correspond to the absence of torque and force, respectively, at the free end [95]. For the free oscillations of the cantilever, $\epsilon = 0$, one writes

$$\bar{u}_z(\bar{y},\bar{t}) = \bar{u}(\bar{y})\cos(\bar{\omega}\bar{t})\,. \tag{4.40}$$

Substitution into Eq. (4.37) with $\epsilon = 0$ then gives

$$\frac{\partial^4 \bar{u}}{\partial \bar{y}^4} - \kappa^4 \bar{u} = 0\,, \qquad \kappa^2 \equiv \bar{\omega}\,. \tag{4.41}$$

The general solution of this equation is

$$\bar{u}(\bar{y}) = A\cos(\kappa\bar{y}) + B\sin(\kappa\bar{y}) + C\cosh(\kappa\bar{y}) + D\sinh(\kappa\bar{y})\,, \tag{4.42}$$

where A, B, C, D are constants of integration. With the help of the first, second, and fourth boundary conditions (4.39) one obtains

$$C = -A\,, \quad D = -B\,, \quad B = \frac{\sin\kappa - \sinh\kappa}{\cos\kappa + \cosh\kappa}A\,. \tag{4.43}$$

Substitution of these expressions into Eq. (4.42) gives up to a normalization factor

$$\begin{aligned}\bar{u}(\bar{y}) &= (\cos\kappa + \cosh\kappa)\left[\cos(\kappa\bar{y}) - \cosh(\kappa\bar{y})\right] \\ &+(\sin\kappa - \sinh\kappa)\left[\sin(\kappa\bar{y}) - \sinh(\kappa\bar{y})\right]\,.\end{aligned} \tag{4.44}$$

The third of the boundary conditions (4.39) provides equation,

$$\cos\kappa\cosh\kappa + 1 = 0\,, \tag{4.45}$$

for the frequencies of the normal modes of the cantilever, $\bar{\omega}_n = \kappa_n^2$ (measured in the units of ν of Eq. (4.36)). Fundamental (minimal) frequency is $\bar{\omega}_1 \approx 3.516$. The next two frequencies are $\bar{\omega}_2 \approx 22.03$ and $\bar{\omega}_3 \approx 61.70$. The profiles of the oscillations of the cantilever for three normal modes ($n = 1, 2, 3$) are shown in Fig. 4.5.

We shall now turn to the forced oscillations of the cantilever due to motion of the domain wall. We first neglect dissipation and write for the displacement

$$\bar{u}_z(\bar{y},\bar{t}) = \sum_m R_m(\bar{t})\bar{u}_m(\bar{y})\,, \tag{4.46}$$

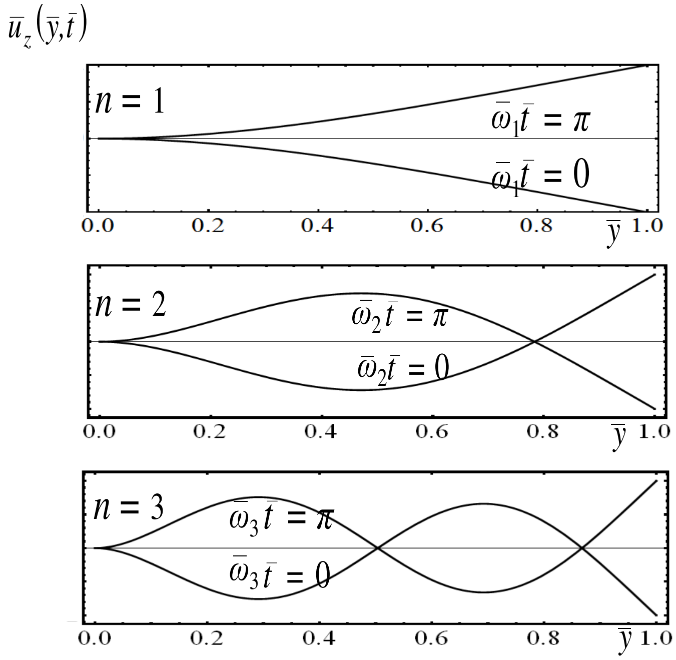

Figure 4.5: Profiles of the oscillating cantilever at different moments of time for $n = 1, 2, 3$.

where $R_m(t)$ are functions of time to be determined and $\bar{u}_m(\bar{y})$ are normalized eigenfunctions (4.44) of the free cantilever that correspond to eigenvalues κ_m given by Eq. (4.45),

$$\int_0^1 dy\, \bar{u}_m(\bar{y})\bar{u}_n(\bar{y}) = \delta_{mn}\,. \tag{4.47}$$

Substitution of Eq. (4.46) into Eq. (4.37) gives

$$\sum_m \left(\frac{d^2 R_m}{d\bar{t}^2} + \bar{\omega}_m^2 R_m \right) \bar{u}_m(\bar{y}) = -\epsilon \left(\frac{d\bar{y}_0}{d\bar{t}} \right) \frac{\partial^2 F}{\partial \bar{y}^2}\,, \tag{4.48}$$

where we have used Eq. (4.41). Multiplying both parts of this equation by $\bar{u}_n(\bar{y})$ and integrating over $\bar{y}$ from 0 to 1 with account of Eq. (4.47), one obtains linear second-order differential equation for $R_n(\bar{t})$,

$$\frac{d^2 R_n}{d\bar{t}^2} + \bar{\omega}_n^2 R_n = -\epsilon \left(\frac{d\bar{y}_0}{d\bar{t}}\right) \int_0^1 d\bar{y} \frac{\partial^2 F}{\partial \bar{y}^2} \bar{u}_n(\bar{y})\,. \tag{4.49}$$

When the width of the domain wall is small compared to the length of the cantilever, the first derivative of F can be replaced by the δ-function,

$$\frac{\partial F}{\partial \bar{y}} = 2\delta[\bar{y} - \bar{y}_0(\bar{t})]\,. \tag{4.50}$$

In this case, integrating by parts in the right-hand side of Eq. (4.49), one obtains

$$\begin{aligned} \frac{d^2 R_n}{d\bar{t}^2} + \bar{\omega}_n^2 R_n &= 2\epsilon \left(\frac{d\bar{y}_0}{d\bar{t}}\right) \left(\frac{d\bar{u}_n}{d\bar{y}}\right)_{\bar{y}=\bar{y}_0(\bar{t})} \\ &= -2\epsilon \frac{d}{d\bar{t}} \bar{u}_n\left[\bar{y}_0(\bar{t})\right]\,. \end{aligned} \tag{4.51}$$

Dissipation can be included into the problem by adding the first time derivative of R_n to this equation. This results in a conventional problem of damped oscillations induced by a periodic force:

$$\frac{d^2 R_n}{d\bar{t}^2} + \frac{\bar{\omega}_n}{Q_n}\frac{dR_n}{d\bar{t}} + \bar{\omega}_n^2 R_n = -2\epsilon \frac{d}{d\bar{t}} \bar{u}_n\left[\bar{y}_0(\bar{t})\right]\,. \tag{4.52}$$

Here Q_n is the quality factor of the oscillations of the cantilever at the eigenfrequency $\bar{\omega}_n$. The most interesting case is when the position of the domain wall,

$$\bar{y}_0(\bar{t}) = \bar{b} + \bar{a}\sin(\bar{\omega}\bar{t})\,, \tag{4.53}$$

oscillates at a frequency $\bar{\omega}$ that is close to one of the resonant frequencies of the cantilever $\bar{\omega}_n = \kappa_n^2$. To solve Eq. (4.52) we write u_n and R_n as Fourier series,

$$u_n(\bar{t}) = \sum_{k=-\infty}^{\infty} u_k^{(n)} e^{ik\bar{\omega}\bar{t}}\,, \qquad R_n(\bar{t}) = \sum_{k=-\infty}^{\infty} r_k^{(n)} e^{ik\bar{\omega}\bar{t}}\,. \tag{4.54}$$

Substitution into Eq. (4.52) gives

$$r_k^{(n)} = \frac{-2i\epsilon k\bar{\omega} u_k^{(n)}}{\bar{\omega}_n^2 - k^2\bar{\omega}^2 + \frac{ik\bar{\omega}\bar{\omega}_n}{Q_n}}\,, \tag{4.55}$$

where

$$u_k^{(n)}(\bar{a},\bar{b}) = \frac{1}{2\pi}\int_0^{2\pi} d\xi e^{-ik\xi}\bar{u}_n\left(\bar{b}+\bar{a}\sin\xi\right) \ . \tag{4.56}$$

Writing $u_k^{(n)}$ as $u_k^{(n)} = |u_k^{(n)}|\exp[i\gamma_k^{(n)}]$ one obtains the following expressions for the amplitude $|r_k^{(n)}|$ and phase $\delta_k^{(n)}$ of the k-th harmonic of $R_n(t)$:

$$|r_k^{(n)}| = \frac{2\epsilon k\bar{\omega}|u_k^{(n)}|}{\sqrt{(k^2\bar{\omega}^2-\bar{\omega}_n^2)^2+\left(\frac{k\bar{\omega}\bar{\omega}_n}{Q_n}\right)^2}} \tag{4.57}$$

$$\delta_k^{(n)} = \gamma_k^{(n)} - \frac{\pi}{2} + \arctan\left[\frac{k\bar{\omega}\bar{\omega}_n}{Q_n(k^2\bar{\omega}^2-\bar{\omega}_n^2)}\right] \ . \tag{4.58}$$

According to Eq. (4.57), resonances occur at frequencies $\omega = \omega_n/k$ that are independent of damping. At $\omega = \omega_n/k$ the maximum displacement of the free end of the cantilever is given by

$$\bar{u}_z(1) = \epsilon Q_n P_k^{(n)}(\bar{a},\bar{b})\,, \tag{4.59}$$

where

$$P_k^{(n)}(\bar{a},\bar{b}) = \frac{2\bar{u}_n(1)}{\bar{\omega}_n}\left|u_k^{(n)}(\bar{a},\bar{b})\right| \ . \tag{4.60}$$

The dependence of $P_k^{(n)}$ on $\bar{a}$ and $\bar{b}$ for various k and n is illustrated in Fig. 4.6.

Note the non-monotonic dependence of the amplitude of the free end on the equilibrium position of the domain wall for $n = 2$ and $n = 3$. It is due to the profile of the normal modes of the cantilever shown in Fig. 4.5. When equilibrium position of the wall coincides with the antinode, the effect of the oscillation of the wall on the cantilever is minimal.

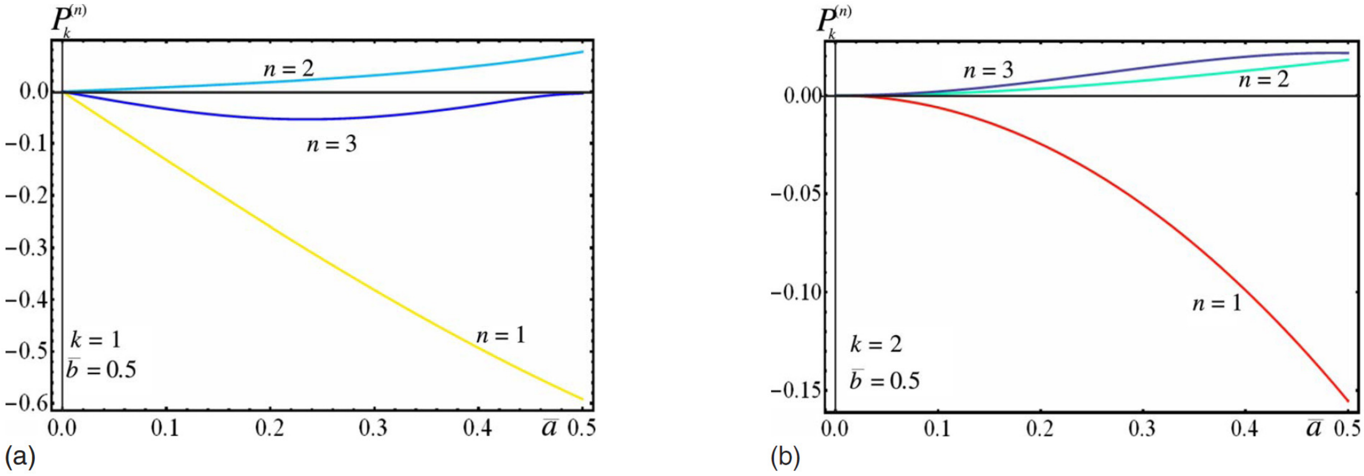

Figure 4.6: The dependence of $P_k^{(n)}(\bar{a}, \bar{b})$ on the amplitude of the oscillations of the domain wall whose equilibrium position is in the middle of the cantilever: a) $k = 1$, b) $k = 2$.

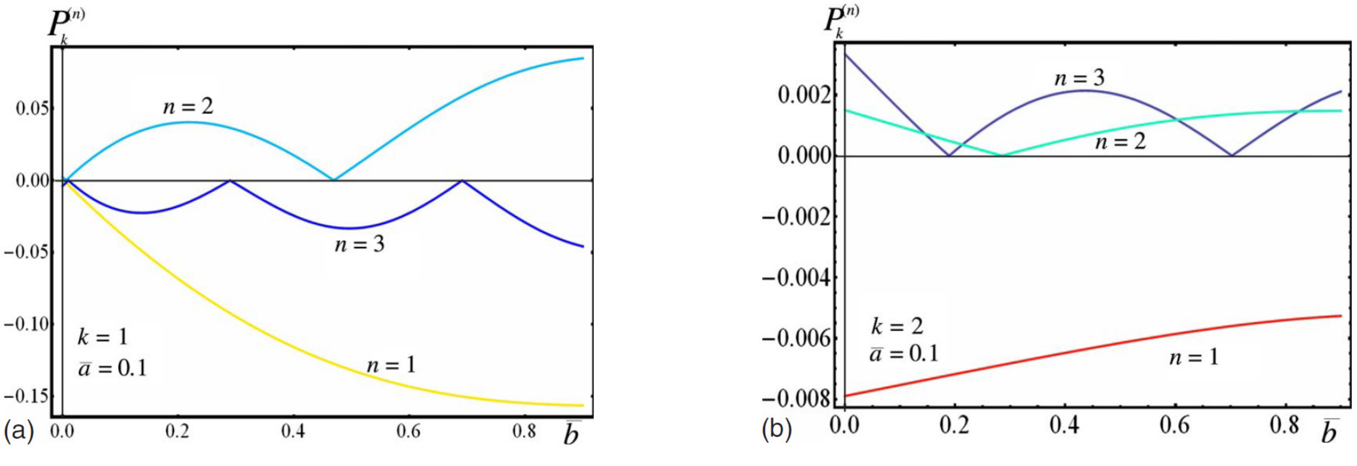

Figure 4.7: The dependence of $P_k^{(n)}(\bar{a}, \bar{b})$ on the equilibrium position of the domain wall for $n = 1, 2, 3$ and $k = 1, 2$.

4.3.3 Suggestions for Experiment and Comparison With NIST's Experiment

Expressions derived in this chapter provide the framework for theoretical analysis of the experimental data on Einstein - de Haas effect. To illustrate applications of the theory we have derived rigorous formulas for the mechanical motion of a magnetic cantilever, induced by the motion of a domain wall when the cantilever is placed in the ac magnetic field. In our theory we assumed that the entire volume of the cantilever was magnetic. The formulas can be easily adjusted, however, to the situation when the magnetic layer has thickness $ph < h$, as was the case in the NIST experiment. In this case the strength of the source in the right hand side of Eq. (4.37) reduces by the factor p. Consequently, one should replace ϵ in the above formulas with $\epsilon_p = p\epsilon < \epsilon$.

Accurate comparison between theory and experiment requires precise knowledge of the mechanism by which the magnetic moment is changing. If it is due to the motion of the domain wall, as we believe was the case in the NIST experiment [82], then one needs to know the initial equilibrium position b and the amplitude of the oscillations of the wall a. The parameter b can be controlled by a weak dc magnetic field, while a can be controlled by the amplitude of the ac field. It is also desirable to excite various harmonics ω_n/k and to identify the fundamental frequency ω_1. This would allow one to obtain the value of the parameter ν in equations (4.36) and (4.38). If the magnetization and the g-factor are known, the ratio S_0/ρ in the first of Eq. (4.38) can be computed with good accuracy. The precision with which the parameter ϵ can be determined will then depend on the knowledge of the length of the cantilever L. Alternatively, ϵ can be extracted from experiment and used to obtain the spin density S_0. If the magnetization M_0 is known this would allow one to obtain the gyromagnetic factor $g = M_0/(\mu_B S_0)$.

In the NIST experiment the fraction of the magnetic material p was close to $1/12$ while the dimensions of the cantilever were $L = 2 \times 10^{-4}$m, $h = 6 \times 10^{-7}$m. This gives $\epsilon_p \sim 10^{-7}$. If a is comparable to L, then according to Eq. (4.59), the deflection of the free end of the cantilever at the fundamental frequency $\omega = \omega_1$ must be of order $\epsilon_p Q_1 L$. The observed deflection in the nanometer range then corresponds to $Q_1 \sim 100$. We should notice in this connection that the effect could be stronger for a cantilever with a higher quality factor. As a matter of fact the quality factors as high as $10,000$ have been reported for microcantilevers [90]. For a cantilever of length $L = 0.2$mm such a high quality factor would allow the deflection of the free end due to Einstein - de Haas effect as high as a few tens of a micrometer. This work led up to think about another problem: what if we replace the magnetic layer with a single molecule magnet? In the next chapter, we report on how to detect quantum oscillations of the spin of a single molecule magnet through its resonant coupling to the mechanical modes of a microcantilever.

Chapter 5

Magnetic Molecule on a Microcantilever

Magnetic molecules exhibit quantum tunneling between different orientations of the spin in macroscopic magnetization measurements [2, 24]. Detection of coherent quantum spin oscillations, similar to those observed in a SQUID [91], would be of great interest. In a crystal of magnetic molecules this effect is difficult to observe because of the inhomogeneous broadening of spin levels and decoherence arising from various interactions. Nevertheless a significant progress has been recently made in this direction [92]. Magnetic measurements of individual molecules would have been more promising because of low inhomogeneous broadening of spin levels and low decoherence [93]. However insufficient sensitivity of existing magnetometers has prohibited such studies so far. Efforts have been made to observe spin tunneling effects in the electron transport through a single magnetic molecule bridged between metallic electrodes [96] which we will report on in the next chapter.

In this chapter, we show our work on how to detect quantum oscillations of the spin of a single magnetic molecule through their resonant coupling to the mechanical modes of a microcantilever [97].

5.1 Projection on a Two-State System

In chapter 2, we showed that for a uniaxial spin Hamiltonian, for low values of the transverse field, the problem of finding the eigenstates and eigenvalues is essentially reduced to a two-state problem with known solutions. The geometry of the proposed experiment is shown in Fig.5.1.

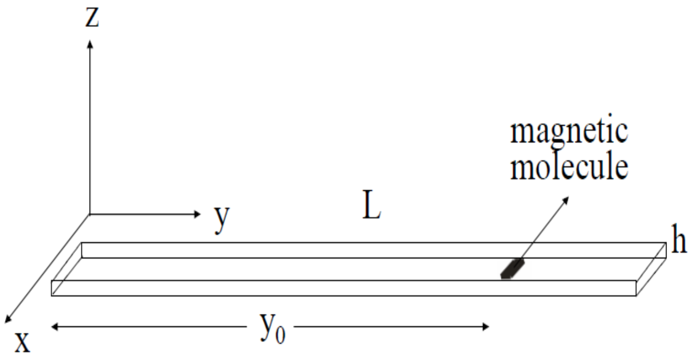

Figure 5.1: The geometry of the problem.

A magnetic molecule of spin **S** is deposited on a microcantilever of length L, Fig. 5.1. The $y = 0$ end of the cantilever is fixed while the $y = L$ end is free. The molecule is assumed to be imbedded in or firmly attached to the cantilever at $y = y_0$, with the magnetic anisotropy axis being parallel the X-direction. Let Δ be the tunnel splitting of the two lowest energy states of the molecule,

$$|\Psi_\pm\rangle = \frac{1}{\sqrt{2}}\left(|S\rangle \pm |-S\rangle\right) , \tag{5.1}$$

where $|\pm S\rangle$ denote two opposite spin orientations along the X-axis. A weak ac magnetic field of frequency $\omega = \Delta/\hbar$, applied along the X-axis, will force the spin of the molecule to oscillate between the two orientations. Conservation of the total angular momentum requires that the oscillations of the spin are accompanied by the mechanical oscillations of the cantilever (Einstein - de Haas effect [77, 82]). Consequently, if $\omega = \Delta/\hbar$ coincides with a resonant mode of the cantilever, one should expect the effect of the ac field on the cantilever.

If the cantilever rotates by a small angle $\delta\boldsymbol{\phi}$ at the location of the spin, the Hamiltonian of the molecule $\hat{H}_S$ becomes [84, 94]

$$\hat{H}'_S = \hat{R}\hat{H}_S\hat{R}^{-1} = \hat{H}_S + i\sum\left[\hat{H}_S, \mathbf{S}\right]\cdot\delta\boldsymbol{\phi} = \hbar\dot{\mathbf{S}}\cdot\delta\boldsymbol{\phi}\,. \tag{5.2}$$

Due to strong magnetic anisotropy the molecule can be considered as a two-state system. The Hamiltonian of such a system, $\mathcal{H}_2$, is a projection of the Hamiltonian (5.2) onto the two states given by Eq. (5.1). These states can be viewed as the eigenstates of the Pauli matrix σ_z. For the geometry shown in Fig. 5.1 the projection can be performed by writing

$$\mathcal{H}_2 = \sum_{i,j=\pm}\langle\Psi_i|\left(\hat{\mathcal{H}}_S + i\left[\hat{\mathcal{H}}_S, S_x\right]\delta\phi_x\right)|\Psi_j\rangle|\Psi_i\rangle\langle\Psi_j| \tag{5.3}$$

with

$$\sigma_x = |\Psi_+\rangle\langle\Psi_-| + |\Psi_-\rangle\langle\Psi_+| \tag{5.4}$$

$$\sigma_y = -i|\Psi_+\rangle\langle\Psi_-| + i|\Psi_-\rangle\langle\Psi_+| \tag{5.5}$$

$$\sigma_z = |\Psi_+\rangle\langle\Psi_+| - |\Psi_-\rangle\langle\Psi_-|\,. \tag{5.6}$$

This gives

$$\mathcal{H}_2 = -\frac{1}{2}\Delta\sigma_z + S\Delta\delta\phi_x\sigma_y\,. \tag{5.7}$$

with $\mathcal{H}_2$ can be written as:

$$\mathcal{H}_2 = \mathcal{H}_s^{eff} + \mathcal{H}_{ph} + \mathcal{H}_{s-ph} = (\frac{\Delta}{2}\mathbf{e}_z - S\Delta\delta\phi_x\mathbf{e}_y)\cdot\sigma + \mathcal{H}_{ph} = -\frac{1}{2}\mathbf{b}_{\text{eff}}\cdot\sigma + \mathcal{H}_{ph} \quad (5.8)$$

The states with a definite X-projection of the spin are eigenstates of σ_x: $|\pm S\rangle = \frac{1}{\sqrt{2}}(|\Psi_+\rangle \pm |\Psi_-\rangle)$. The expectation value of $\boldsymbol{\sigma}$ satisfies the Landau-Lifshitz equation:

$$\hbar\dot{\boldsymbol{\sigma}} = -\boldsymbol{\sigma}\times\mathbf{b}_{\text{eff}}\,, \quad (5.9)$$

with

$$\mathbf{b}_{\text{eff}} = -\Delta\mathbf{e}_z + 2S\Delta\delta\phi_x\mathbf{e}_y\,. \quad (5.10)$$

If the cantilever was held stationary ($\delta\phi_x = 0$), the solution of Eq. (5.9) would describe pure quantum oscillations of the spin: $\sigma_z = const, \sigma_x \propto \cos(\Delta t/\hbar), \sigma_y \propto \sin(\Delta t/\hbar)$.

5.2 Coupled Dynamics of Spin and Cantilever

We are interested in the coupled oscillations of the spin and the cantilever. Since the latter contains macroscopic number of atoms, its oscillations can be studied within a continuous elastic theory that deals with the displacement field $\mathbf{u}(\mathbf{r},t)$ and the local rotation $\delta\boldsymbol{\phi}$ given by [95]

$$\delta\phi(\mathbf{r}) = \frac{1}{2}\nabla\times\mathbf{u}(\mathbf{r})\,. \quad (5.11)$$

Within such a model the spin of the molecule at a point $\mathbf{r}_0$ can be replaced by the spin field

$$\boldsymbol{\Sigma}(\mathbf{r},t) = S\boldsymbol{\sigma}(t)\delta(\mathbf{r}-\mathbf{r}_0)\,, \quad (5.12)$$

where $\boldsymbol{\sigma}(t)$ satisfies Eq. (5.9). With account of Eq. (5.2) the energy of the cantilever becomes

$$\mathcal{H}_C = \mathcal{H}_E + \frac{1}{2}\int d^3r\,\hbar\dot{\boldsymbol{\Sigma}}\cdot(\nabla\times\mathbf{u})\,, \quad (5.13)$$

where $\mathcal{H}_E$ is the part of the elastic energy that is independent of the spin.

The dynamical equation for the displacement field is

$$\rho\frac{\partial^2 u_\alpha}{\partial t^2} = \frac{\partial\sigma_{\alpha\beta}}{\partial x_\beta}\,, \quad (5.14)$$

where $\sigma_{\alpha\beta} = \delta\mathcal{H}_C/\delta e_{\alpha\beta}$ is the stress tensor, $e_{\alpha\beta} = \partial u_\alpha/\partial x_\beta$ is the strain tensor, and ρ is the mass density of the material. This gives

$$\rho\frac{\partial^2 u_\alpha}{\partial t^2} - \frac{\partial\sigma^{(\mathrm{E})}_{\alpha\beta}}{\partial x_\beta} = -\frac{\hbar}{2}\boldsymbol{\nabla}\times\dot{\boldsymbol{\Sigma}} \tag{5.15}$$

where $\sigma^{(\mathrm{E})}_{\alpha\beta} = \delta\mathcal{H}_E/\delta e_{\alpha\beta}$. It is easy to see that in the absence of the external torque, $K^{(E)}_\alpha = \oint dA_\delta\left[\epsilon_{\alpha\beta\gamma}r_\beta\sigma^{(E)}_{\gamma\delta}\right]$, applied to the surface of the body $\mathbf{A}$, Eq. (5.15) provides conservation of the total angular momentum,

$$\mathbf{J} = \int d^3r\left[\hbar\boldsymbol{\Sigma} + \rho\left(\mathbf{r}\times\dot{\mathbf{u}}\right)\right]\,, \quad d\mathbf{J}/dt = 0\,. \tag{5.16}$$

Writing the left-hand side of Eq. (5.15) in the conventional form for a cantilever [95] one obtains the elastic equation that couples vertical displacements of the cantilever, $u_z(y,t)$, with the oscillations of the spin:

$$\rho\frac{\partial^2 u_z}{\partial t^2} + \frac{h^2 E}{12(1-\sigma^2)}\frac{\partial^4 u_z}{\partial y^4} = \frac{\hbar S}{2V}\frac{\partial}{\partial y}\frac{\partial}{\partial t}\left[\sigma_x(t)L\delta(y-y_0)\right]\,. \tag{5.17}$$

Here h and V are the thickness and the volume of the cantilever, respectively, E is the Young's modulus, and σ is the Poisson coefficient, $-1 < \sigma < 1/2$.

It is convenient to switch in Eq. (5.17) to dimensionless variables $\bar{u}_z = u_z/L, \bar{y} = y/L, \bar{t} = t\nu$, where

$$\nu \equiv \sqrt{\frac{Eh^2}{12\rho(1-\sigma^2)L^4}} \tag{5.18}$$

determines the scale of the eigenfrequencies of the oscillations of the cantilever. By order of magnitude $\nu \sim v_s h/L^2$ where $v_s \sim \sqrt{E/\rho}$ is the speed of sound. In terms of these variables Eq. (5.17) becomes

$$\frac{\partial^2\bar{u}_z}{\partial\bar{t}^2} + \frac{\partial^4\bar{u}_z}{\partial\bar{y}^4} = \frac{\epsilon}{2}\frac{\partial}{\partial\bar{y}}\frac{\partial}{\partial\bar{t}}\left[\sigma_x(\bar{t})\delta(\bar{y}-\bar{y}_0)\right]\,, \tag{5.19}$$

where $0 < \bar{y}_0 < 1$ and

$$\epsilon = \frac{\hbar S}{ML^2\nu} = \frac{\hbar S}{M}\sqrt{\frac{12\rho(1-\sigma^2)}{Eh^2}} \tag{5.20}$$

is a dimensionless small parameter. By order of magnitude, $\epsilon \sim \hbar S/(Mv_s h)$, where $M = \rho V$ is the mass of the cantilever. For, e.g., a molecule of spin $S = 10$ on a cantilever of dimensions 100nm×10nm×1nm the parameter ϵ should be of order 10^{-7}. Eq. (5.19) has to be solved with the following boundary conditions:

$$\bar{u}_z = 0\,, \ \frac{\partial \bar{u}_z}{\partial \bar{y}} = 0 \quad \text{at} \quad \bar{y} = 0\,,$$
$$\frac{\partial^2 \bar{u}_z}{\partial \bar{y}^2} = 0\,, \ \frac{\partial^3 \bar{u}_z}{\partial \bar{y}^3} = 0 \quad \text{at} \quad \bar{y} = 1\,. \tag{5.21}$$

The first two conditions correspond to the absence of displacement and the absence of bending of the cantilever at the fixed end, while the last two conditions correspond to the absence of torque and force, respectively, at the free end [95].

For the free oscillations of the cantilever ($\epsilon = 0$) one writes

$$\bar{u}_z(\bar{y}, \bar{t}) = \bar{u}(\bar{y}) \cos(\bar{\omega}\bar{t})\,. \tag{5.22}$$

Substitution into Eq. (5.19) with $\epsilon = 0$ then gives

$$\frac{\partial^4 \bar{u}}{\partial \bar{y}^4} - \kappa^4 \bar{u} = 0\,, \qquad \kappa^2 \equiv \bar{\omega}\,. \tag{5.23}$$

Solutions are

$$\bar{u}(\bar{y}) = (\cos\kappa + \cosh\kappa)\left[\cos(\kappa\bar{y}) - \cosh(\kappa\bar{y})\right]$$
$$+(\sin\kappa - \sinh\kappa)\left[\sin(\kappa\bar{y}) - \sinh(\kappa\bar{y})\right]\,. \tag{5.24}$$

The third of the boundary conditions (5.21) provides the equation,

$$\cos\kappa \cosh\kappa + 1 = 0\,, \tag{5.25}$$

for the frequencies of the normal modes of the cantilever, $\bar{\omega}_n = \kappa_n^2$ (measured in the units of ν of Eq. (5.18)). The fundamental (minimal) frequency is $\bar{\omega}_1 \approx 3.516$. The next two frequencies are $\bar{\omega}_2 \approx 22.03$ and $\bar{\omega}_3 \approx 61.70$. The profiles of the oscillations of the cantilever for three normal modes ($n = 1, 2, 3$) are shown in Fig. 4.5 in chapter 4.

To consider coupled oscillations of the cantilever and the spin of the molecule we first neglect dissipation and write for the displacement

$$\bar{u}_z(\bar{y}, \bar{t}) = \sum_m R_m(\bar{t}) \bar{u}_m(\bar{y})\,, \tag{5.26}$$

where $R_m(t)$ are functions of time to be determined and $\bar{u}_m(\bar{y})$ is a normalized eigenfunction (5.24) that corresponds to the eigenvalue κ_m given by Eq. (5.25),

$$\int_0^1 dy\, \bar{u}_m(\bar{y})\bar{u}_n(\bar{y}) = \delta_{mn}\,. \tag{5.27}$$

Substitution of Eq. (5.26) into Eq. (5.19) gives

$$\sum_m \left(\frac{d^2 R_m}{d\bar{t}^2} + \bar{\omega}_m^2 R_m\right)\bar{u}_m(\bar{y}) = \frac{\epsilon}{2}\frac{d}{d\bar{t}}\frac{d}{d\bar{y}}[\sigma_x(\bar{t})\delta(\bar{y}-\bar{y}_0)]\,, \tag{5.28}$$

where we have used Eq. (5.23). Multiplying both parts of this equation by $\bar{u}_n(\bar{y})$ and integrating over $\bar{y}$ from 0 to 1 with account of Eq. (5.27), one obtains linear second-order differential equation for $R_n(\bar{t})$,

$$\frac{d^2 R_n}{d\bar{t}^2} + \bar{\omega}_n^2 R_n = -\frac{\epsilon}{2}\left(\frac{d\sigma_x}{d\bar{t}}\right)\bar{u}_n'(\bar{y}_0)\,, \tag{5.29}$$

where $\bar{u}_n'(\bar{y}_0) \equiv (d\bar{u}_n/d\bar{y})_{\bar{y}=\bar{y}_0}$.

Coupled magneto-mechanical oscillations near the ground state correspond to small σ_x, σ_y, R_n, and $\sigma_z \approx 1$. This requires temperatures $k_BT \ll \Delta$. In this case Eq. (5.9) gives for σ_x

$$\frac{d^2\sigma_x}{d\bar{t}^2} + \bar{\Delta}^2\sigma_x = S\bar{\Delta}\bar{u}_n'(\bar{y}_0)\frac{dR_n}{d\bar{t}}, \tag{5.30}$$

where $\bar{\Delta} \equiv \Delta/(\hbar\nu)$. Substituting into Eqs. (5.29) and (5.30) $\sigma_x(\bar{t}), R_n(\bar{t}) \propto \exp(i\bar{\omega}\bar{t})$, one obtains the following equation for the eigenmodes of the coupled oscillations:

$$(\bar{\omega}^2 - \bar{\omega}_n^2)(\bar{\omega}^2 - \bar{\Delta}^2) = \frac{1}{2}\epsilon S\bar{\Delta}\bar{u}_n'^2(\bar{y}_0)\bar{\omega}^2\,. \tag{5.31}$$

Due to the smallness of ϵ, oscillations of the spin and the cantilever occur independently at frequencies $\Delta/\hbar$ and ω_n, respectively, unless these two frequencies are very close to each other. The latter can be achieved by, e.g., changing Δ with the help of the dc magnetic field perpendicular to the anisotropy axis of the molecule. At $\Delta = \hbar\omega_n$ one should observe the splitting of the mechanical mode of the cantilever, ω_n, into two modes

$$\omega_{n\pm} = \omega_n\left(1 \pm \frac{\delta}{2}\right)\,, \quad \delta = \sqrt{\frac{\epsilon S\bar{u}_n'^2(\bar{y}_0)}{2\bar{\omega}_n}}\,. \tag{5.32}$$

The remarkable property of Eq. (5.32) is that it has no free parameters. For a chosen resonance $\Delta = \hbar\omega_n$, the relative splitting δ depends only on the position of the molecule on the cantilever. We will explore various plots of δ in the next section.

5.3 Quantum Magneto-Mechanical Oscillations

The dependence of the splitting of the first three cantilevers modes on the position of the molecule is shown in figure 5.2.

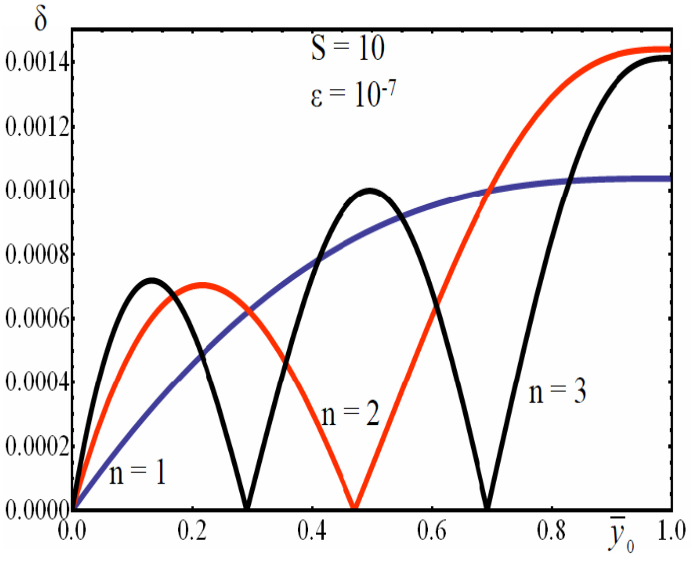

Figure 5.2: The dependence of the splitting of the first three cantilevers modes on the position of the molecule.

As expected, the first resonance $n = 1$ has no nodes whereas the second one $n = 2$ has one node and the third resonance $n = 3$ has two nodes.

We shall now demonstrate that the above experiment can be performed by studying the response of the system to a weak ac magnetic field, $\mathbf{B}(t) = B_0\mathbf{e}_x \sin(\omega t)$, applied along the anisotropy axis of the magnetic molecule. In the presence of such a field $\mathbf{b}_{\text{eff}}$ becomes

$$\mathbf{b}_{\text{eff}} = -\Delta\mathbf{e}_z + 2S\Delta\delta\phi_x\mathbf{e}_y + b\mathbf{e}_x \sin(\omega t)\,, \tag{5.33}$$

where $b = g\mu_B B_0$, with g being the gyromagnetic factor for the spin and μ_B being the Bohr magneton. To obtain the amplitude of the forced oscillations of the cantilever we need to include dissipation in the equations of motion of the spin and the cantilever. The damping modifies the Landau-Lifshitz equation [10]:

$$\hbar\dot{\boldsymbol{\sigma}} = -\boldsymbol{\sigma} \times \mathbf{b}_{\text{eff}} + 2Q_s^{-1}\boldsymbol{\sigma} \times (\boldsymbol{\sigma} \times \mathbf{b}_{\text{eff}})\;. \tag{5.34}$$

Here Q_s is the quality factor of the spin oscillations. Small oscillations ($|\sigma_{x,y}| \ll 1, \sigma_z \approx 1$) now satisfy

$$\frac{d\sigma_\pm}{d\bar{t}} + \bar{\Delta}\left(Q_s^{-1} \pm i\right)\sigma_\pm = S\bar{\Delta}\bar{u}_n'(\bar{y}_0)R_n \mp i\bar{b}\sin(\bar{\omega}\bar{t}) \tag{5.35}$$

where $\sigma_\pm = \sigma_x \pm i\sigma_y$ and $\bar{b} \equiv b/(\hbar\nu)$.

Dissipation of the mechanical motion of the cantilever can be introduced by adding the first time derivative of R_n to Eq. (5.29):

$$\frac{d^2R_n}{d\bar{t}^2} + \frac{\bar{\omega}_n}{Q_n}\frac{dR_n}{d\bar{t}} + \bar{\omega}_n^2 R_n = -\frac{\epsilon}{4}\bar{u}_n'(\bar{y}_0)\frac{d}{dt}(\sigma_+ + \sigma_-)\,. \tag{5.36}$$

Here Q_n is the quality factor of the oscillations of the cantilever at the eigenfrequency $\bar{\omega}_n$. One can now obtain the time dependence of R_n and $\sigma_\pm$ by solving together Eq. (5.35) and Eq. (5.36). The displacement of the cantilever at a point y is given by $\bar{u}_z(\bar{t}, \bar{y}) = R_n(\bar{t})\bar{u}_n(\bar{y})$. The simplest way to obtain the solution is to replace $i\sin(\bar{\omega}\bar{t})$ in Eq. (5.35) with $\exp(i\bar{\omega}\bar{t})$ and solve the resulting three algebraic equations for $R_n, s_\pm \propto \exp(i\bar{\omega}\bar{t})$. This gives the following expressions for the amplitudes of the oscillations:

$$|\bar{u}_z(\bar{y})| = \frac{1}{2}\bar{b}\epsilon\bar{\omega}\bar{\Delta}|\bar{u}'_n(\bar{y}_0)||\bar{u}_n(\bar{y})| \times \\ \left\{\left[(\bar{\omega}^2-\bar{\omega}_n^2)(\bar{\omega}^2-\bar{\Delta}^2)-\frac{1}{2}\epsilon S\bar{\Delta}\bar{u}'^2_n(\bar{y}_0)\bar{\omega}^2\right]^2+\bar{\omega}^2\left[\frac{2}{Q_s}\bar{\Delta}(\bar{\omega}^2-\bar{\omega}_n^2)+\frac{1}{Q_n}\bar{\omega}_n(\bar{\omega}^2-\bar{\Delta}^2)\right]^2\right\}^{-1/2} \tag{5.37}$$

and

$$|\sigma_\pm| = \bar{b}\left\{\left[\left(\bar{\omega}\mp\bar{\Delta}\right)\left(\bar{\omega}^2-\bar{\omega}_n^2\right)-\frac{1}{2}\epsilon S\bar{\Delta}\bar{u}'^2_n(\bar{y}_0)\bar{\omega}\right]^2+\left[\frac{\bar{\Delta}}{Q_s}\left(\bar{\omega}^2-\bar{\omega}_n^2\right)+\frac{\bar{\omega}\bar{\omega}_n}{Q_n}\left(\bar{\omega}\mp\bar{\Delta}\right)\right]^2\right\}^{1/2} \times \\ \left\{\left[(\bar{\omega}^2-\bar{\omega}_n^2)(\bar{\omega}^2-\bar{\Delta}^2)-\frac{1}{2}\epsilon S\bar{\Delta}\bar{u}'^2_n(\bar{y}_0)\bar{\omega}^2\right]^2+\bar{\omega}^2\left[\frac{2}{Q_s}\bar{\Delta}(\bar{\omega}^2-\bar{\omega}_n^2)+\frac{1}{Q_n}\bar{\omega}_n(\bar{\omega}^2-\bar{\Delta}^2)\right]^2\right\}^{-1/2} \tag{5.38}$$

The applicability of the above equations is limited by the range of variables that provides the condition $|s_\pm| \ll 1$ used to derive Eq. (5.35) from Eq. (5.9). It is easy to see from Eq. (5.38) that this requirement is easily violated for s_- when ω is close to Δ. This is an indication of the breakdown of the linear approximation for the dynamics of the spin that occurs due to the strong pumping of the spin excitations by the ac field. To avoid this problem, let us consider oscillations at, e.g., $\omega = \omega_n \neq \Delta$, in the practical range of the quality factor $1 \ll Q_n \ll 1/\epsilon$. In this case, one obtains from Eqs. (5.37) and (5.38)

$$|\bar{u}_z(\bar{y})| = \frac{\bar{b}\epsilon Q_n\bar{\Delta}}{2\bar{\omega}_n|\bar{\omega}_n^2-\bar{\Delta}^2|}|\bar{u}'_n(\bar{y}_0)||\bar{u}_n(\bar{y})|\,, \qquad |\sigma_\pm| = \frac{\bar{b}}{|\bar{\omega}_n\pm\bar{\Delta}|}\,. \tag{5.39}$$

A plot of $|\bar{u}_z(\bar{y})|$ for $y = 1$ (that is at the free end of the cantilever) as a function of $\bar{\omega}$ and $\bar{\Delta}$ for the molecule being positioned at $\bar{y}_0 = 0.9$ along the cantilever is shown in figure 5.3.

The parameter Δ can be controlled by a dc magnetic field applied perpendicular to the anisotropy axis of the molecule. The condition $|\sigma_-| \ll 1$ determines how close to the double resonance, $\Delta = \omega_n$, one can still use equations (5.39): $|\bar{\omega}_n - \bar{\Delta}| \gg \bar{b}/2$. Substitution of $|\bar{\omega}_n - \bar{\Delta}| \approx \bar{b}$ into the first of Eqs. (5.39) provides estimate for the

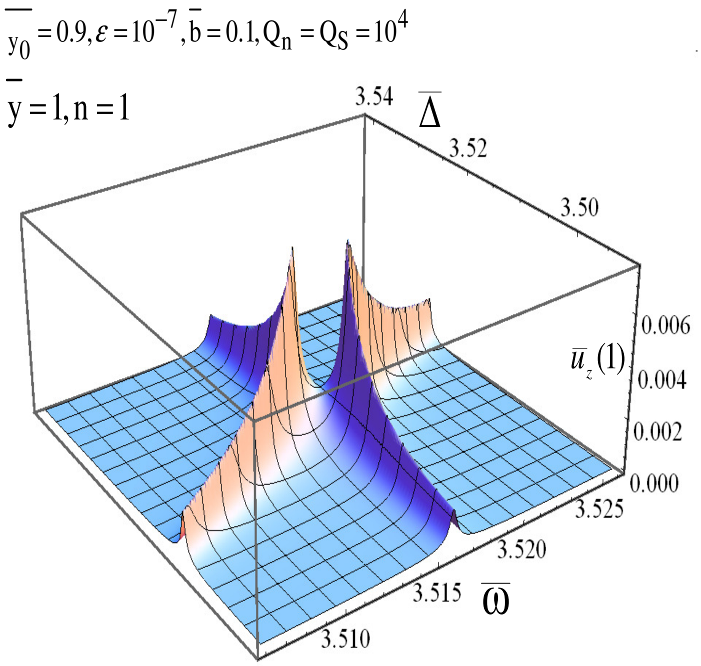

Figure 5.3: 3D plots of the amplitude of oscillation at the free end as a function of $\bar{\Delta}$ and $\bar{\omega}$ when the molecule is at $\bar{y}_0 = 0.9$.

maximum amplitude of the oscillations of the cantilever at $\Delta \to \omega_n$:

$$\max |\bar{u}_z(\bar{y})| \sim \frac{\epsilon Q_n}{4\bar{\omega}_n} |\bar{u}_n'(\bar{y}_0)||\bar{u}_n(\bar{y})| \, . \tag{5.40}$$

Equation 5.40 is valid in the practical range of quality factors $1 \ll Q_{n,s} \ll 1/\epsilon$, and is a function of the distance y from the fixed end of the cantilever, parameterized by the position of the molecule y_0.

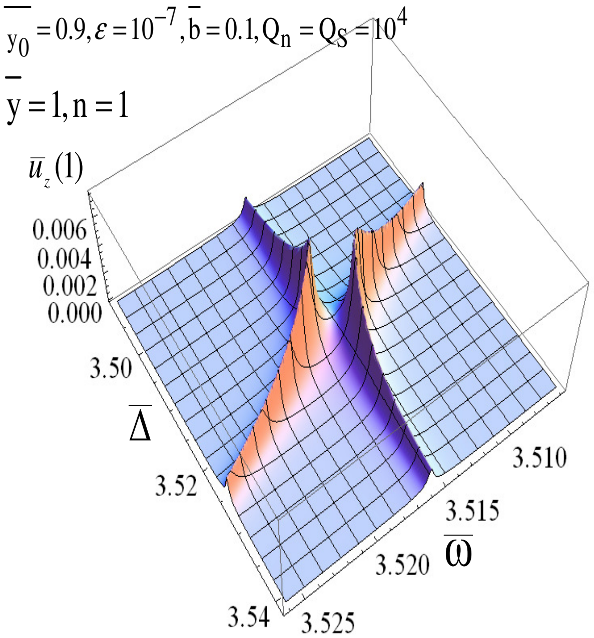

Figure 5.4: 3D plots of the amplitude of oscillation at the free end as a function of $\bar{\Delta}$ and $\bar{\omega}$ when the molecule is at $\bar{y}_0 = 0.9$. It is the same as figure 5.3 but shown from a different angle.

A cantilever of dimensions 100nm×10nm×1nm will have $\nu \sim 10^8 \mathrm{s}^{-1}$, see Eq. (5.18). For the first harmonic of the cantilever, $\omega_1 = 3.52\nu$, the magneto-mechanical resonance will then occur for Δ in the mK range. In that case, $f_1 = 3.52\nu/(2\pi) \approx 30$ MHz and the splitting δf_1 of the first harmonic of the cantilever occurs in the ballpark of a few kilohertz. Note that the splitting of the spin energy levels Δ in a magnetic molecule, regardless of its magnitude, is a well-defined quantity: Δ as low as 0.1μK has been measured in the context of the interference of spin tunneling trajectories [51]. This parameter can be easily controlled by the magnetic field normal to the anisotropy axis. Smaller cantilevers will have higher ν and, thus, will permit work with higher Δ. Our approach is valid when the probability for the molecule to occupy the excited spin levels is small. The first excited state is separated from the ground state by the energy Δ. Consequently, if the system is at thermal equilibrium, the temperature should be low compared to Δ. There are ways around this condition, though. One such a possibility consists of studying resonances at higher harmonics: $\omega_2 = 22.03\nu$, $\omega_3 = 61.70\nu$, and so on. Another possibility follows from the observation that the relaxation of our system towards thermal equilibrium can be very long. Consequently, if one uses the external field to prepare the initial magnetic state of the molecule, the coupled magneto-mechanical oscillations can, in principle, be studied during much shorter times than the time required for thermalization.

Very high quality factors (up to 10^5) have also been reported for mechanical oscillations of microcantilevers [98, 90]. For a cantilever of dimensions 100nm×10nm×1nm, carrying a magnetic molecule of spin 10, the parameter ϵ of Eq. (5.20), responsible for the magneto-mechanical coupling, is of order 10^{-7}. A definitive observation of the coupled quantum magneto-mechanical oscillations would be the detection of the splitting, $\delta\omega_n$, of the mechanical modes of the cantilever. Such a splitting should appear in the spectrum of the cantilever regardless of the measuring procedure. For the first resonance ($\omega = \omega_1$), δ of Eq. (5.32) would be generally of order $\sqrt{\epsilon S} \sim 10^{-3}$. The condition for the detection of the splitting of the cantilever modes is $Q_{n,s} \gg 1/\delta$. This means that the quality factors of $10,000$ reported for microcantilevers should be sufficient to observe this effect. When the molecule is near the tip of the cantilever, Eq. (5.40) with $\epsilon \sim 10^{-7}$ and $Q_n \sim 10^4$ gives for the tip: $|\bar{u}_z| \sim 5 \times 10^{-4}$. For a 100-nm long cantilever this would correspond to the oscillations by 0.05nm. Such a displacement can be detected by tunneling or force microscopy.

The possibility of the observation of quantum magneto-mechanical oscillations studied comes from the resonant nature of the effect. While the coupling between quantum spin oscillations and the mechanical oscillations of the cantilever is always weak, the resonant condition ($\Delta = \omega_n$) generates a large effect similar to the one produced by a very weak periodic resonant force acting on a pendulum with a high quality factor. Working with smaller cantilevers would provide higher values of the coupling parameter ϵ and would relax the requirements on temperature and the quality factors.

In Conclusion, we have shown that driven quantum oscillations of the spin of a magnetic molecule can be observed by placing the molecule on a microcantilever. Since such cantilevers consist of hundreds of thousands of atoms, this would be a remarkable example of a macroscopic quantum effect. Our theory has no free parameters and, therefore, it must be helpful in designing the proposed experiment.

Chapter 6

Magnetic Molecule Between Conducting Leads

In this chapter, we present our work on molecular magnet bridged between two conducting leads. Dynamics of the total angular momentum couples spin tunneling in such a molecule to the mechanical twists. We'll focus on Landau-Zener spin transition due to a time-dependent magnetic field and we'll show that these transitions generate a unique pattern of mechanical oscillations that can be detected by measuring the electronic current through the molecule.

6.1 Recent Experiments

6.1.1 Introduction

In the last two decades there has been a great interest in the field of spintronics. Spintronic systems make use of the fact that the electron current is composed of spin-up and spin-down carriers which carry information encoded in their spin state. In a closely related field, molecular spintronics is emerging, which combines the ideas of spintronics and molecular electronics. There is a strong interest in designing molecular devices using a few magnetic molecules. Single molecule magnets are a candidate for that purpose: they have a long relaxation times at temperatures lower than 3 K. To this end, a significant experimental effort has been developed to measure the electronic current through a single molecule bridged between conducting leads. The properties of single molecule magnets (such as Mn_{12}-acetate) have been outlined in the first two chapters of this thesis.

In most experiments, a magnetic molecule was attached between two non-magnetic tips, see figure 6.1 for example [103].

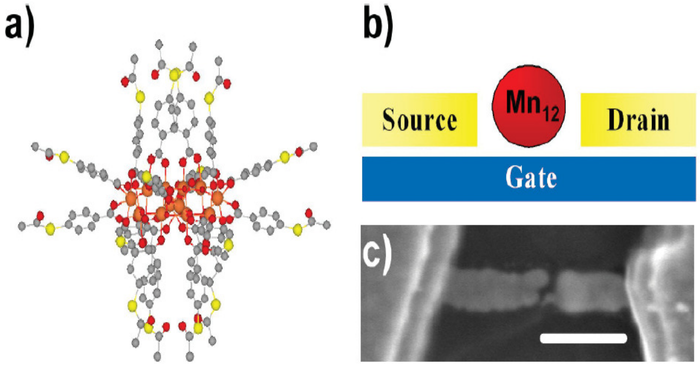

Figure 6.1: (a) Side view of a Mn_{12} molecule with tailormade ligands containing acetyl-protected thiol end groups. Atoms are color labeled: manganese (orange), oxygen (dark red), carbon (gray), sulfur (yellow). The molecule diameter is about 3 nm. (b) Schematic drawing of the Mn12 molecule (red circle) trapped between electrodes. A gate changes the electrostatic potential on the molecule enabling energy spectroscopy. (c) Scanning electron microscopy image of the electrodes [103].

The device pictured in 6.1 is called a three-terminal transport device or a molecular spin-transistor. The current passes through the magnetic molecule through the source and drain electrodes and the electronic transport properties are tuned using a gate voltage V_g. Two experimental regimes are distinguished and they are the subject of various research papers: when the coupling between the electrodes and the molecule is weak (the weak coupling limit) and when the coupling between the electrodes and the molecule is strong. We will briefly describe each of the coupling limits next.

6.1.2 The Weak and the Strong Coupling Limit

In the weak coupling limit, Heersche et al. observed striking voltage dependence of the current through a single-molecule magnet Mn_{12}, with a complete current suppression and excitations of negative differential conductance on the energy scale of the anisotropy barrier [103]. Jo et al. measured the magnetic field dependence of the electron tunneling spectrum in a transistor incorporating a Mn_{12} molecule [104]. Henderson et al. observed a Coulomb blockade effect by measuring conductance through a single-molecule magnet Mn_{12} [105]. Voss et al. conducted experiments and developed theoretical model for the dependence of the tunneling current on the orientation of the Mn_{12} molecule [106]. In the cases mentioned above, the experiment was done using Mn_{12} molecules where the acetate of the molecule has been substituted by a thiol-containing ligands which bind the single molecule magnet to the gold electrodes with strong and reliable covalent bonds.

In the strong coupling limit, paramagnetic molecules containing one or two magnetic centers have been used but not molecular magnets [107]. In references [99, 100, 101, 102], a simple molecule containing two magnetic centers was used. The molecule was tuned using V_g into two different charged states. The neutral state, due to antiferromagnetic coupling between the two magnetic centers, has S=0, whereas the positively charged state has S=1/2. Kondo features are found, as expected, only for the state in which the molecule has a non-zero spin moment. This nicely demonstrates that magnetic molecules with multiple centers and antiferromagnetic interactions enable the Kondo effect to be switched on and off, depending on their charge state. Theoretical investigations have explored various aspects of the field.

The effect of the exchange coupling between spins of conducting electrons and the spin of the Mn_{12} molecule has been studied by G.-H. Kim and T.-S. Kim [108]. Elste and Timm [109] developed a model for the Coulomb blockade in a transport through a single magnetic molecule weakly coupled to magnetic and nonmagnetic leads. They also studied the possibility of writing, storing, and reading spin information in memory devices based upon single-molecule magnets [110]. Kondo effect in transport through a single-molecule magnet strongly coupled to metallic electrodes has been investigated by Romeike et al [111]. The effect of spin Berry phase on electron tunneling has been studied by González and Leuenberger [112]. Misiorny et al. investigated magnetic switching of the molecular spin by a spin-polarized current [113], as well as tunneling magnetoresistance [114]. Cornaglia et al. have studied the effect on the transport of a soft vibrating mode of the molecule [115]. First principle DFT calculations of the electron transport through a Mn_{12} single-molecule magnet and of spin-filtering effect have been performed by Barraza-Lopez et al. [116]. There also has been some effort to compute Josephson current through a magnetic molecule coupled to superconducting leads [117].

6.2 Rotational Dynamics of the Molecule

Recently Chudnovsky and Garanin have demonstrated [118] that quantum states of a magnetic molecule that is free to rotate are different from quantum states of a magnetic molecule whose position is fixed in a crystal. This effect arises from the conservation of the total angular momentum (spin + orbital). Somewhat intermediate situation occurs when a molecule is bridged between two electrodes. While such a molecule is not free to rotate, its orientation can still vary due to the spin-rotation coupling. In our work we studied the Landau-Zener transition between quantum states of the molecule caused by a field sweep. We showed that coupled dynamics of the molecular spin and the mechanical rotation of the molecule leads to the modification of the Landau-Zener dynamics. It also results in a specific pattern of mechanical oscillations of the molecule. Since electron tunneling through the molecule should strongly depend on its orientation, this effect should be seen in the tunneling current [119].

We consider geometry depicted in Fig. 6.2. The magnetic anisotropy axis of the molecule, Z, is perpendicular to the direction of the transport current Y. The mechanical motion of the molecule is restricted by its coupling to the leads. For simplicity we consider only small torsional oscillations about the Z-axis that we describe by the angle of rotation ϕ. This is justified by the fact that quantum tunneling of the molecular spin between two opposite directions along the Z-axis changes only the Z-component of the angular momentum, thus generating the Z-component of the torque. In our approximation, small rotation of the molecule due to this torque produces negligible deformation of a rigid magnetic core of the molecule. On the contrary, the tunneling current through the molecule must have exponential dependence on ϕ. We assume that electrons in the leads have only marginal effect on the quantum spin states of the molecule.

The main part of the Hamiltonian of the molecule has three terms:

$$\hat{H} = \hat{H}_{rot} + \hat{H}_Z + \hat{H}_S \,. \tag{6.1}$$

Here

$$\hat{H}_{rot} = \frac{1}{2I_z}\left(\hbar^2 L_z^2 + I_z^2 \omega_r^2 \phi^2\right) \tag{6.2}$$

describes mechanical rotations about the Z-axis. I_z is the corresponding moment of inertia and ω_r is the frequency of free torsional oscillations of the molecule due its coupling to the leads. Operator of the mechanical angular momentum, $L_z = -i\partial/\partial\phi$, satisfies the commutation relation

$$[\phi, L_z] = i. \tag{6.3}$$

Interaction of the molecular spin $\mathbf{S}$ with the external magnetic field, $\mathbf{B}$ applied along

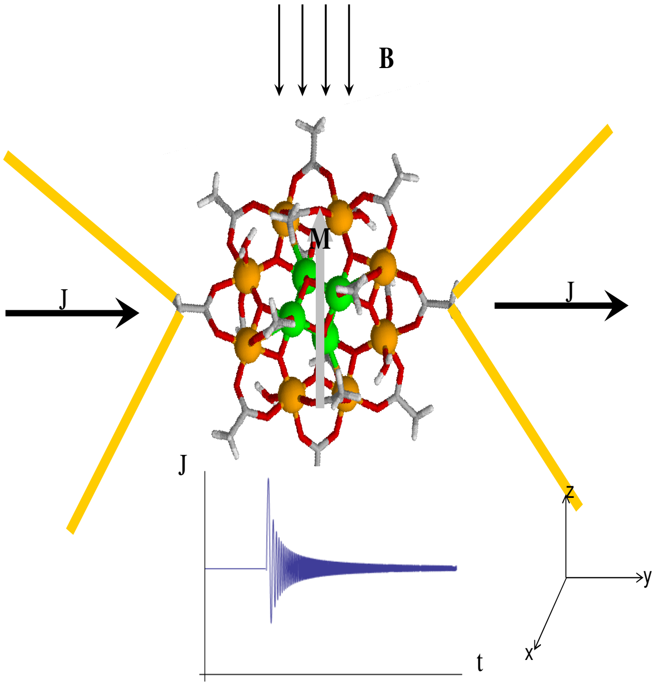

Figure 6.2: Mn_{12} spin-10 magnetic molecule bridged between metallic leads [116].

the Z-axis, is described by the Zeeman term in Eq. (6.1):

$$\hat{H}_Z = -g\mu_B S_z B_z \,, \tag{6.4}$$

with g being the gyromagnetic factor and μ_B being the Bohr magneton. Operator $\hat{H}_S$ in Eq. (6.1) is given by [84, 94]

$$\hat{H}_S = \hat{R}\hat{H}_A\hat{R}^{-1} \,, \tag{6.5}$$

where $\hat{H}_A$ is the crystal-field (magnetic anisotropy) spin Hamiltonian and

$$\hat{R} = e^{-iS_z\phi} \tag{6.6}$$

is the operator of rotation in the spin space. The general form of $\hat{H}_A$ is

$$\hat{H}_A = \hat{H}_\| + \hat{H}_\perp \,, \tag{6.7}$$

where $\hat{H}_{\|}$ commutes with S_z and $\hat{H}_{\perp}$ is a perturbation that does not commute with S_z. The existence of the magnetic anisotropy axis Z means that the $|\pm S\rangle$ eigenstates of S_z are degenerate ground states of $\hat{H}_{\|}$. Operator $\hat{H}_{\perp}$ slightly perturbs the $|\pm S\rangle$ states, adding to them small contributions of other $|m_S\rangle$ states. We shall call these degenerate normalized perturbed states $|\psi_{\pm S}\rangle$. Physically they describe the magnetic moment of the molecule looking in one of the two directions along the anisotropy axis. Full perturbation theory with account of the degeneracy of $\hat{H}_A$ provides quantum tunneling between the $|\psi_{\pm S}\rangle$ states. The ground state and the first excited state become

$$\Psi_{\pm} = \frac{1}{\sqrt{2}}\left(|\psi_S\rangle \pm |\psi_{-S}\rangle\right) . \tag{6.8}$$

They satisfy

$$\hat{H}_A\Psi_{\pm} = E_{\pm}\Psi_{\pm} \tag{6.9}$$

with $E_- - E_+ \equiv \Delta$ being the tunnel splitting. Expressing $|\psi_{\pm S}\rangle$ via $\Psi_{\pm}$ according to Eq. (6.8), it is easy to see from Eq. (6.9) that

$$\langle\psi_{\pm S}|\hat{H}_A|\psi_{\pm S}\rangle = 0, \quad \langle\psi_{-S}|\hat{H}_A|\psi_S\rangle = -\Delta/2\,. \tag{6.10}$$

This gives

$$\langle\psi_{\pm S}|\hat{H}_S|\psi_{\pm S}\rangle = 0, \quad \langle\psi_{\mp S}|\hat{H}_S|\psi_{\pm S}\rangle = -\frac{\Delta}{2}e^{\pm 2iS\phi}\,. \tag{6.11}$$

for the matrix elements of $\hat{H}_S$.

Since the low-energy spin states of the molecule are superpositions of $|\psi_{\pm S}\rangle$, it is convenient to describe such a two-state system by a pseudospin 1/2. Components of the corresponding Pauli operator $\boldsymbol{\sigma}$ are

$$\begin{aligned} \sigma_x &= |\psi_{-S}\rangle\langle\psi_S| + |\psi_S\rangle\langle\psi_{-S}| \\ \sigma_y &= i|\psi_{-S}\rangle\langle\psi_S| - i|\psi_S\rangle\langle\psi_{-S}| \\ \sigma_z &= |\psi_S\rangle\langle\psi_S| - |\psi_{-S}\rangle\langle\psi_{-S}|\,. \end{aligned} \tag{6.12}$$

The projection of any operator $\hat{H}$ onto $|\psi_{\pm S}\rangle$ states is given by

$$\sum_{m,n=\pm S}\langle\psi_m|\hat{H}|\psi_n\rangle|\psi_m\rangle\langle\psi_n|\,. \tag{6.13}$$

Noticing that

$$S_z|\psi_{\pm S}\rangle \cong S_z|\pm S\rangle = \pm S|\psi_{\pm S}\rangle\,, \tag{6.14}$$

it is easy to project Hamiltonian (6.1) onto $\psi_{\pm S}$.

The projection of $e^{-iS_z\phi}\hat{H}_A e^{iS_z\phi}$ on the two-state basis is

$$\begin{aligned}
&\left\langle \psi_{-S}\left| e^{-iS_z\phi}\hat{H}_A e^{iS_z\phi}\right| \psi_S\right\rangle |\psi_{-S}\rangle\langle\psi_S| + \left\langle \psi_S\left| e^{-iS_z\phi}\hat{H}_A e^{iS_z\phi}\right| \psi_{-S}\right\rangle |\psi_S\rangle\langle\psi_{-S}| \\
=\;& -\frac{1}{2}\Delta\left(e^{2iS\phi}|\psi_{-S}\rangle\langle\psi_S| + e^{-2iS\phi}|\psi_S\rangle\langle\psi_{-S}|\right) \\
=\;& -\frac{1}{2}\Delta\cos(2S\phi)\left(|\psi_{-S}\rangle\langle\psi_S| + |\psi_S\rangle\langle\psi_{-S}|\right) - \frac{1}{2}\Delta\sin(2S\phi)\, i\left(|\psi_{-S}\rangle\langle\psi_S| - |\psi_S\rangle\langle\psi_{-S}|\right) \\
=\;& -\frac{1}{2}\Delta\cos(2S\phi)\,\sigma_x - \frac{1}{2}\Delta\sin(2S\phi)\,\sigma_y.
\end{aligned} \tag{6.15}$$

One can see that the full effective Hamiltonian has the form

$$\hat{H}_{\text{eff}} = -\frac{1}{2}W\sigma_z - \frac{1}{2}\Delta\left[\cos(2S\phi)\,\sigma_x + \sin(2S\phi)\,\sigma_y\right] + \hat{H}_{\text{rot}} \tag{6.16}$$

or

$$\hat{H}_{\text{eff}} = -\frac{1}{2}\mathbf{H}_{\text{eff}}\cdot\sigma + \hat{H}_{\text{rot}}, \tag{6.17}$$

where

$$\mathbf{H}_{\text{eff}} = W\mathbf{e}_z + \Delta\cos(2S\phi)\,\mathbf{e}_x + \Delta\sin(2S\phi)\,\mathbf{e}_y. \tag{6.18}$$

and

$$W = 2Sg\mu_B B_z\,. \tag{6.19}$$

Note that for a non-rotating magnetic molecule the effective Hamiltonian has the form

$$\hat{H}_{\text{eff}} = -\frac{1}{2}W\sigma_z - \frac{1}{2}\Delta\sigma_x\,. \tag{6.20}$$

Its eigenvalues are

$$E_\pm = \pm\frac{1}{2}\sqrt{W^2+\Delta^2} \tag{6.21}$$

with

$$E_+ - E_- \equiv \hbar\omega_0 \equiv \sqrt{W^2+\Delta^2}\,. \tag{6.22}$$

Using the Heisenberg equation of motion for an operator $A(t)$,

$$\dot{A}(t) = \frac{i}{\hbar}\left[\hat{H}_{\text{eff}}, A(t)\right] , \tag{6.23}$$

one obtains

$$\dot{\phi} = \frac{i}{\hbar}\left[\frac{\hbar^2 L_z^2}{2I_z}, \phi\right] = \frac{i\hbar}{2I_z}\left(L_z\left[L_z, \phi\right] + \left[L_z, \phi\right]L_z\right) = \frac{\hbar L_z}{I_z} \tag{6.24}$$

and

$$\hbar\dot{L}_z = i[\frac{1}{2}I_z\omega_r^2\phi^2 - \frac{1}{2}\Delta\left[\cos 2S\phi\sigma_x + \sin 2S\phi\sigma_y\right], L_z] = -I_z\omega_r^2\phi - S\Delta\sin(2S\phi)\sigma_x + S\Delta\cos(2S\phi)\sigma_y$$

Elimination of L_z provides the following system of equations:

$$\hbar\dot{\sigma}_x = W\sigma_y - \Delta\sin(\varphi)\sigma_z \tag{6.25}$$

$$\hbar\dot{\sigma}_y = \Delta\cos(\varphi)\sigma_z - W\sigma_x \tag{6.26}$$

$$\hbar\dot{\sigma}_z = \Delta\sin(\varphi)\sigma_x - \Delta\cos(\varphi)\sigma_y \tag{6.27}$$

and

$$\ddot{\varphi} + \omega_r^2\varphi = \omega_c^2\left[\cos(\varphi)\sigma_y - \sin(\varphi)\sigma_x\right] . \tag{6.28}$$

Here

$$\varphi \equiv 2S\phi \tag{6.29}$$

and

$$\omega_c \equiv \sqrt{2S^2\Delta/I_z} . \tag{6.30}$$

Combining the above equations it is easy to see that they satisfy

$$\frac{d}{dt}(\hbar L_z + \hbar S\sigma_z) = -I_z\omega_r^2\phi . \tag{6.31}$$

The left-hand side of this equation is the time derivative of the Z-component of the total angular momentum, $\hbar(L_z + S_z)$, while the right-hand side is the elastic torque due to the coupling to the leads (see Fig. 6.2). This torque acts such as to return the molecule to its equilibrium position, $\phi = 0$. In the absence of such a torque the total angular momentum of the molecule alone would be conserved.

Equations (6.25) - (6.28) are operator equations. To obtain numerically tractable equations, these operator equations should be averaged over quantum states of the system. If one decouples the quantum averages as

$$\langle \sin(\varphi)\,\sigma_z \rangle \Rightarrow \langle \sin(\varphi) \rangle \langle \sigma_z \rangle \ , \tag{6.32}$$

in the spirit of the mean-field approximation, one obtains classical-like equations of the same structure as above. Without such a decoupling the equations for the Heisenberg operators are useless and one has to go back to the Schrödinger equation for the whole system consisting of coupled spin and mechanical subsystems. While the decoupling cannot be justified in the general case, we notice that the cross terms containing $\boldsymbol{\sigma}$ and ϕ become small when $\langle \varphi \rangle$ is small. Since $\varphi = 2S\phi$ this condition for large S is stronger than the condition of small oscillations, $|\phi| \ll 1$. Nevertheless, even for $S = 10$, which is the case of a Mn_{12} molecule, it is likely that rotations of the molecule in the geometry depicted in Fig. 6.2 will still satisfy the condition $|\varphi| \ll 1$. In this case Eqs. (6.25) - (6.28) can be treated as classical.

6.3 Landau-Zener Effects in a Magnetic Molecule Bridged Between two Conducting Leads

6.3.1 Landau-Zener Dynamics

The behavior of the system depends on the dimensionless magneto-mechanical constant of a free molecule,

$$\delta \equiv \left(\frac{\hbar\omega_c}{\Delta} \right)^2 = \frac{2\hbar^2 S^2}{I_z \Delta} \,, \tag{6.33}$$

and the resonance parameter,

$$r \equiv \frac{\hbar\omega_r}{\Delta} \,. \tag{6.34}$$

For a linear field sweep, $W = vt$, another relevant dimensionless parameter is

$$\epsilon \equiv \frac{\pi\Delta^2}{2\hbar v} \,. \tag{6.35}$$

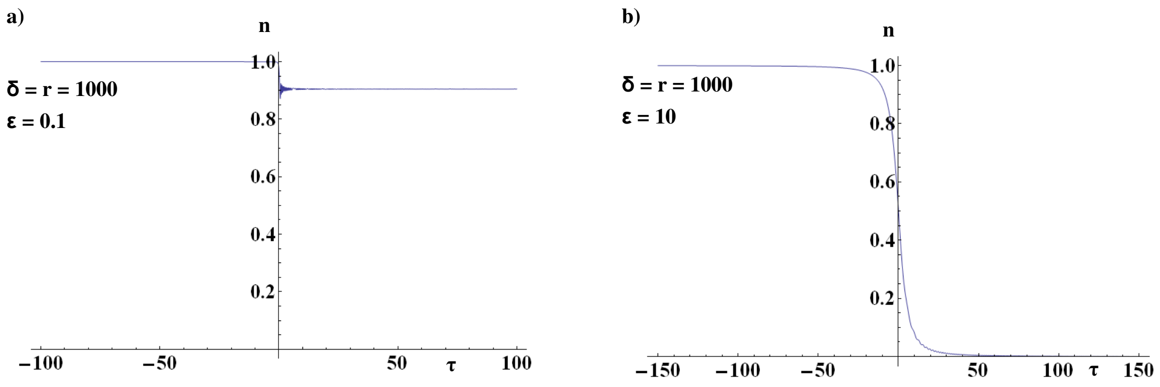

Figure 6.3: The fraction of molecules n that transit to the final state for a) fast sweep, b) slow sweep.

It determines probability,

$$P = e^{-\epsilon}\,, \tag{6.36}$$

of staying in the initial ψ_{-S} state in the standard Landau-Zener problem. Typical plots for the fraction of molecules n that transit to the final state for various sweep is presented in figure 6.3.

Using the above parameters and dimensionless variables

$$\tau \equiv \frac{t\Delta}{\hbar} \quad w = \frac{vt}{\Delta} = \frac{\hbar v \tau}{\Delta^2} = \frac{\pi\tau}{2\epsilon}\,, \tag{6.37}$$

Eqs. (6.25) - (6.28) for $|\varphi| \ll 1$ can be re-written in the form

$$\begin{aligned} \sigma'_x &= w\sigma_y - \varphi\sigma_z \\ \sigma'_y &= \sigma_z - w\sigma_x \\ \sigma'_z &= \varphi\sigma_x - \sigma_y \end{aligned} \tag{6.38}$$

and

$$\varphi'' + \gamma\varphi' + r^2\varphi = \delta\left[\sigma_y - \varphi\sigma_x\right]\,, \tag{6.39}$$

where prime means $d/d\tau$. Notice that in the last equation we introduced a term $\gamma\varphi'$ that describes damping of the mechanical oscillations of the molecule.

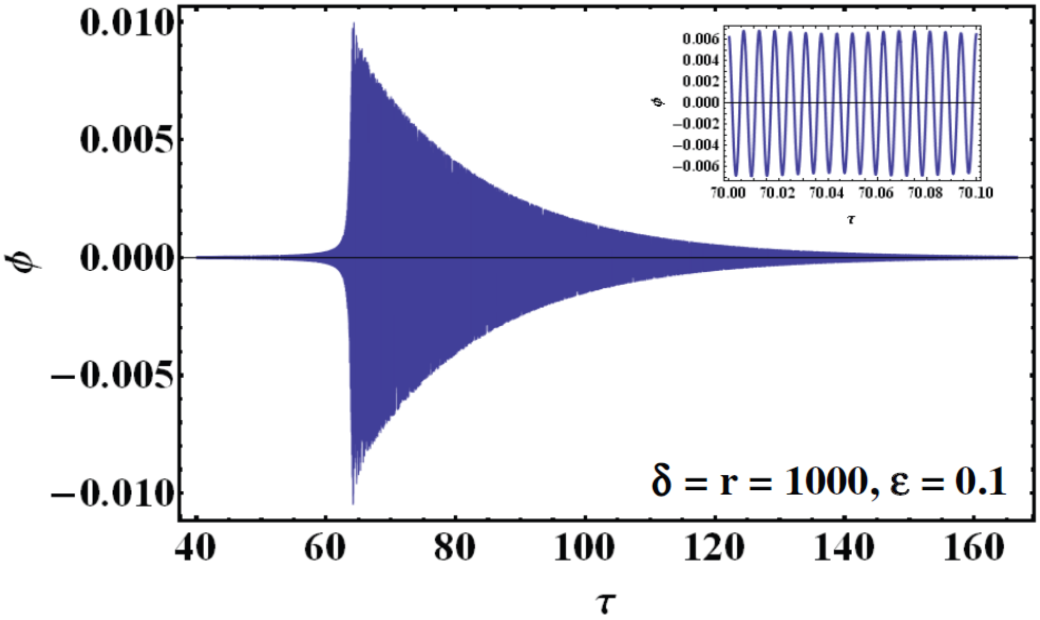

Figure 6.4: Typical time dependence of the rotation angle ϕ. The inset shows the fine structure of the oscillations.

The above equations have been solved numerically using Mathematica. With the Mn_{12} molecule in mind, we compute the time dependence of the angle of twist, $\phi = \varphi/(2S)$, for $S = 10$, $\delta = 10^3$ and $r = 10^3$ (see discussion below). For the illustration purpose, the value of the damping constant $\gamma = 0.1$ has been chosen to provide the finite duration of the oscillations. Fig. 6.4 shows the results for a relatively fast field sweep corresponding to $\epsilon = 0.1$. For a slow sweep ($\epsilon \gg 1$) the amplitude of the oscillations is significantly smaller.

Simple arguments allow one to understand the behavior shown in Fig. 6.4. Oscillations of ϕ are excited when the time-dependent distance between the spin levels given by Eq. (6.22), coincides with the frequency ω_r of the mechanical oscillations of the molecule. For large ϵr this happens at $\tau = 2\epsilon r/\pi$ in excellent agreement with Fig. 6.4, 6.5 and 6.6. Oscillations continue at the frequency ω_r until they are completely damped due to the finite γ. To obtain the dependence of the initial amplitude of oscillations on the parameters the approximate solution of Eqs. (6.38) for $\sigma_y(\tau)$ at small φ, $\epsilon < 1$ and $\tau > 1$ can be used [120]:

$$\sigma_y(\tau) = -2\sqrt{e^{-\epsilon}(1-e^{-\epsilon})}\sin\left(\frac{\pi\tau^2}{4\epsilon}\right). \tag{6.40}$$

This gives an approximate solution of Eq. (6.39) at $\gamma = 0$:

$$\varphi(\tau) = \frac{\delta}{r}\mathrm{Im}\left[e^{ir\tau}\int_0^\tau d\tau' e^{-ir\tau'}\sigma_y(\tau')\right]. \tag{6.41}$$

The result of the integration can be expressed in terms of trigonometric and error functions.

$$\begin{aligned}
\varphi(\tau) \;=\; & \frac{1}{2Sr}C\left[(a_1 + a_2(\tau))\left(Sin\left[r\tau - \frac{r^2\epsilon}{\pi}\right] - Cos\left[r\tau - \frac{r^2\epsilon}{\pi}\right]\right)\right. \\
& +(a_{11} + a_{22}(\tau))\left(\mathrm{Cos}\left[r\tau - \frac{r^2\epsilon}{\pi}\right] + \mathrm{Sin}\left[r\tau - \frac{r^2\epsilon}{\pi}\right]\right) \\
& +(-a_3 + a_4(\tau))\left(\mathrm{Sin}\left[r\tau + \frac{r^2\epsilon}{\pi}\right] + \mathrm{Cos}\left[r\tau + \frac{r^2\epsilon}{\pi}\right]\right) \\
& \left.+\,(a_{44}(\tau) - a_{33})\left(\mathrm{Cos}\left[r\tau + \frac{r^2\epsilon}{\pi}\right] - \mathrm{Sin}\left[r\tau + \frac{r^2\epsilon}{\pi}\right]\right)\right]
\end{aligned} \tag{6.42}$$

where various unknowns in equation 6.42 are given below:

$$\mathrm{C} = \frac{\delta\sqrt{\epsilon}}{\sqrt{2}}\sqrt{e^{-2\epsilon}\left(-1+e^{\epsilon}\right)}, \quad a_1 = \mathrm{Re}\left[\mathrm{Erf}\left[\frac{(1-i)r\sqrt{\epsilon}}{\sqrt{2\pi}}\right]\right], \quad a_{11} = \mathrm{Im}\left[\mathrm{Erf}\left[\frac{(1-i)r\sqrt{\epsilon}}{\sqrt{2\pi}}\right]\right]$$

$$a_2(\tau) = \mathrm{Re}\left[\mathrm{Erf}\left[\frac{\left(\frac{1}{2}-\frac{i}{2}\right)(-2r\epsilon+\pi\tau)}{\sqrt{2\pi}\sqrt{\epsilon}}\right]\right], \quad a_{22}(\tau) = \mathrm{Im}\left[\mathrm{Erf}\left[\frac{\left(\frac{1}{2}-\frac{i}{2}\right)(-2r\epsilon+\pi\tau)}{\sqrt{2\pi}\sqrt{\epsilon}}\right]\right]$$

$$a_3 = \mathrm{Re}\left[\mathrm{Erf}\left[\frac{(1+i)r\sqrt{\epsilon}}{\sqrt{2\pi}}\right]\right], \quad a_{33} = \mathrm{Im}\left[\mathrm{Erf}\left[\frac{(1+i)r\sqrt{\epsilon}}{\sqrt{2\pi}}\right]\right]$$

$$a_4(\tau) = \mathrm{Re}\left[\mathrm{Erf}\left[\frac{(-1)^{1/4}(2r\epsilon + \pi\tau)}{2\sqrt{\pi}\sqrt{\epsilon}}\right]\right], \quad a_{44}(\tau) = \mathrm{Im}\left[\mathrm{Erf}\left[\frac{(-1)^{1/4}(2r\epsilon + \pi\tau)}{2\sqrt{\pi}\sqrt{\epsilon}}\right]\right]$$

Equation 6.42 can be verified by plotting φ obtained from analytical work with the one obtained numerically, as shown in figure 6.5. While the formula is rather cumbersome it provides a simple dependence of the final amplitude of the undamped oscillations on the parameters:

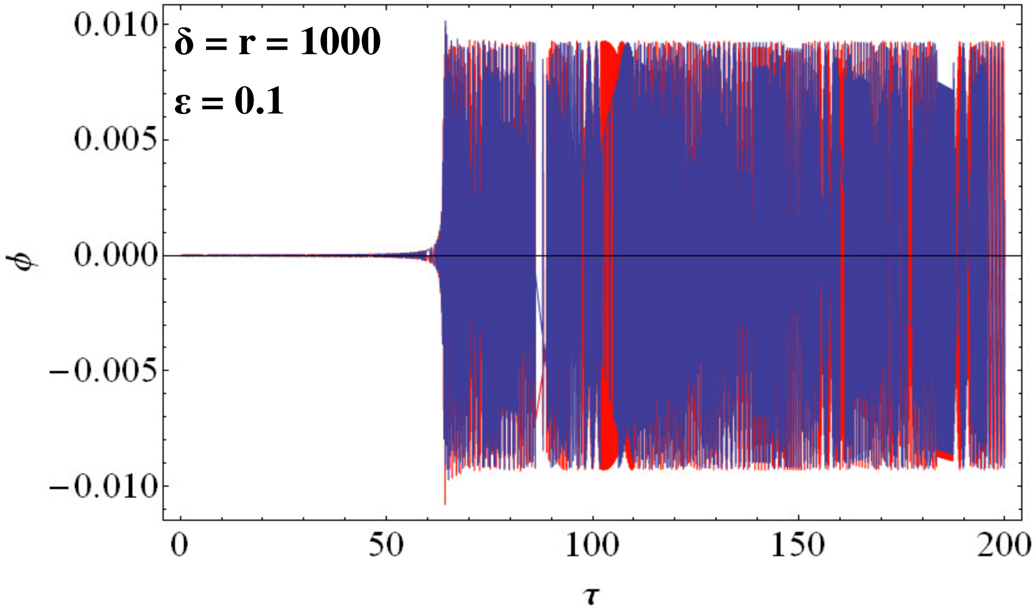

Figure 6.5: The evolution of the angle ϕ when $\delta = r = 1000, \epsilon = 0.1$. The red plot is the result of the analytical solution shown in equation 6.42 whereas the blue one represents the numerical solution for φ.

$$\phi_{max} = \frac{2\hbar S}{I_z\omega_r}\sqrt{\epsilon e^{-\epsilon}\left(1 - e^{-\epsilon}\right)}\,. \tag{6.43}$$

It reaches maximum at $\epsilon = 1.45$. This expression is in excellent agreement with

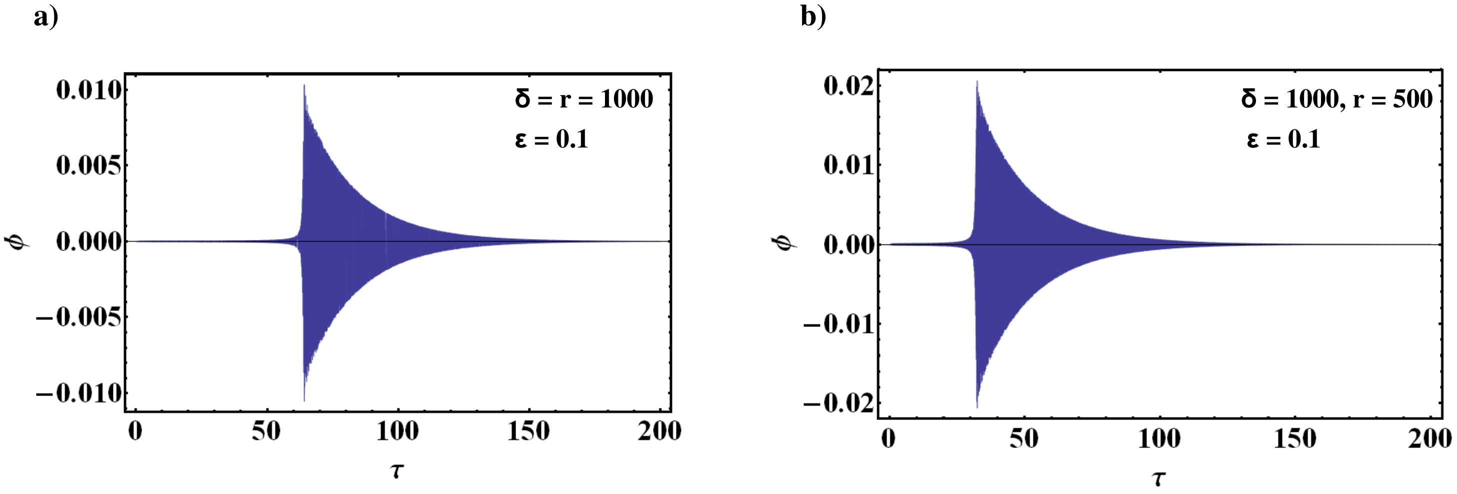

Figure 6.6: The evolution of the angle ϕ when: a) $\delta = r = 1000, \epsilon = 0.1$; b) $\delta = 1000, r = 500, \epsilon = 0.1$.

numerical results. It can be used as long as $2S\phi_{max} \ll 1$.

6.3.2 Conclusion

Most of the existing experiments on transport through individual magnetic molecules have been done with Mn_{12} acetate. The moment of inertia of the Mn_{12} molecule is in the ballpark of 10^{-34}g·cm^2. The tunnel splitting Δ depends strongly on the transverse anisotropy, $\hat{H}_\perp$ in Eq. (6.7). For the molecule bridged between two leads it may differ drastically from that in a Mn_{12} crystal. With $I_z \sim 10^{-34}$g·cm^2 our choice of $\delta \sim 10^3$ in Fig. (6.4) corresponds to $\Delta/\hbar \sim 10^6\mathrm{s}^{-1}$. The resonance frequency of the rotational oscillations of the molecule must be much higher. The choice of $r = 10^3$ in Fig. (6.4) corresponds to $\omega_r = 10^9\mathrm{s}^{-1}$. The mechanical oscillations of the molecule begin at $t = 2\epsilon\hbar^2\omega_r/(\pi\Delta^2)$ or $\tau = \frac{2\epsilon r}{\pi}$ (as demonstrated in figures 6.4, 6.5 and 6.6) after the spin states ψ_{-S} and ψ_S cross due to the field sweep. For the choice of parameters used in Fig. (6.4) this time is of order 10^{-4}s. Spin oscillations given by Eq. (6.40) must dissipate on a longer time scale for the mechanical oscillations to be observable. In a Mn_{12} crystal, dissipation is dominated by phonons. For a setup shown in Fig. 6.2 phonon processes must be suppressed, making spin relaxation times of order 10^{-4}s quite reasonable. For $\Delta/\hbar \sim 10^6\mathrm{s}^{-1}$, the fast field sweep, $\epsilon < 1$, corresponds to a few kOe per second, which is also reasonable. Magnetic molecules other than Mn_{12} acetate may prove to be even better candidates for such an experiment.

If a tunneling current flows through the setup depicted in Fig. 6.2, the amplitude of the current should be affected by the mechanical oscillations of the molecule. Same as in tunneling microscopy, this effect should be detectable due to high sensitivity of the electron tunneling rate to the orientation of the molecule [106]. Following the field sweep, the current should acquire an oscillating component similar to that shown in Fig. 6.4. Such an experiment is practicable and it would be of great interest as it would prob quantum dynamics of spin in individual magnetic molecules.

Part III

Quantum Magnetic Deflagration

Introduction

In this part, we follow up on the work mentioned in chapter 3 of part I of this thesis. Peaks in the deflagration speed versus the external applied magnetic field were observed by Tejada's group in Spain and were attributed to the resonance spin tunneling. I will talk about these quantum features first, then I will mention my work on the experimental determination of the dipolar field in Mn_{12}-acetate followed by the theoretical work of Garanin and Chudnovsky on the low temperature resonant spin tunneling in molecular magnets induced by a field sweep with account of dipole-dipole interactions. The authors have discovered self-organized fronts of tunneling, a non-thermal process triggered by the dipolar field. The aim of my work was to unify the theories of the standard (hot) deflagration and the fronts of tunneling induced by the dipolar field (non-thermal process).

Chapter 7

Recent Experiments

7.1 Quantum Deflagration Maxima

In chapter 3 of this thesis, quantum features of magnetic avalanches were introduced. They were discovered in 2005 by A. Hernández-Mínguez el al. [71]. In figure 3.5, peaks in the speed of the deflagration fronts versus the field were an indication of "quantum" magnetic deflagration: the speed of the avalanche is enhanced at those particular values of the field for which the peaks occur. In that case, the anisotropy barrier is effectively lowered by quantum tunneling of the spins. The velocity maxima were attributed to thermally-assisted quantum deflagration. Those peaks have been confirmed by the theory of Garanin and Chudnovsky see Fig. 3.6, [70]. A follow-up investigation that I was a part of in 2007 confirmed the existence of maxima in the velocity of propagation. This work is detailed next [121]. In that experiment, magnetic avalanches were triggered using a wire heater in a fixed magnetic field applied along the easy axis of single crystals of Mn_{12}-acetate. Fast local measurements of the temperature and time-resolved measurements of the local magnetization as a function of the magnetic field were reported. The measurements were performed on single crystals of Mn_{12}-acetate with typical dimensions of 1.5 x 0.3 x 0.3 mm^3 immersed in liquid ^3He at 0.3 K.

It is well known that all crystals of Mn_{12}-ac contain a small amount of a second species of spin S = 10 molecules that have a lower anisotropy barrier of roughly 45K. This minor species is homogeneously distributed in the crystal at typical levels between 5 and 8 % [22, 122]. The presence of the minor species was found to have a significant influence on both the temperature for ignition and the propagation velocity of the avalanches. Consequently, we used the following protocol to quench the effect of the minor species spin relaxation [123]: after fully magnetizing the crystal in the up direction, the field was swept to a value in the opposite (downward) direction that is large enough to flip the minor species downward but small enough that it leaves the major species intact. Bringing the magnetic field back to zero then yields a crystal with the major (spin up) and minor (spin down) species fully magnetized in opposite directions. This allows the magnetic relaxation of minor and major species of Mn_{12}-ac to be studied independently. For samples prepared as described above, we report the behavior of avalanches of the major species where the minor species plays no role, having already relaxed along the direction of the applied field.

Studies of avalanches of the major species were carried out using the following experimental protocol. After preparing the sample as described earlier, the magnetic field was ramped to a preassigned value in a direction opposite to the polarization of the major species, with the sample immersed in liquid ^{3}He at 300 mK. It is important to note that this temperature is well below the blocking temperature of ≈ 3 K so that below about 2 T, there was negligible reduction of the magnetization by relaxation via tunneling as the field was swept through the resonant fields; the sample thus remained fully magnetized. The wire heater was then turned on at a fixed magnetic field, and the temperature of the sample was monitored by measuring the resistance of the Ge thermometer using standard four-terminal techniques.

Figure 7.1 shows the threshold temperature required to ignite avalanches plotted as a function of the magnetic field for fixed fields between 0.4 and 2.0 T. Sharp dips in the ignition temperature occur at magnetic fields denoted by vertical lines. These magnetic fields correspond to thermally assisted spin tunneling across the anisotropy barrier in Mn_{12}-ac,[24, 64, 35] effectively reducing the anisotropy barrier.

Garanin and Chudnovsky have recently provided a detailed theoretical foundation for the newly discovered process of magnetic deflagration by extending many of the results from the classical theory of combustion to the process of spin reversal in molecular magnets [70]. Consistent with the data shown in Fig. 7.1, their theory predicts a significant drop in the threshold temperature required to trigger avalanches at the resonant values of magnetic field where the barrier against spin reversal is effectively reduced due to resonant quantum spin tunneling.

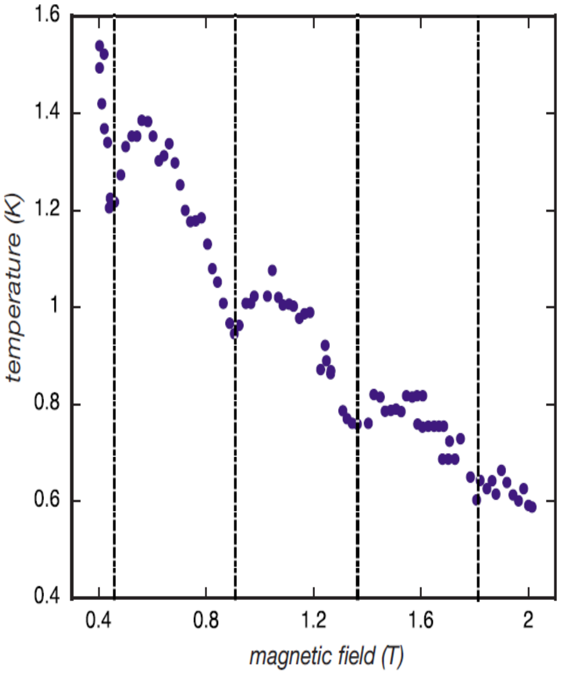

Figure 7.1: Temperature required to ignite avalanches plotted as a function of magnetic field. All data were taken for field-cooled samples. The vertical lines denote the magnetic fields where sharp minima occur in the ignition temperature corresponding to thermally assisted tunneling near the top of the anisotropy barrier [64, 35]. The overall decrease in ignition temperature is due to the reduction of the anisotropy barrier as the field is increased.

In separate experimental runs, time resolved magnetization measurements of the local magnetization obtained for similar Mn_{12}-ac crystals were obtained. The velocity of avalanches was shown in Fig. 7.2 where the filled circles denote results for avalanches that entail the reversal of the full magnetization from one direction to the other along the c-axis, and the open circles are for zero-field-cooled samples where the magnetization changes by half the amount, from zero to full magnetization. The ignition temperatures shown in Fig. 7.1 are also plotted as triangles for comparison. The vertical lines drawn in Fig. 7.2 denote the magnetic fields at which minima occur in the ignition temperature and maxima occur for the velocity.

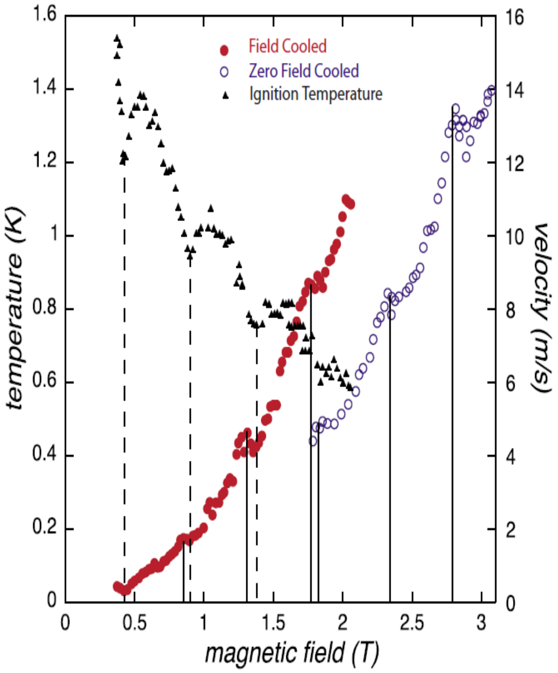

Figure 7.2: Velocity of propagation of avalanches (right-hand yaxis) for field-cooled (filled circles) and zero-field-cooled (open circles) samples versus magnetic field at which avalanche was triggered. The triangles show the ignition temperature (lefthand y-axis). The solid vertical lines drawn from the bottom denote velocity maxima; the dashed vertical lines drawn from the top denote ignition temperature minima. The overall increase of the velocity with increasing magnetic field is due to the decrease of the anisotropy barrier.

The velocity of propagation increases as the field is raised and the barrier due to spin reversal is reduced. From measurements at $\approx$ 2.1 K, Hernandez-Minguez et al.[71] have reported maxima at 0.9 T and 1.35 T, (see 3.5) in agreement with predictions of the theory of Garanin and Chudnovsky [70]. Although maxima are barely discernible at low magnetic fields at the lower (initial) temperatures of our experiments, they become evident at higher magnetic fields. To summarize, using fast local measurements of the temperature and time-resolved measurements of the local magnetization, we have shown that quantum tunneling of the magnetization plays a significant role in determining the threshold temperature for the ignition as well as the propagation of avalanches, as predicted by Garanin and Chudnovsky [70].

In conclusion, using fast local measurements of the temperature and time-resolved measurements of the local magnetization, we have shown that quantum tunneling of the magnetization plays a significant role in determining the threshold temperature for the ignition as well as the propagation of avalanches, as predicted by Garanin and Chudnovsky [70] and confirming the peaks in the speed of propagation of the avalanches as discovered by A. Hernández-Mínguez el al. [71].

7.2 Effect of Dipolar Fields

Recent work on molecular magnet has focused on circumstances where the assumption of independent spins breaks down. Thus, ferromagnetic ordering due to magnetic dipole-dipole interactions has been demonstrated experimentally in high-spin molecular magnets by Morello et al.[124] in Mn_6 by Evangelisti et al.[125] in the high-spin molecular magnet Fe_{17}. Based on neutron scattering experiments, Luis et al.[126] have claimed that Mn_{12}-ac also orders ferromagnetically provided a large transverse field is applied to reduce the magnetic barrier and increase the relaxation rate. In this section we focus on two studies: first I report the results of a direct measurement of the dipolar field obtained by exploiting the properties of the fast-relaxing minor species in crystals of Mn_{12}-ac, a project I was part of. Second, I report on recent detailed calculations by Garanin and Chudnovsky [127] that indicated that dipolar ferromagnetism in a transverse field should indeed be found in Mn_{12}-ac below a Curie temperature $T_c \approx 0.8$ K and the authors' theoretical calculations of the dipolar field in Mn_{12}-ac.

7.2.1 Experimental Determination of the Dipolar Field in Mn_{12}-acetate

It is well known that Mn_{12}-ac crystals contain a small fraction of low-symmetry species molecules at a level of roughly 5% [128]. This minor species, an isomer of the major species of Mn_{12}-ac, has a reduced energy barrier of ≈ 42 K at zero field [129]. The magnetic relaxation rates, typically determined by AC susceptibility measurements, are fit with an Arrhenius equation:

$$\Gamma = \Gamma_0 exp[-U(H)/T] \tag{7.1}$$

For the major species, $\Gamma_0 \approx 4.2 \times 10^7 s^{-1}$ and $\Gamma_0 \approx 4.5 \times 10^9 s^{-1}$ for the fast-relaxing minor species [129].

The different relaxation rates are also evident in magnetization curves. Figure 7.3 shows a hysteresis loop for a single crystal of Mn_{12}-ac taken at 0.3 K with an external field sweep rate of ±10 mT/s. Starting from zero field, the total magnetization is constant as the field is increased to 0.90 T. Small steps are observed at ≈ 0.9 T and 1.28 T corresponding to the resonant relaxation of the minor species magnetization. Above 1.5 T, all minor species molecules have reversed and no further change in the total magnetization is seen until ≈ 3 T. Between 3.1 and 5.3 T, evenly space steps are observed due to tunneling of the major species. Above 5.3 T, all the major species molecules have reversed and the crystal is completely magnetized. Using a simple protocol similar to one described in Ref. [130], the difference in the fields required to flip the spins of the major and minor species allows one to magnetically prepare the crystal with:

(A) Minor species are aligned and major species spins are random; This is achieved

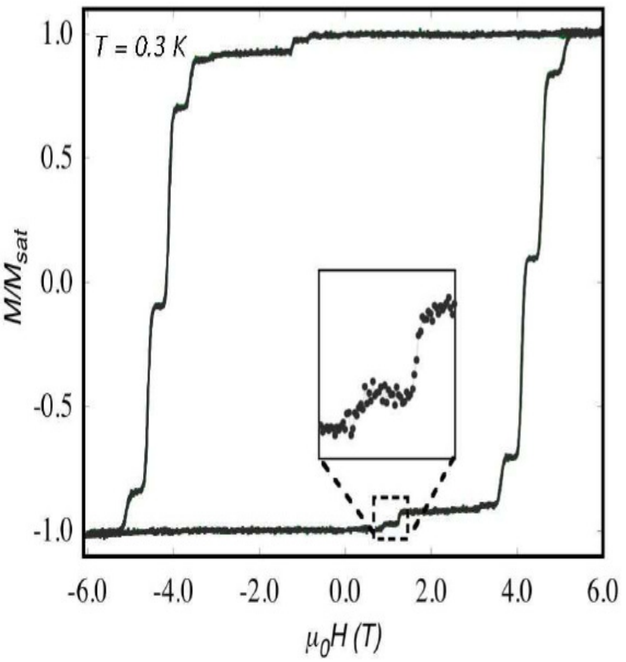

Figure 7.3: Magnetization versus magnetic field of a single crystal of Mn_{12}-ac measured for an external field sweep rate of ±10 mT/s.

using the following protocol: Starting with an unmagnetized (zero-field-cooled) crystal, and maintaining the temperature at 300 mK: a magnetic field of -2 T is applied which is sufficient to completely magnetize the minor species while leaving the major species spins unchanged; sweeping the field back to zero yields a sample with minor species spins aligned and major species spins random with zero net magnetization.
(B) Major and minor species spins are aligned in the same direction; This is achieved by applying a larger magnetic field of -6.0 T is applied along the c-axis of the crystal, sufficient to magnetize both species; reducing the magnetic field to zero yields a sample with major species and minor species spins aligned in the same direction.
(C) Major and minor species spins are aligned in opposite directions. This magnetic preparation is described schematically in Figure 7.4. Starting with the spins aligned

in same direction (Fig. 7.4(a)), the magnetic field is ramped to -2 T in the direction opposite to the magnetization, reversing the direction of the minor species spins while leaving the major species spins unchanged, as shown in (Fig. 7.4(b)). Reducing the field back to zero, (Fig. 7.4(c)), yields a sample in which the minor and major species are magnetized in opposite directions.

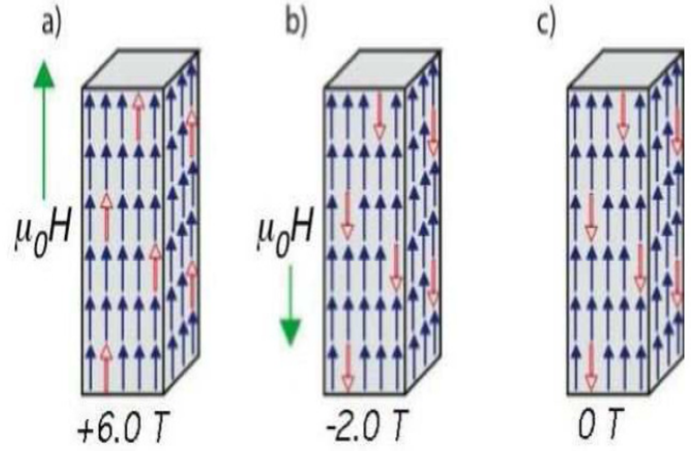

Figure 7.4: Procedure used to prepare Mn_{12}-ac with minor and major species magnetized in opposite directions. (a) First, a +6 T field is applied to align all spins. (b) Then, a -2 T field is applied, reversing the magnetization of the minor species. (c) Finally, the field is returned to zero, leaving the major and minor species spins anti-parallel.

With the sample prepared according to these three methods, the hysteresis loop of the minor species was measured by sweeping the magnetic field between +2 and -2 T, taking care not to reach fields large enough to reverse the spins of the major species. The magnetization was measured using an array of micron-sized Hall sensors for single crystal of Mn_{12}-ac with typical dimensions of 1.0 x 0.3 x 0.3 mm^3 immersed in ^{3}He.

Fig. 7.5 (a) shows hysteresis curves for the minor species taken at 0.3 K and an external field sweep rate of 5 mT/s for the three different magnetic preparations. The curves are normalized by M_{sat}, the saturation value of the minor species. The minor species hysteresis curves exhibit a similar staircase structure as the major species. However, the smaller anisotropy leads to a smaller spacing between steps. Fig. 7.5 (b) shows the derivative of the magnetization curve, which is useful for determining the location and widths of the tunneling resonances. It is clear that the externally applied magnetic field corresponding to the tunneling resonances depends on the direction of the magnetization of the major species. The circles of Fig. 7.5 are data taken with the net magnetization of the major species equal to zero. Fully magnetizing the major species in the positive direction shifts the location of the tunneling resonance fields by ≈ 0.05 T, as indicated by the triangles. Here the dipolar field adds to the external field to satisfy the resonance condition. The squares are data taken with the major species magnetized fully in the negative direction with a consequent shift in the resonance field of ≈ 0.05 T. In this case, the external field is larger to offset the dipolar field in the opposite direction. A close determination of the shift corresponding to the dipolar field associated with full magnetization of the major species of Mn_{12}-ac yields 51.5 ± 8.5 mT.

The dipolar fields of a completely magnetized crystal of Mn_{12}-ac was calculated in [127] and was found to be 52.6 mT, in excellent agreement with our data. These calculations as well as the existence of dipolar ferromagnetism in Mn_{12}-ac are discussed next.

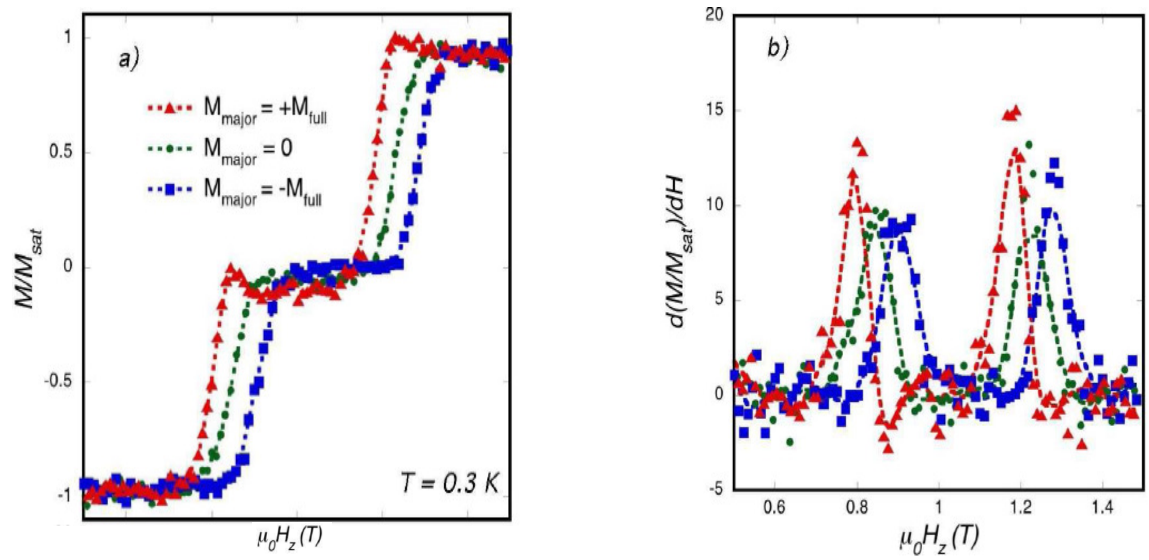

Figure 7.5: (a) Magnetization of the minor species as a function of external magnetic field swept at +5 mT/s with the major species magnetization prepared following the three protocols described in the text. The triangles (squares) are data taken with the major species aligned in the positive (negative) direction. The circles are data taken with the minor species randomly oriented to yield zero magnetization. (b) The derivative of the curves shown in frame (a).

7.2.2 Theoretical Calculations of the Dipolar Field

Theoretical calculations of the dipolar field were performed by Garanin and Chudnovsky [127]. In that work, the authors found that dipolar interactions favor ferromagnetic ordering of elongated crystals of Mn_{12}-acetate below 0.8 K. Ordered crystals must possess domain walls, and it was proved that the motion of the wall corresponds to a moving front of Landau-Zener transitions between quantum spin levels. The authors accounted for local spin transitions and long range dynamics of the dipolar field to study relaxation in molecular magnets: the change in the spin state of one molecule results in the change in the long range dipolar field.

Quantum tunneling was considered between two nearly degenerate ground states of magnetic molecules at low temperature interacting with each other as magnetic dipoles. The molecules are then effectively described by spin 1/2 instead of spin 10. In the absence of Quantum tunneling between states $|\pm S\rangle$, these states do not communicate with each other so that any initial distribution of molecules in spin up and spin down states will be preserved. The measure of communication between $|\pm S\rangle$ states is the tunnel splitting Δ. Ferromagnetic ordering and motion of domain walls can be observed only if Δ is sufficiently large. In Mn_{12}-acetate, it can be controlled by the transverse magnetic field. The authors chose an elongated sample of the shape of a long cylinder of length L and radius R, the quantization axis of spins being directed along the z axis of the cylinder and ignored inhomogeneities along the perpendicular axes x and y and σ_z depends on z only.

The effective Hamiltonian of one magnetic molecule taking into account only the two ground states $|\pm S\rangle$ of a molecular magnet at low temperature can be formulated in terms of pseudospin $\hat{\sigma}$

$$\hat{H}_{eff} = -\frac{1}{2}W\hat{\sigma}_z - \frac{1}{2}\Delta\hat{\sigma}_x \tag{7.2}$$

Here $W = 2Sg\mu_B B_z$ is the energy bias that generally depends on time via the total longitudinal field B_z including the external and dipolar fields. Δ is the tunnel splitting defined by uniaxial anisotropy D and the terms in the Hamiltonian that cause tunneling (like the transverse field), $\hat{\sigma}_z$, $\hat{\sigma}_x$ are Pauli matrices. The energy levels of this Hamiltonian for an instantaneous value of W are:

$$\epsilon_{\pm} = \pm\frac{1}{2}\hbar\omega_0 \quad \hbar\omega_0 = \sqrt{W^2 + \Delta^2}, \tag{7.3}$$

where ω_0 is the corresponding transition frequency.

The energy bias W in the equations above at the site i is given by :

$$W_i = 2Sg\mu_B(Bz + B^D_{i,z}) = W_{ext} + W^D_i \tag{7.4}$$

where B_z is the z component of the external field and $B^D_{i,z}$ is the dipolar field at site i. The dipolar component of the bias is given by:

$$W^D_i = 2E_D\, D_{i,zz} \tag{7.5}$$

where

$$D_{i,zz} = \sum_j \phi_{ij}\sigma_{\mathrm{jz}} \tag{7.6}$$

and

$$E_D = \frac{(g\mu_B S)^2}{v_0} \tag{7.7}$$

is the dipolar energy and v_0 is the unit cell volume and $\phi_{ij} = \frac{3v_0(\mathbf{ez}.\mathbf{n}_{ij})^2-1}{r^3_{ij}}$ and $\mathbf{n}_{ij} = \frac{\mathbf{r}_{ij}}{r_{ij}}$ is the dimensionless dipole-dipole interaction between the spins at sites i and $j \neq i$. The z-component of the dipolar field itself is given by:

$$B^D_{i,z} = \frac{g\mu_B S}{v_0} D_{i,zz}. \tag{7.8}$$

To calculate the dipolar field, one can introduce a macroscopic sphere of radius r_0 satisfying $v_0^{1/3} \ll r_0 \ll L$ around the site i where L is the macroscopic linear size of the sample. The field from the spins at sites j inside the sphere can be calculated by direct summation over the lattice whereas the field from the spins outside the sphere can be obtained by integration. In particular for a uniformly magnetized ellipsoid,one has [127]

$$D_{zz} = \sigma_z \sum_j \phi_{ij} = \overline{D}_{zz}\sigma_z \tag{7.9}$$

independently of i where

$$\overline{D}_{zz} = \overline{D}_{zz}^{sph} + 4\pi\nu\left(1/3 - n^z\right) \tag{7.10}$$

where ν is the number of molecules per unit cell. For the demagnetizing factor one has $n^z = 0, 1/3$, and 1 for a cylinder, sphere, and disk respectively. One obtains $\overline{D}_{zz}{}^{sph} = 0$ or a simple cubic lattice and $\overline{D}_{zz}{}^{sph} < 0$ for a tetragonal lattice with $a = b > c$ and $\overline{D}_{zz}{}^{sph} > 0$ for $a = b < c$ Define $E_0 = \frac{-\overline{D}_{zz}E_D}{2}$ to be the dipolar energy per site.

For Mn$_{12}$-acetate we have S = 10, a = b = 17.319 A, c = 12.388 A so v_0 is 3716 A^3 with 2 molecules per unit cells ν =2. Then $\frac{E_D}{k_B} = 0.0671K$. It was proven that for Mn$_{12}$-ac, $\overline{D}_{zz}^{sph}$ =2.155 that results in $\overline{D}_{zz}^{cyl} = 10.53$ for a cylinder. In that case, Eq. 7.8 yield the dipolar field $B_z^D \approx 0.0526$ T or 52.6 mT very close to the experimental value of 51.5±8.5 mT. For a cylinder magnetized with $\sigma_z = \sigma_z(z)$ the field along the symmetry axis has the form:

$$D_{zz}(z) = \nu \int_{-L/2}^{L/2} \frac{2\pi R^2 \sigma_z(z')}{\left[(z'-z)^2 + R^2\right]^{3/2}} dz' - k\sigma_z(z) \tag{7.11}$$

where $k = 8\pi\nu/3 - \overline{D}_{zz}^{sph} = 4\pi\nu - \overline{D}_{zz}^{cyl} > 0$, k = 14.6 for Mn$_{12}$-acetate. Equation 7.11 will be used in the next chapter when numerical work related to deflagration combined with the effect of the dipolar field is discussed.

In the next chapter we discuss self-organized front of tunneling, a non-thermal effect triggered by the dipolar field, then we investigate its application to the problem of thermal deflagration.

Chapter 8

Theory of Quantum Magnetic Deflagration

In this chapter, we present numerical work on deflagration with quantum and dipolar effects. First, it is necessary to introduce the recent discovery of self-organized fronts of tunneling, a non-thermal process triggered by the dipolar field that can bring the system on or off resonance, then I present details of my numerical work on deflagration.

8.1 Self-Organized Patterns of Macroscopic Quantum Tunneling in Molecular Magnets

Garanin and Chudnovsky recently discovered self-organized patterns of the magnetization when studying low temperature resonant spin tunneling in molecular magnets induced by a field sweep with the account of dipole-dipole interactions [131]. It is well-known that molecular magnets do not show significant exchange interaction because the magnetic core of the molecule is screened by organic ligands. So magnetic molecules remain largely superparamagnetic. Garanin and Chudnovsky have shown, as mentioned in the previous chapter [127], that below 0.8 K molecular magnets can order due to dipole-dipole interaction. One important role of dipole-dipole interaction is that the dipolar field created by the spins is large enough to change the resonance condition for the up and down spins and thus to influence spin tunneling. It is also known that in molecular magnets, the reversal of any individual spin changes the long-range dipolar magnetic field of the entire crystal, which can tune other spins out of resonance as explained below. Fully ordered spins in an elongated Mn_{12} sample create a dipolar field at a molecule that was estimated theoretically [127] and experimentally [121], in a project I was part of, to be ≈ 52 mT. This becomes comparable with the resonance width defined by the tunnel splitting Δ in transverse magnetic fields above 5 T, for the $k = 1$ tunneling resonance. For smaller transverse fields, Δ is much smaller and thus the dipole-dipole interactions can completely block the resonant tunneling. The action of the dipolar field is dynamical and self-consistent since tunneling of spins causes the dipolar field to change, blocking or allowing resonant transitions.

In their work, the authors derived and solved integro-differential equations that govern the self-organized tunneling dynamics of spins coupled by dipolar interactions [131]. The calculations used are similar to the ones outlined in the previous chapter where the dipolar field was calculated. The problem was solved for a long cylindrical sample of length L and radius R such as $R \ll L$. As mentioned in earlier work [70], deflagration is mathematically described by the system of coupled rate equation for the number of particles (magnetic molecules) in the metastable state and the heat conduction equation. Here the effect studied is non-thermal so the heat conduction equation will not be used. Using the expressions of the bias at site i of Wi from section 7.2.2, the authors numerically solve for n_{-S} (the initial population of spins which was magnetized in the $-z$ direction initially) as a function of the time ($t\Gamma_{res}$ in dimensionless units) and of dimensionless spatial variable for Mn_{12}-acetate (see fig. 8.1).

The relaxation rate in the dipolar mechanism of spin tunneling resembles the

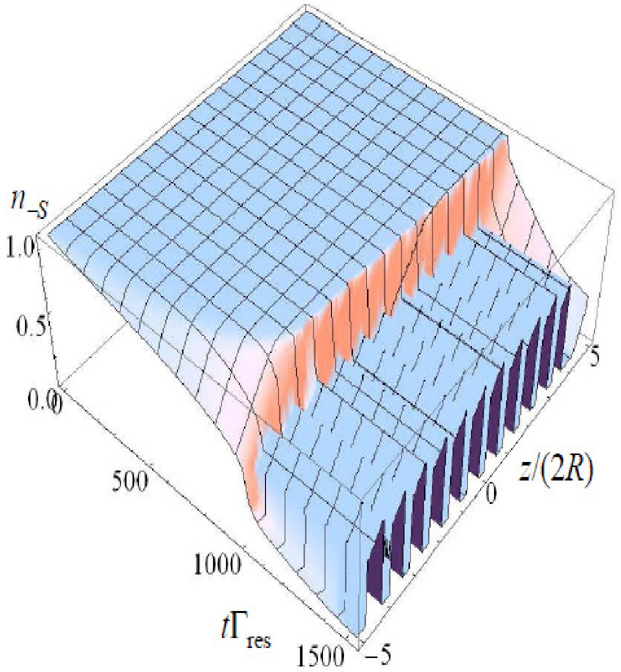

Figure 8.1: Moving wall of resonant spin tunneling induced by a slow sweep, for Mn_{12}-acetate. There are well-developed spatially quasiperiodic, time independent structures behind the wall [131].

magnetic deflagration in Mn_{12}-acetate: however, instead of the temperature, the relaxation rate is controlled by the self-consistent dipolar field bringing the system on or off-resonance. The resulting wall of resonant spin tunneling induced by a slow field sweep is shown in figure 8.1.

8.2 Computation of the Spin Relaxation Rate

Tunneling and relaxation in molecular magnets can be described by the density matrix equation [132] the most comprehensive account of which is given in Ref. [133]. The latter numerically implements the universal spin-phonon interaction suggested in Refs. [134, 135]. This interaction is due to distortionless rotation of the crystal field acting on the spins by transverse phonons and it is completely expressed in terms of the crystal-field Hamiltonian $\hat{H}_A$ without any unknown spin-lattice coupling constants.

As mentioned earlier, experiments in [67, 71] showed the existence of propagating deflagration (burning) fronts in the molecular magnet Mn_{12}-ac that are similar to chemical burning. A. Hernández-Mínguez et al. observed peaks in the deflagration speed on the bias magnetic field B_z that were interpreted as contribution of resonance spin tunneling. This was shown in chapter 3 in Fig. 3.5. A detailed, mainly classical, theory of the magnetic deflagration including the ignition threshold and the accurate prefactor in the Arrhenius-type expression for the speed of the burning front was proposed in Ref. [70] as detailed in chapter 3: in that work quantum effects in magnetic deflagration were taken into account, as a first attempt, by using the Arrhenius relaxation rate that contains the effective barrier lowering at tunneling resonances taken from experiments.

The physics of deflagration is based on the relaxation from a metastable state triggered by the temperature increase and the feedback due to energy release. The burning front forms because the temperature in the regions still unburned (e.g., before the front) rises as the result of heat conduction from the hot areas where burning just occurred. The two main ingredients of deflagration thus are the Arrhenius dependence of the relaxation rate on temperature (making burning in the cold areas before the front negligibly slow) and the heat conduction. Deflagration is mathematically described by the system of coupled i) rate equation for the number of particles (magnetic molecules) in the metastable state and ii) the heat conduction equation.

Subsequent theoretical search for an essentially quantum form of deflagration led to the discovery of self-organized fronts of tunneling, a non-thermal process triggered by the dipolar field (rather than by temperature) that can bring the system on or off resonance [131, 127, 136]. A hallmark of these fronts is the self-consistent adjustment of the metastable population (or magnetization) to the optimal spatial profile

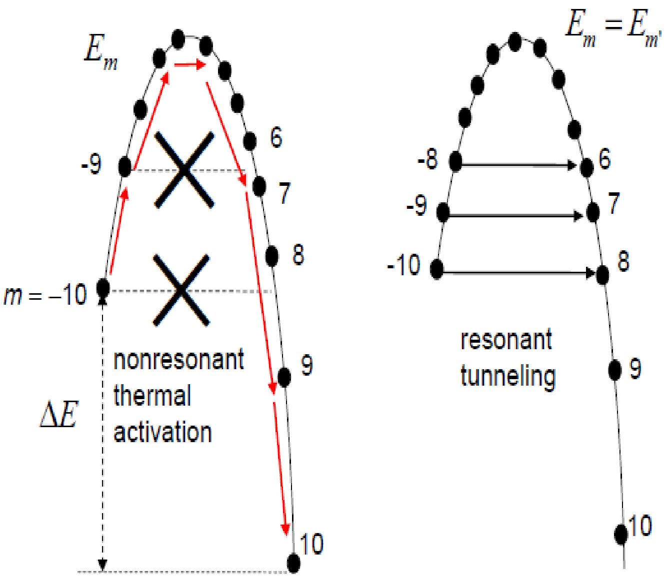

Figure 8.2: Thermal activation in the nonresonant case vs tunneling in the resonant case.

that creates the dipolar field that is constant in some region of space, maintaining the resonance condition (fig. 8.1). The width of the resonance region forming the front core is about the transverse dimension R of the sample that allows an efficient tunneling and thus front propagation. On the other hand, in front and behind the front core the system is off resonance and tunneling is blocked. Fronts of tunneling can be realized in the *dipolar window* of the external field B_z

$$0 \leq B_z - B_k \leq B_z^{(D)} \tag{8.1}$$

Here B_k is the field corresponding to the kth resonance in the absence of the dipolar field and $B_z^{(D)}$ is the dipolar field created by the uniformly magnetized elongated crystal. It was shown [131] that the adjustment mechanism is robust with respect to resonance spread (e.g., due to defects) smaller than $B_z^{(D)}$. There are two regimes of the front propagation: Laminar regime at smaller bias and non-laminar regime at larger bias. In the laminar regime the speed of the front increases with the bias but in the non-laminar regime it decreases with the bias. There is a sharp drop of the front speed at the breakdown of the laminar regime.

The aim of my work was to unify the theories of the standard (hot) deflagration and fronts of tunneling (cold deflagration). The first equation to be used for the fronts of tunneling have been elucidated in chapter 7, see equations 7.8, 7.9, 7.10, 7.11.

We use the generic model of a molecular magnet with $\hat{H}_A = -DS_z^2$, where the tunneling resonance fields are given by

$$B_k = kD/\left(g\mu_B\right), \qquad k = 0, 1, \ldots \tag{8.2}$$

Resonance tunneling occurs at $B_{\mathrm{tot},z} = B_z + B_z^{(D)} \approx B_k$ between the metastable ground state $|-S\rangle$ and an excited state at the other side of the barrier $|m'\rangle$ with $m' = S - k$. At temperatures much smaller than the barrier height (that also includes the temperature of the deflagration front) one can describe magnetic molecules as two-level systems occupying the states $|\pm S\rangle$. Let us denote the probability for a molecule to be in the metastable state $|-S\rangle$ as n. Then the average value of the effective pseudospin σ_z is

$$\sigma_z = 1 - 2n, \tag{8.3}$$

so that $n = 1$ corresponds to $\sigma_z = -1$. The general expression for the longitudinal component of the dipolar field on magnetic molecule i is the sum over positions of all other molecules j

$$B_{i,z}^{(D)} = \frac{Sg\mu_B}{v_0} D_{i,zz}, \qquad D_{i,zz} \equiv \sum_j \phi_{ij}\sigma_{jz}. \tag{8.4}$$

Here v_0 is the unit-cell volume, D_{zz} is the reduced dipolar field, and

$$\phi_{ij} = v_0 \frac{3\left(\mathbf{e}_z \cdot \mathbf{n}_{ij}\right)^2 - 1}{r_{ij}^3}, \qquad \mathbf{n}_{ij} \equiv \frac{\mathbf{r}_{ij}}{r_{ij}}. \tag{8.5}$$

For a long crystal of cylindrical shape of length L and radius R with the symmetry axis z along the easy axis, magnetized with $\sigma_z = \sigma_z(z)$, we will use equations 7.10 for $\bar{D}_{zz}$ and 7.11 for the reduced magnetic field along the symmetry axis D_{zz}.

Now the total field is given by

$$B_{\mathrm{tot},z}(z) = B_z + B_z^{(D)} = B_z + \frac{Sg\mu_B}{v_0} D_{zz}(z). \tag{8.6}$$

One of the dynamical equations of the model is the rate equation

$$\frac{\partial n(t,z)}{\partial t} = -\Gamma\left(B_{\mathrm{tot},z}(z), T(z)\right)\left[n(t,z) - n^{(\mathrm{eq})}(T)\right] \tag{8.7}$$

for the metastable population $n(z)$. In Eq. (8.7), $\Gamma(B_z, T)$ is the relaxation rate taking into account both thermal activation over the barrier and resonance spin tunneling that is calculated from the density matrix equation. In the next section, I will show some plots for $\Gamma(B_z, T)$ as a function of the field and temperature. As $B_{\mathrm{tot},z}$ depends on $n(z)$ everywhere in the sample via Eqs. (7.11) and (8.3), this is an integro-differential equation. We will set $n^{(\mathrm{eq})} \Rightarrow 0$ which is a good approximation for strong enough bias [132].

The second equation is the heat conduction equation that is convenient to write in terms of the energy $\mathcal{E}$ of the system per unit cell. In the full-burning case $n^{(\mathrm{eq})} = 0$ this equation has the form

$$\frac{\partial \mathcal{E}(t,z)}{\partial t} = \frac{\partial}{\partial z}\kappa \frac{\partial \mathcal{E}(t,z)}{\partial z} - n_0 \Delta E \frac{\partial n(t,z)}{\partial t}. \tag{8.8}$$

In Eq. (8.8) κ is the thermal diffusivity and ΔE is the energy released in the transition of a spin from the metastable state to the ground state,

$$\Delta E = 4hDS^2, \qquad h \equiv \frac{g\mu_B B_z}{2DS}. \tag{8.9}$$

The relation between the energy $\mathcal{E}$ and temperature is given by $\mathcal{E}(T) = \int_0^T C(T')dT'$, where $C(T)$ is the experimentally measured heat capacity per unit cell [137].

To solve the system of Eqs. (8.7) and (8.8) numerically, it is convenient to introduce reduced variables [132]

$$\tilde{\mathcal{E}} \equiv \frac{\mathcal{E}}{n_0 \Delta E}, \qquad \tau \equiv t\Gamma_f, \qquad \tilde{\mathbf{r}} \equiv \frac{\mathbf{r}}{l_d}, \tag{8.10}$$

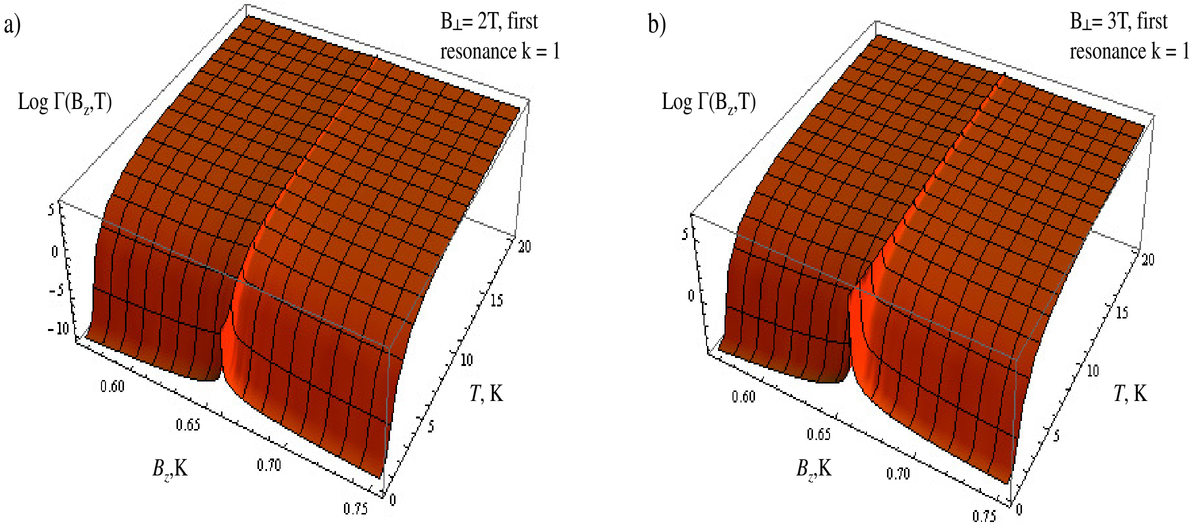

Figure 8.3: Relaxation rate $\Gamma(B_z, T)$ in a generic model of a molecular magnet when a)$B_\perp = 2$ T and b) $B_\perp = 3$ T.

where $n_0 \leq 1$ is the initial population of the metastable state and Γ_f is the relaxation rate at the flame temperature T_f defined by the energy balance $n_0 \Delta E = \mathcal{E}(T_f)$ and some fixed value of $B_{\text{tot},z}$ that we set to the resonance field B_k. The characteristic distance $l_d = \sqrt{\kappa_f / \Gamma_f}$ defines the width of the deflagration front in the case of normal (thermal) deflagration and κ_f is the thermal diffusivity at T_f. In terms of these variables, Eqs. (8.7) and (8.8) become

$$\frac{\partial \tilde{\mathcal{E}}}{\partial \tau} = \frac{\partial}{\partial \tilde{z}} \tilde{\kappa} \frac{\partial \tilde{\mathcal{E}}}{\partial \tilde{z}} - \frac{\partial n}{\partial \tau} \tag{8.11}$$

$$\frac{\partial n}{\partial \tau} = -\tilde{\Gamma} \left(B_{\text{tot},z}, T(\tilde{\mathcal{E}}) \right) n, \tag{8.12}$$

where $\tilde{\Gamma} \equiv \Gamma / \Gamma_f$ is the reduced relaxation rate and $\tilde{\kappa} \equiv \kappa / \kappa_f$. It remains to add the expression for $B_{\text{tot},z}$ in reduced variables, Eq. (8.6) with $D_{zz}(\tilde{z})$ given by Eq. (7.11) with $z \Rightarrow \tilde{z}$ and $R \Rightarrow \tilde{R} \equiv R/l_d$. The important parameter $\tilde{R}$ is the ratio of the width of the front of tunneling that is of order R (see Refs. [131, 136]) and the width of the standard deflagration front [67].

Eqs. (8.11) and (8.12) have been solved numerically by choosing a finite-length sample and discretizing the problem in z. This yields a system of ordinary differential equations in time. We set $\tilde{\kappa} = 1$ for simplicity that means temperature-independent thermal diffusivity. Before solving the equations, $\tilde{\Gamma}$ was calculated from the density matrix equation[133] for the transverse field $B_\perp = 3$ T and tabulated as a function of $B_{\mathrm{tot},z}$ and $\mathcal{E}$. As $\tilde{\Gamma}$ increases by many orders of magnitude near tunneling resonances one has to use many different values of $B_{\mathrm{tot},z}$ for interpolation here. In Fig. 8.3 one can see that for such a strong transverse field the barrier is reduced to zero at resonance where Γ practically does not depend on temperature. Thus near the resonance the cold deflagration should dominate, while off resonance the regular deflagration should take place.

8.3 Quantum Deflagration Fronts

8.3.1 Various Types of Fronts

In Eqs. (8.11) and (8.12), if one switches off the field sweep, while the temperature is rising, a typical thermal fronts develops. This front is shown in figure 8.4 for 2 T and 3 T transverse field at the first resonance.

The effect of the transverse field on the front speed can already be seen. When $B_\perp = 3$ T, one can see shortly after the front starts, the transverse field accelerates the speed of the deflagration front. These fronts were calculated using the numerically calculated relaxation rates from the density matrix formalism. Plots of $\mathrm{Log}(\Gamma(B_z, T))$ are shown in Fig. 8.3 for the cases when $B_\perp = 2$ T and when $B_\perp = 3$ T, with the external swept field expressed in K.

When the field is swept, a small term was added to (8.11) in order to kill self-ignition when computing the solution numerically. The results are shown in fig. 8.5. Hot or cold deflagration take place depending on the various conditions as discussed next.

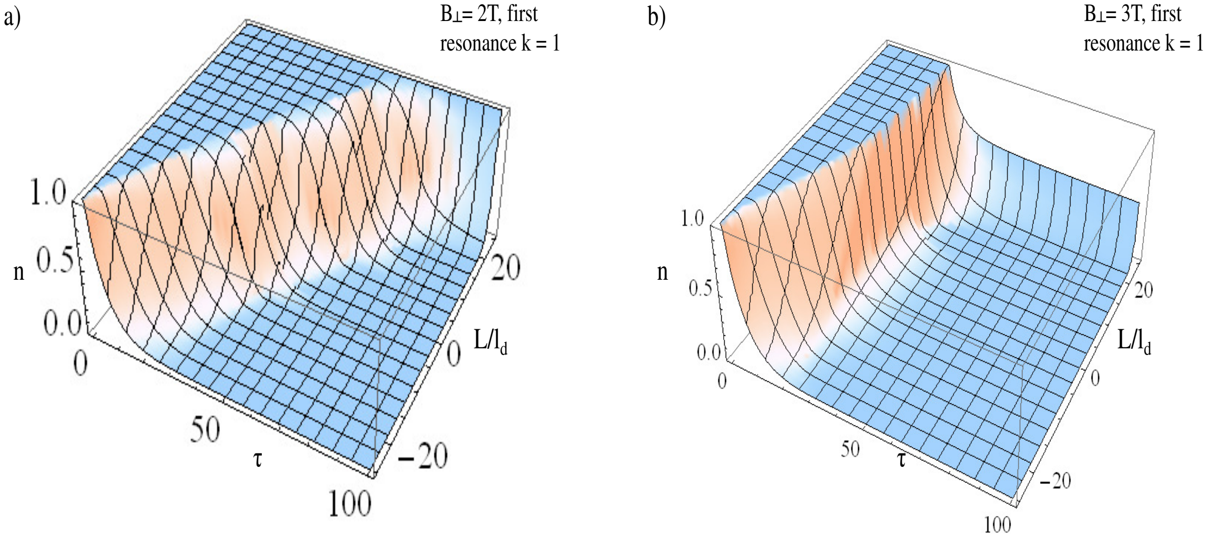

Figure 8.4: Deflagration fronts for $\tilde{R} = 10$ and $\tilde{L} = L/l_d = 50$ as a function of τ and dimensionless spatial variables when a)$B_\perp = 2$ T and b) $B_\perp = 3$ T.

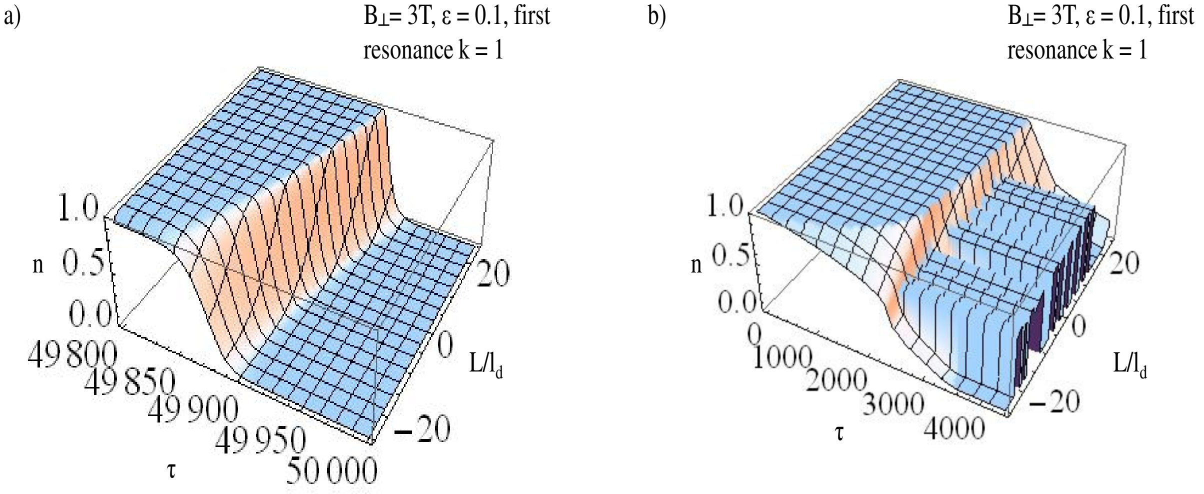

Figure 8.5: Deflagration front when the field is swept for $B_\perp = 2$, $\tilde{R} = 10$ and $\tilde{L} = L/l_d = 50$ and $\epsilon = 0.1$ when the added term to (8.11) is a) 0, b) slightly greater than zero.

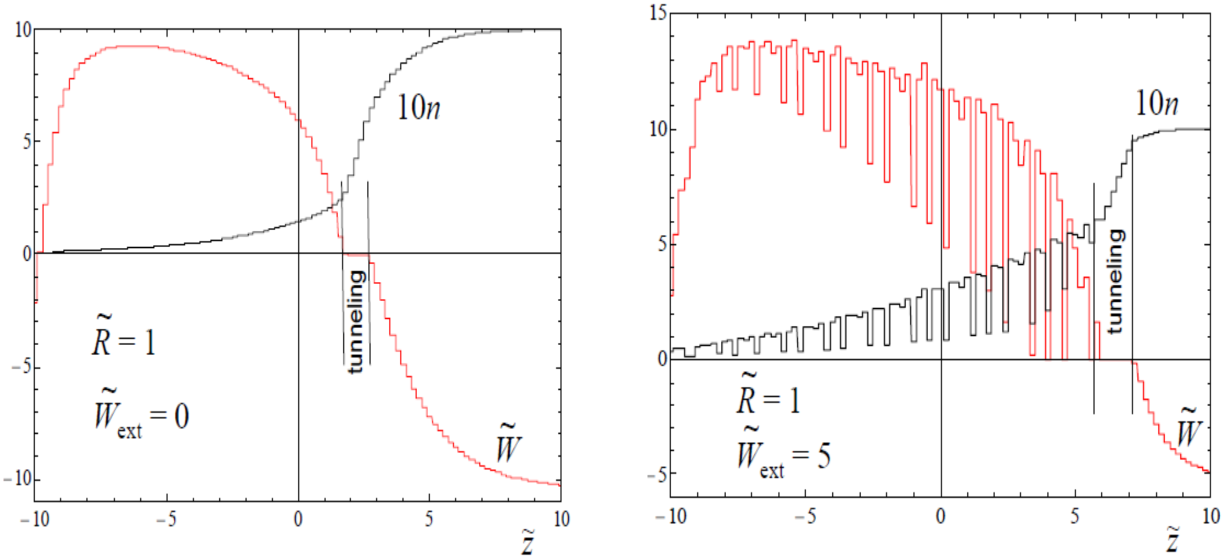

Figure 8.6: Profiles of the metastable population n and the total bias $\widetilde{W}$ across the front for two values of the external bias $\widetilde{W}_{\rm ext}$: (a) $\widetilde{W}_{\rm ext} = 0$, laminar regime; (b) $\widetilde{W}_{\rm ext} = 5$, non-laminar regime.

8.3.2 Front Speed

For the discussion it is convenient to consider the energy bias $W = \varepsilon_{-S} - \varepsilon_{m'}$ between the two resonant levels,

$$W = (S + m')\, g\mu_B \left(B_z + B_z^{(D)} - B_k\right) \equiv W_{\rm ext} + W^{(D)}, \tag{8.13}$$

where $W_{\rm ext}$ does not contain $B_z^{(D)}$. It is convenient to use the reduced external bias

$$\widetilde{W}_{\rm ext} \equiv \frac{W_{\rm ext}}{2E_D} = \left(1 + \frac{m'}{S}\right) \frac{v_0}{2Sg\mu_B} \left(B_z - B_k\right), \tag{8.14}$$

where $E_D \equiv (Sg\mu_B)^2 / v_0$ is the dipolar energy, $E_D/k_B = 0.0671$ K for Mn$_{12}$-ac. At the right end of the dipolar window of Eq. (8.1) one has $B_z = B_k + B^{(D)}$. Thus with the help of Eq. (8.4) one obtains $\widetilde{W}_{\rm ext} = (1/2)(1 + m'/S)\, D_{zz}$, i.e., $\widetilde{W}_{\rm ext} \approx D_{zz}$ for small bias, $m' \approx S$. We will see that in the case of strong tunneling the speed of the quantum deflagration front has a maximum at the right end of the dipolar window, $\widetilde{W}_{\rm ext} \approx \bar{D}_{zz}^{(\rm cyl)} = 10.53$ for Mn$_{12}$-ac.

Cold deflagration can be ignited by the field sweep across the resonance. In this case ignition occurs around the "magical" value $\widetilde{W}_{\rm ext} \cong 5$ that corresponds to $B_z - B_k \cong 22$ mT [131, 136]. Outside the dipolar window fronts of tunneling do not exist that thus cannot be excited. On the other hand, standard deflagration can be initiated, at any bias, by a quick temperature rise on one side of the sample [132]. Applying this method of ignition here, we will see that within the dipolar window the process is modified by spin tunneling and the speed of the burning front can significantly increase for $\tilde{R} \gtrsim 1$, especially at the right end of the window.

There are two regimes of propagation of fronts of tunneling: Laminar and non-laminar. Laminar regime with a smooth front takes place in the left part of the dipolar window, $0 \leq B_z - B_k \leq 10$ mT (or $0 \leq \widetilde{W}_{\text{ext}} \leq 1.3$), while the non-laminar regime with frozen-in quasiperiodic spatial patterns of the magnetization behind the front is realized in the right part of the dipolar window. In both regimes burning is not complete and becomes less complete with increasing the bias. In the laminar regime the residual magnetization and the front speed were calculated analytically [136]. The front speed increases with the bias. In the non-laminar regime, quasi-periodic frozen-in patterns of magnetization deteriorate the resonance condition, and the front speed decreases with the bias after the breakdown of the laminar regime (see Fig. 5 of Ref. [136]). Thermal mechanism of deflagration leads to complete burning of this residual metastable population that smoothens the dipolar field profile in the sample and improves the resonance condition inside the front core. This leads to the increase of the front speed because of spin tunneling in the whole dipolar window.

Results of numerical calculations for the profiles of the metastable population n and the total bias $\widetilde{W}$ in the front for $\tilde{R} = 1$ are shown in Fig. 8.6. Both in laminar and non-laminar regimes, there is a region where $\widetilde{W} \cong 0$ and resonant tunneling takes place, causing a greater slope of $n(z)$. Behind the front (on the left) metastable population n burns to zero via thermal mechanism.

Numerical solutions for the front speed for the generic model with $B_\perp = 3$ T and $\tilde{R} = 1$ and 10 are shown in Fig. 8.7. We plot the reduced front speed $\tilde{v} = v/(l_d \Gamma_f)$ [136]. Within the dipolar window the front speed can largely exceed the speed of regular deflagration and depends on the transverse crystal size R parametrized by $\tilde{R}$.

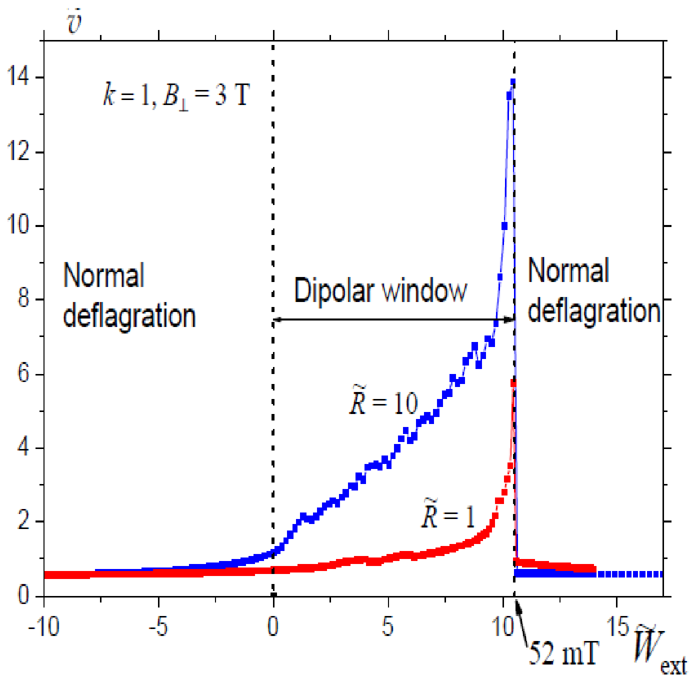

Figure 8.7: Reduced front speed $\tilde{v}$ vs bias field for different values of the reduced transverse size $\widetilde{R} \equiv R/l_d$, l_d being the width of the thermal deflagration front. For such a strong applied transverse field, the effect of tunneling is dramatic.

At $B_\perp = 3$ T the maximal values of $\tilde{v}$ are attained at the right end of the dipolar window, followed by a steep drop towards the standard-deflagration result outside the dipolar window. For smaller transverse fields such as 2 T, the effect of spin tunneling is weaker and $\tilde{v}$ reaches a maximum somewhere in the middle of the dipolar window, depending on $\tilde{R}$.

8.4 Conclusion

Measurements of the speed of deflagration fronts [67, 71] were done in zero or small transverse field, so that the influence of resonance spin tunneling on the front speed is not so dramatic as in Fig. 8.7. It would be highly interesting to perform deflagration experiments in strong enough transverse field to see the big effect of tunneling on the front propagation. Changing thermal contact of the crystal with the environment, one can boost or suppress the thermal mechanism of magnetic burning thus isolating thermal and quantum effects from each other.

Bibliography

[1] E. M. Chudnovsky and L. Gunther, Phys. Rev. Lett **60**, 661 (1988).

[2] E. M. Chudnovsky and J. Tejada,*Macropscopic Quantum Tunneling of the Magnetic Moment*, Cambridge University Press (1998).

[3] E. M. Chudnovsky, Phys. Rev. Lett. **72**, 3433 (1994).

[4] L. D. Landau and E. M. Lifshitz, Sov. Phys. JETP **8**, 153 (1935).

[5] R. P. Feynman and A. R. Hibbs,*Quantum Mechanics and Path Integrals*, McGraw-Hill, New York (1965).

[6] E. Freidkin, *Field Theories of Condensed Matter*, Addison-Wesley, New York (1991).

[7] D. Loss, D. P. DiVincenzo, and G. Grinstein, Phys. Rev. Lett. **69**, 3232 (1992).

[8] J. von Delft and C. L. Henley, Phys. Rev. Lett. **69**, 3236 (1992).

[9] E. Vincent, J. Hamman, P. prene, and E. Tronc, J. Physique **4**, 273 (1994).

[10] E. M. Chudnovsky and J. Tejada,*Lectures on Magnetism*, (Rinton Press, Princeton, New Jersey, 2006).

[11] J. Tejada, R. F. Ziolo, and X. X. Zhang. Chem. Mater. **8**, 1784 (1996) (review).

[12] B. Barbara, and E. M. Chudnovsky, Phys. Rev. Lett. *A* **145**, 205(1990).

[13] D. D. Awschalom, J. F. Smyth, G. Grinstein, D. T. DiVincenzo, and D. Loss, Phys. Rev. Lett. **68**, 3092 (1992).

[14] T. G. St. Pierre, D. H. Jones, and D. P. E. Dickson, J. magn. Magn. mater., **69**, 276 (1987).

[15] R. Bauminger and I. Nowik, Hyperfine Interactions, **50**, 484 (1989).

[16] J. Tejada and X. X. Zhang, J. Phys.: Condens. matter **6**, 236 (1994).

[17] S. Gider, D. D. Awschalom, T. Douglas, S. Mann, and M. Chaparala, Science **268**, 77 (1995).

[18] S. H. Kilcoyne and R. Cywinski, J. Magn. Magn. Mater: **140-144**, 1466 (1995).

[19] F. Luis, E. del Barco, X. X. Zhang, J. M. hernandez, J. Bartolome, and J. Tejada (unpublished).

[20] S. H. Bell, M. P. Weir, D. P. E. Dickson, J. F. Gibson, G. A. Sharp, and T. J. Peters, Biochim. Biophys. Acta **787**, 227 (1994).

[21] T. Lis, Acta Crystallogr. B **36**, 2042 (1980).

[22] R. Sessoli, D. Gatteschi, A. Ganeschi, and M. A. Novak, Nature (London) **365**, 141 (1993).

[23] A. Caneshi, D. Gatteschi, R. Sessoli, A. L. Barra, L. C. Brunel, and M. Guillot, J. Am. Chem. Soc. **113** 5873 (1991).

[24] J. R. Friedman, M. P. Sarachik, J. Tejada, and R. Ziolo, Phys. Rev. Lett. **76**, 3830 (1996).

[25] B. Barbara, W. Wernsdorfer, L. C. Sampaio, J.-G. Park, C. Paulsen, M. A. Novak, R. Ferre, D. Mailly, R. Sessoli, A. Caneshi, K. Hasselbach, A. Benoit, and L. Thomas J. Magn. Magn. Mater.,**140**, 1825 (1995).

[26] M. A. Novak, R. Sessoli in *Quantum Tunneling of magnetization QTM'94*, ed. L. Gunther and B. Barbara, John Wiley & Sons, New York, p171-188 (1995).

[27] C. Paulsen, J.-G. Park, B. Barbara, R. Sessoli, A. Caneshi J. Magn. Magn. Mater., **140**, 379 (1995).

[28] R. Sessoli, H. L. Tsai, A. R. Schake, S. Wang, J. B. Vincent, K. Folting, D. Gatteschi, G. Christou, and D. N. Hendrikson, J. Am. Chem. Soc. **115**, 1804 (1993).

[29] C. Paulsen and J. G. Park in *Quantum Tunneling of Magnetization QTM'94*, ed. by L. Gunther and B. Barbara, John Wiley & Sons, New York, p189-207 (1995).

[30] J. M. Hernández, X. X. Zhang, F. Luis, J. Tejada, J. R. Friedman, M. P. Sarachik, and R. Ziolo, Phys. Rev. B **55**, 5858 (1997).

[31] J. R. Friedman and M. P. Sarachik arXiv:1001.4194v1

[32] E. M. Chudnovsky, and D. A. Garanin, Phys. Rev. Lett. **87**, 187203 (2001).

[33] E. M. Chudnovsky, and D. A. Garanin, Phys. Rev. B **65**, 094423 (2002).

[34] K. Park, T. Baruah, N. Bernstein, and M. R. Pederson, Phys. Rev. B **69**, 144426 (2004).

[35] K. M. Mertes, Y. Suzuki, M. P. Sarachik, Y. Paltiel, H. Shtrikman, E. Zeldov, E. M. Rumberger, D. N. Hendrickson, and G. Christou, Phys. Rev. Lett. **87**, 227205 (2001).

[36] E. del Barco, A. D. Kent, E. M. Rumberger, D. N. Hendrickson, and G. Christou, Phys. Rev. Lett. **91**, 047203 (2003).

[37] E. del Barco, A. D. Kent, S. Hill, J. M. North, N. S. Dalal, E. M. Rumberger, D. N. Hendrickson, and G. Christou, J. Low Temp. Phys. 119 (2005).

[38] S. Hill, R. S. Edwards, S. I. Jones, N. S. Dalal,and J. M. North, Phys. Rev. Lett. **90**, 217204 (2003).

[39] S. Takahashi, R. S. Edwards, J. M. North, S. Hill, and N. S. Dalal, Phys. Rev. B **70**, 094429 (2004).

[40] A. Cornia, R. Sessoli, L. Sorace, D. Gatteschi, A. L. Barra, and C. Daiguebonne, Phys. Rev. Lett. **89**, 257201 (2002).

[41] Kevin Mertes, PH.D. Thesis, The City University of New York (2002).

[42] D. A. Garanin, Journal of Physics A, **24**, L61 1991.

[43] L. D. Landau, and E. M. Lifshitz, *Quantum Mechanics*, 1997, Pergamon, London

[44] L. D. Landau, Phys. Z. Sowjetunion, **2**, 46, (1932).

[45] C. Zener, Proc. R. Soc. Lodon A, **137**, 696 (1932).

[46] E. C. G. Stueckelberg, Helv. Phys. Acta, textbf5 370 (1932).

[47] A. L. Barra, P. Debrunner, D. Gatteschi, C. E. Schulz, and R. Sessoli Europhys. Lett. **78**, 133 (1996).

[48] C. Sangregorio, T. Ohm, C. Paulsen,R. Sessoli, and D. Gatteschi, Phys. Rev. Lett. **78**, 4645 (1997).

[49] A. Garg, Europhys. Lett. **22**, 205 (1993).

[50] A. Garg, Phys. Rev. B **51**, 15161 (1995).

[51] W. Wernsdorfer, and R. Sessoli, Science **284**, 133 (1999).

[52] M. V. Berry, Proc. R. Soc. London Ser. A **392**, 45 (1984).

[53] W. Wernsdorfer, R. Sessoli, A. Caneshi, D. Gatteschi, A. Cornia, and D. Mailly, J. Appl. Phys. **87**, 5481 (2000).

[54] C. M. Ramsey, E. del Barco, S. Hill, S. J. Shah, C. C. Beedle, and D. N. Hendrickson Nat. Phys. **4**, 277 (2008).

[55] W. Wernsdorfer, T. C. Stamatatos, and G. Christou Phys. Rev. Lett. **101**, 237204 (2008).

[56] O. Waldmann, T. C. Stamatatos, G. Christou, H. U. Gudel, I. Sheikin, and H. Mutka Phys. Rev. Lett. **102**, 157202 (2009).

[57] A. Chiolero, and D. Loss, Phys. Rev. Lett. **80**, 169 (1998).

[58] V. I. Goldanskii, Dokl. Acad. Nauk SSSR **124**, 1261 (1959) [Sov. Phys. Dokl. **4**, 74 (1959)].

[59] I. Affleck, Phys. Rev. Lett. **46**, 388 (1981).

[60] A. I. Larkin, and Yu. N. Ovchinnikov, Pis'ma Zh. É ksp. Teor. Fiz. textbf37, 322 (1983) [JETP Lett. **37**, 382 (1983)].

[61] E. M. Chudnovsky, Phys. Rev. A**46**, 8011 (1992).

[62] D. A. Garanin, X. Mart í nes Hidalgo, and E. M. Chudnovsky, Phys. Rev. B **57**, 13639 (1998).

[63] E. M. Chudnovsky, and D. A. Garanin, Phys. Rev. Lett. **79**, 4469 (1997).

[64] A. D. Kent, Y. Zhong, L. Bokacheva, D. Ruiz, D. N. Hendrickson, and M. P. sarachik, Europhys. Lett. **49**, 521 (2000).

[65] L. Bokacheva, A. D. kent, and M. A. Walter, Phys. Rev. Lett. **85**, 4803 (2000).

[66] W. Wernsdorfer, M. Murugesu, and G. Christou, Phys. Rev. Lett. **96**, 057208 (2006).

[67] Y. Suzuki, M. P. Sarachik, E. M. Chudnovsky, S. McHugh, R. Gonzalez-Rubio, N. Avraham, Y. Myasoedov, E. Zeldov, H. Shtrikman, N. E. Chakov, and G. Christou, Phys. Rev. Lett. **95**, 147201 (2005).

[68] R. Jaafar, S. McHugh, Yoko Suzuki, M. P. Sarachik, Y. Myasoedov, E. Zeldov, H. Shtrikman, R. Bagai, and G. Christou J. Magn. Magn. Mater. **320** 695, (2008).

[69] L. D. Landau, and E. M. Lifshitz, *Fluid Dynamics* (Pergamon, 1987).

[70] D. A. Garanin and E. M. Chudnovsky, Phys. Rev. B. **76**, 054410 (2007).

[71] A. Hernández-Mínguez, J. M. Hernández, F. Macià, A. García-Santiago, J. Tejada, and P. V. Santos, Phys. Rev. Lett. **95**, 217205 (2005).

[72] J. Tejada, E. M. Chudnovsky, J. M. Hernández, and R. Amigo, Appl. Phys. Lett. **84**, 2373 (2004).

[73] A. Hernández-Mínguez, M. Jordi, R. Amigo, A. García-Santiago, J. M. Hernández, and J. Tejada, Europhys. Lett. **69**, 270 (2005).

[74] O. Shafir and A. Keren, Phys. Rev. B **79**, 180404 (2009).

[75] S. McHugh, R. Jaafar, M. P. Sarachik, Y. Myasoedov, A. Finkler, H. Shtrikman, E. Zeldov,R. Bagai, and G. Christou, Phys. Rev. B **76**, 172410 (2007).

[76] C. Kittel, *Quantum Theory of Solids*, Wiley and Sons, New York-London (1963)

[77] A. Einstein and W. J. de Haas, Verhandl. Deut. Physik Ges. **17**, 152 (1915);**18**, 173 (1916);**18**, 423 (1916).

[78] S. J. Barnett, Phys. Rev. **6**, 239 (1915).

[79] See, e.g., V. Ya. Frenkel, Sov. Phys. Usp. **22**, 580 (1979) about the history of Einstein - de Haas and Barnett experiments.

[80] S. J. Barnett and G. S. Kenny, Phys. Rev. **87**, 723 (1952); G. G. Scott and H. W. Sturner, Phys. Rev. **184**, 490 (1969), and references therein.

[81] R. Jaafar, E. M. Chudnovsky, and D. A. Garanin, Phys. Rev. B **79**, 104410 (2009).

[82] T. M. Wallis, J. Moreland, and P. Kabos. Appl. Phys. Lett. **89**, 122502 (2006).

[83] A. Messiah, *Quantum Mechanics*, Lecture Notes in Physics Vol. 2 (Wiley, New York, 1976).

[84] V. Dohm and P. Fulde, Z. Phys. B **21**, 369 (1975).

[85] E. M. Chudnovsky, D. A. Garanin, and R. Schilling, Phys. Rev. B **72**, 094426 (2005).

[86] E. M. Chudnovsky and D. A. Garanin, Phys. Rev. Lett. **93**, 257205 (2004).

[87] C. Calero, E. M. Chudnovsky, and D. A. Garanin, Phys. Rev. Lett. **95**, 166603 (2005).

[88] C. Calero and E. M. Chudnovsky, Phys. Rev. Lett. **99**, 047201 (2007).

[89] L. D. Landau and E. M. Lifshitz, *Theory of Elasticity* (Pergamon, New York, 1959).

[90] E. Finot, A. Passian, and T. Thundat, Sensors **8**, 3497 (2008).

[91] J. R. Friedman, V. Patel, W. Chen, S. K. Tolpygo, and J. E. Lukens, Nature **406**, 43 (2000); C. H. van der Wal, A. C. J. ter Haar, F. K. Wilhelm, R. N. Schouten, C. J. P. M. Harmans, T. P. Orlando, S. Lloyd, and J. E. Mooij, Science **290**, 773 (2000).

[92] A. Ardavan, O. Rival, J. J. L. Morton, S. J. Blundell, A. M. Tyryshkin, G. A. Timco, and R. E. P. Winpenny, Phys. Rev. Lett. **98**, 057201 (2007); S. Bertaina, S. Gambarelli, T. Mitra, B. Tsukerblat, A. Müller, and B. Barbara, Nature **453**, 203 (2008); C. Schlegel, J. van Slageren, M. Manoli, E. K. Brechin, and M. Dressel, Phys. Rev. Lett. **101**, 147203 (2008).

[93] W. Wernsdorfer, Nature Materials **6**, 174 (2007).

[94] E. M. Chudnovsky, D. A. Garanin, and R. Schilling, Phys. Rev. B **72**, 094426 (2005).

[95] L. D. Landau and E. M. Lifshitz, *Theory of Elasticity* (Pergamon, New York, 1959).

[96] H. B. Heersche, Z. de Groot, J. A. Folk, H. S. J. van der Zant, C. Romeike, M. R. Wegewijs, L. Zobbi, D. Barreca, E. Tondello, and A. Cornia, Phys. Rev. Lett. **96**, 206801 (2006); M.-H. Jo, J. E. Grose, K. Baheti, M. M. Deshmukh, J. J. Sokol, E. M. Rumberger, D. N. Hendrickson, J. R. Long, H. Park, and D. C. Ralph, Nano Lett. **6**, 2014 (2006); J.J. Henderson, C.M. Ramsey, E. del Barco, A. Mishra, and G. Christou, J. Appl. Phys. **101**, 09E102 (2007); S. Voss, M. Fonin, U. Rudiger, M. Burgert, and U. Groth, Appl. Phys. Lett. **90**, 133104 (2007).

[97] R. Jaafar, and E. M. Chudnovsky, Phys. Rev. Lett. **102**, 227202 (2009).

[98] E. K. Irish and K. Schwab, Phys. Rev. B **68**, 155311 (2003).

[99] D. Goldhaber-Gordon, J. Gres, H. Shtrikman, D. Mahalu, U. Meirav and M. A. Kastner, Nature **391**, 156 (1998).

[100] S. M. Cronenwett, T. H. Oosterkamp and L. P. Kouwenhoven, Science **281**, 540 (1998).

[101] W. G. van der Wiel, S. De Franceschi, T. Fujisawa, J. M. Elzerman, S. Tarucha and L. P. Kouwenhoven, Science**289**, 2105 (2000).

[102] J. Nygard, D. H. Cobden and P. E. Lindelof, nature **408**, 342 (2000).

[103] H. B. Heersche, Z. de Groot, J. A. Folk, H.S. van der Zant, C. Romeike, M. R. Wegewijs, L. Zobbi, D. Barreca, E. Tondello, and A. Cornia, Phys. Rev. Lett. **96**, 206801 (2006).

[104] M.-H. Jo, J. E. Grose, K. baheti, M. M. Deshmukh, J. J. Sokol, E. M. Rumberger, D. N. Hendrickson, J. R. Long, H. Park, and D. C. Ralph, Nano Lett. **6**, 2014 (2006).

[105] J. J. Henderson, C. M. Ramsey, E. del Barco, A. Mishra, and G. Christou, J. Appl. Phys. **101**, 09E102 (2007).

[106] Voss S., Fonin M., Rudiger U., Burgert M. and Groth U., *Phys. Rev. B*, **78** (2008) 155403.

[107] J. Park, A. N. Pasupathy, J. I. Goldsmith, C. Chang, Y. Yaish, J. R. Petta, M. Rinkoski, J. P. Sethna, H. D. Abruña, P. L. McEuen, and D. C. Ralph, Nature **417**, 722 (2002).

[108] G.-H. Kim and T.-S. Kim, Phys. Rev. Lett. **92**, 137203 (2004).

[109] F. Elste, and C. Timm, Phys. Rev. B **71**, 155403 (2005).

[110] C. Timm, and F. Elste, Phys. Rev. B **73** 235304 (2006).

[111] C. Romeike, M. R. Wegewijs, W. Hofstetter, and H. Schoeller, Phys. Rev. Lett. **96**, 196601 (2006).

[112] G. González, and M. N. Leuenberge Phys. Rev. Lett. **98**, 256804 (2007).

[113] M. Misiorny, and J. Barnaś Phys. Rev. B **76** 054448 (2007).

[114] M. Misiorny, I. Weymann and J. Barnaś, Phys. Rev. B **79**, 22420 (2009).

[115] P. S. Cornaglia, Gonzalo Usaj, and C. A. Balseiro, Phys. Rev. B **76**, 241403 (2007).

[116] S. Barraza-Lopez, K. Park, V. García-Suárez, and J.Ferrer J. Appl. Phys. **105**, 07E309 (2009); Phys. Rev. Lett. **102**, 246801 (2009).

[117] C. Benjamin, T. Jonckheere, A. Zazunov, and T. Martin, Europhys. J. B, **57** 279 (2007) ; M. Lee, T. Jonckheere, and T. Martin Phys. Rev. Lett. **101** 146804 (2008).

[118] E. M. Chudnovsky, and D. A. Garanin arXiv:cond-mat/0911.2810.

[119] R. Jaafar, E. M. Chudnovsky and D. A. Garanin, Europhys. Lett. **89** 27001 (2010).

[120] E. M. Chudnovsky, and D. A. Garanin, Phys. Rev. Lett., **89**, 157201 (2002); C. L. Joseph, C. Calero,and E. M. Chudnovsky, Phys. Rev. B, **70**, 174416 (2004).

[121] S. Mchugh, R. Jaafar, M. P. Sarachik, Y. Myasoedov, A. Finkler, H. Shtrikman, E. Zeldov, R. Bagai, and G. Christou, Phys. Rev. B. **76**, 172410 (2007).

[122] W. Wernsdorfer, R. Sessoli, D. Gatteschi, Europhys. Lett. **47**, 254 (1999).

[123] W. Wernsdorfer, N.E. Chakov, G. Christou, http://arxiv.org/abs/cond-mat/0405014.

[124] A. Morello, F. L. Mettes, F. Luis, J. F. Fernandez, J. Krzystek, G. Arom, G. Christou, and L. J. de Jongh, Phys. Rev. Lett. **90**, 017206 (2003).

[125] M. Evangelisti, A. Candini, A. Ghirri, M. Affronte, G. W. Powell, I. A. Gass, P. A. Wood, S. Parsons, E. K. Brechin, D. Collison, and S. L. Heath, Phys. Rev. Lett. **97**, 167202 (2006).

[126] F. Luis, J. Campo, J. Gmez, G. J. McIntyre, J. Luzn, and D. Ruiz-Molina, Phys. Rev. Lett. **95**, 227202 (2005).

[127] D. A. Garanin and E. M. Chudnovsky, Phys. Rev. B. **78**, 174425 (2008).

[128] A. Caneschi, T. Ohm, C. Paulsen, D. Rovai, C. Sangregorio and R. Sessoli, J. Magn. and Magn. Matt. 177-181, 1330 (1998); Z. Sun, D. Ruiz, N. R. Dilley, M. Soler, J. Ribas, K. Folting, M. B. Maple, G. Christou and D. N. Hendrickson,

Chem. Commun., 1973 (1999); Wernsdorfer, R. Sessoli, D. Gatteschi, Europhys. Lett. **47**, 254 (1999).

[129] M. Soler, W. Wernsdorfer, Z. Sun, J. C. Huffman, D. N. Hendrickson and G. Christou, Chem. Commun. (Cambridge) 2003, 2672 (2003).

[130] W. Wernsdorfer, N.E. Chakov, and G. Christou, http://arxiv.org/abs/cond-mat/0405014.

[131] D. A. Garanin and E. M. Chudnovsky, Phys. Rev. Lett. **102**, 097206 (2009).

[132] D. A. Garanin and E. M. Chudnovsky, Phys. Rev. B **56**, 11102 (1997).

[133] D. A. Garanin, arXiv:0805.0391v1 (2008).

[134] E. M. Chudnovsky, Phys. Rev. Lett. **92**, 120405 (2004).

[135] E. M. Chudnovsky, D. A. Garanin, and R. Schilling, Phys. Rev. B **72**, 094426 (2005).

[136] D. A. Garanin, Phys. Rev. B **80**, 014406 (2009).

[137] A. M. Gomes, M. A. Novak, R. Sessoli, A. Caneschi, and D. Gatteschi, Phys. Rev. B **57**, 5021 (1998).

Papers by Reem Jaafar

Published Works

Articles

1. Deflagration with quantum and dipolar effects in a model of a molecular magnet. D. A. Garanin and R. Jaafar, Phys. Rev. B **81**, 180401 (2010).
2. Single magnetic molecule between conducting leads: Effect of mechanical rotations. R. Jaafar, E. M. Chudnovsky and D. A. Garanin, Europhys. Lett. **89** 27001 (2010).
3. Magnetic Molecule on a Microcantilever: Quantum Magnetomechanical Oscillations. R. Jaafar, and E. M. Chudnovsky, Phys. Rev. Lett. **102**, 227202 (2009).
4. Dynamics of Einstein - de Haas Effect: Application to Magnetic Cantilever. R. Jaafar, E. M. Chudnovsky, and D. A. Garanin, Phys. Rev. B **79**, 104410 (2009).
5. Experimental Determination of the Dipolar Field in Mn_{12}-acetate. S. McHugh, R. Jaafar, M. P. Sarachik, Y. Myasoedov, H. Shtrikman, E. Zeldov, R. Bagai, and G. Christou, Phys. Rev. B **79**, 052404 (2009).
6. Magnetic Avalanches of Minor fast-Relaxing Species in Mn_{12}-acetate. S. McHugh, R. Jaafar, M. P. Sarachik, Y. Myasoedov, A. Finkler, E. Zeldov, R. Bagai, and G. Christou, Phys. Rev. B **80**, 024403 (2009).

7. Spatial Determination of Magnetic Avalanche Ignition Points. R. Jaafar, S. McHugh, Yoko Suzuki, M. P. Sarachik, Y. Myasoedov, E. Zeldov, H. Shtrikman, R. Bagai, and G. Christou, J. Magn. Magn. Mater. **320** 695, (2008).
8. Effect of Quantum Tunneling on the Ignition and Propagation of magnetic avalanches in Mn_{12}-acetate. S. Mchugh, R. Jaafar, M. P. Sarachik, Y. Myasoedov, A. Finkler, H. Shtrikman, E. Zeldov, R. Bagai, and G. Christou, Phys. Rev. B. **76**, 172410 (2007).